DISSERTATION

PART 1: SYNTHESIS AND CHARACTERIZATION OF MAGNETIC Cr_5Te_8 NANOPARTICLES

PART 2: LOCAL ATOMIC STRUCTURE STUDIES USING THEORY TO SIMULATE POLARONS IN SUPERCONDUCTING CUPRATES AND EXPERIMENT TO ANALYZE ALTERNATIVE ENERGY NANOMATERIALS

Submitted by

Mary B. Martucci

Department of Chemistry

In partial fulfillment of the requirements

For the Degree of Doctor of Philosophy

Colorado State University

Fort Collins, Colorado

Spring 2012

Doctoral Committee:

Advisor: Amy L. Prieto

C. Michael Elliott
Ellen R. Fisher
Dawn Rickey
Carl E. Patton

ABSTRACT

PART 1: SYNTHESIS AND CHARACTERIZATION OF MAGNETIC Cr_5Te_8 NANOPARTICLES

PART 2: LOCAL ATOMIC STRUCTURE STUDIES USING THEORY TO SIMULATE POLARONS IN SUPERCONDUCTING CUPRATES AND EXPERIMENT TO ANALYZE ALTERNATIVE ENERGY NANOMATERIALS

The field of spintronics, the development of spin-based devices that utilize the spin degree of freedom to increase memory capacity, has emerged as a solution to faster more efficient memory storage for electronic devices. One class of materials that has been extensively studied is the half-metallic ferromagnets, compounds that are 100% spin-polarized at the Fermi level. One material in this group that has been investigated is chromium telluride ($Cr_{1-x}Te$), whose family of compounds is known to exhibit a wide range of interesting magnetic and electronic properties. We have developed a hot injection solution synthesis of Cr_5Te_8 nanoplatlets which show similar magnetic behavior to the bulk material. It has also been shown that selenium and sulfur analogues can be obtained without changing the reaction conditions, making progress toward a better understanding of the reaction as well as an interesting family of compounds.

Using real-space simulations, the effect of polarons in the high-Tc superconducting cuprates has been studied. The simulations demonstrate energetically favorable sites for the defects and show evidence of longer-range pairing interactions. Variations of the stripe show similar energetic results. X-ray absorption fine structure

spectroscopy and neutron scattering have been utilized to examine the local structure of Ni-doped Mg nanoparticles, a hydrogen storage material as well as Cu_2ZnSnS_4 (CZTS) nanoparticles, a photovoltaic material. The Mg-Ni material shows much local disorder upon hydrogen cycling. The CZTS data demonstrate a loss of sulfur from around the copper sites upon annealing, helping to explain the changes observed in the optical absorption properties resulting from the annealing process.

ACKNOWLEDGEMENTS

I would like to thank my advisors, Amy Prieto (CSU) and Steve Conradson (LANL), for their guidance and knowledge. It is truly a privilege to have had the opportunity to learn so much from you both.

Thanks to my committee members for their thoughtful and constructive evaluations of my work over the years.

Thanks to all my colleagues, both at the department of chemistry at CSU and the materials science division at LANL, for their enthusiasm for the work that we do and the collaborative spirit that is so evident among both groups. It helps to make the tough days a little easier.

To Mike McKay for all of the kindness and support during the final stages of my dissertation. The endless supply of encouraging words and coffee are appreciated more than you could ever imagine.

To my family: Daddy, Mommy, Mike, Anne, and Joe. Your unwavering love and support make all goals in life possible, and any obstacle surmountable. Thank you for giving me roots to hold on to no matter where life will take me and wings so that I have the independence and determination to accomplish all that I set out to do.

TABLE OF CONTENTS

PART 1: SYNTHESIS AND CHARACTERIZATION OF MAGNETIC Cr_5Te_8 NANOPARTICLES

Chapter 1: Synthesis and Characterization of Magnetic Cr_5Te_8 Nanoparticles[i]

1.1 Introduction

As electronic devices continue to become smaller and more efficient, the need has arisen to combat the approaching size limitations of Moore's Law, which predicts that the number of transistors used on an integrated circuit will double approximately every two years.[1,2] The field of spintronics, the development of spin-based devices that utilize the spin degree of freedom to increase memory capacity, has emerged as a solution to faster more efficient memory storage for electronic devices.[3-6] The development of this field has resulted from several key discoveries: the first was a discovery made by Johnson and Silsbee in 1985 in which they observed that a significant imbalance between spin-up and spin-down sub-bands in a ferromagnet will result in coupling between the charge and spin transport across the interface from the ferromagnetic material to a paramagnetic metal.[7] The second discovery, made independently by two different scientists in 1988, was the observation of the phenomenon known as giant magnetoresistance. This effect occurs in thin film structures that consist of alternating ferromagnetic and non-magnetic layers, which exhibit significant changes in electrical resistance depending on how the separated ferromagnetic layers are aligned with each other (parallel or anti-parallel).[8,9] Following these discoveries, Datta and Das proposed the idea of spin-based field-effect-

[i] All experimental work in this chapter was done by Mary B. Martucci. High-resolution TEM images were obtained with the assistance of Dr. Gary Zito at the Colorado School of Mines.

transistor (SPIN-FET) as a device that could harness the utility of these phenomena create a spin-based device.[10]

One class of materials that has been extensively studied for this application is the half-metallic ferromagnets, consisting of compounds that are 100% spin-polarized at the Fermi level. The term "half-metal", coined by de Groot and coworkers in 1983, arises from the fact that one spin channel is metallic, while the other is insulating, giving the ideal spin polarization (all the spins in the conducting band aligned) for fabricating a device based on spin.[11,12] Following this discovery, much research focused on the search for optimal half-metallic ferromagnetic materials, leading to the advent of many new avenues of research on this topic. Among the materials that have been studied for their 100% spin-polarization half-metallic properties are the Heusler alloys, semi-Heusler alloys, magnetic oxides (including CrO_2 and Fe_3O_4), and colossal magnetoresistance materials.[13-25]

In addition to these types of materials, another important subset of half-metallic ferromagnets that exhibit these key features is the zinc-blend transition metal chalcogenides and pnictides.[26-33] One material in particular from this group that has been investigated is chromium telluride ($Cr_{1-x}Te$), which has received increasing attention in research because it is a half-metallic ferromagnetic solid that has been shown to exhibit giant magnetovolume and large magnetoresistance.[34,35] These properties make it a promising candidate for application in magneto-optic materials and spin-dependent devices.[26,32] Chromium telluride has previously been synthesized by sequential electron beam evaporation, diffusion of superlattice reactants, classic solid-state reactions, molecular beam epitaxy, and there are also limited reports on solution-phase

syntheses.[32,36-39] Recently, Liu, Bose and Kudrnovsky presented first-principle calculations comparing the magnetic properties of the different CrTe phases: zinc blende, rocksalt, and the NiAs-type structure in terms of growing them as thin films on a substrate. These calculations show that the NiAs-type lattice is not predicted to be half-metallic at its equilibrium volume but that the zinc blende and rocksalt structures will exhibit the half-metallic behavior.[40] Theoretical studies such as this one help to focus synthetic efforts on more promising candidates for spintronic applications.

Table 1.1: The nine predicted compounds in the Cr/Te family and their crystal structures.

Compound	Crystal Structure
$Cr_{1-x}Te$	hexagonal, cubic
$CrTe_2$	hexagonal
$CrTe_3$	monoclinic
Cr_2Te_3	trigonal
Cr_5Te_6	monoclinic
Cr_7Te_8	monoclinic hexagonal
Cr_3Te_4	monoclinic
Cr_5Te_8	monoclinic trigonal

The chromium/tellurium system is a large family of compounds with a wide range of crystal structures and varying magnetic properties. Different studies of the Cr-Te phase diagram have shown the existence of at lease nine different phases, which are presented in Table 1.1.[41,42] In spite of the potential of some of these magnetically interesting compounds, the focus of most of the research on these compounds has been on $Cr_{1-x}Te$, the predicted half-metallic ferromagnet.[35,38,43-45]

Nanoscience is a rapidly developing field that has generated much interest, in part, because of the drive for smaller devices and because it has been shown that nanoparticles often exhibit different properties than the bulk material and with the

constant drive for smaller electronic devices, the ability to synthesize materials as thin films and at the nanoscale in this field is essential.[46-48] The most common solution phase synthesis of nanoparticles is the hot-injection method, involving dissolution of precursors followed by rapid injection into a hot solution of surfactant which initiates nucleation and growth of the nanoparticles.[49-51] This is advantageous when developing synthetic routes to nanoparticles because of the control over the various reaction parameters, which often leads to uniform size distribution and control over morphology.[52-55] This particular method has also had much success in the synthesis of transition metal chalcogenides.[56,57] Solution synthesis of nanomaterials also has the advantage of being far more cost-effective than the aforementioned synthetic methods for chromium telluride, and also has the possibility of offering ease of processing in device development through techniques such as dip-casting.[58,59] We have developed a solution-phase synthesis of Cr_5Te_8 nanoplatlets. To our knowledge, there have been no previous reports in the literature of a synthesis for nanoparticles of any compounds in the Cr/Te family. The synthesis and characterization of this material will be discussed herein.

1.2 Experimental

Chemicals. Chromium (II) chloride ($CrCl_2$, Aldrich, 99.999%), Tellurium powder (Te, Alfa Aesar, 99.999%), trioctylphosphine (TOP, Aldrich, 90%), dodecylamine (DDA, Aldrich, 99%) and oleylamine (OLA, Aldrich, 70%) were purchased and used without further purification. All reactions were kept under an inert atmosphere using standard air-free techniques to prevent oxidation of the chromium (II) precursor and resulting products.

Synthesis of Cr_5Te_8 Nanoplatelets. Tellurium powder (0.06 mmol), TOP (0.50 mL), and OLA (1.5 mL) were measured out into a three-necked roundbottom flask. $CrCl_2$ (0.06 mmol) and OLA (2 mL) were loaded into a second roundbottom flask. Both flasks were heated under nitrogen flow on a Schlenk line to 125 ºC to dissolve the precursors. The chromium precursor solution was then injected into the Te/TOP/OLA mixture and heated to 350 ºC at a rate of 650 ºC per hour. The reaction solution was held at the target temperature for 45 minutes before being cooled to room temperature. The solid black product was washed with hexanes followed by precipitation using acetone and subsequent centrifugation and decantation. This process was repeated three times to ensure the removal of excess organics. Following this washing process, the particles were re-suspended in hexanes and washed with a warm 1:5 degassed water/isopropanol mix in attempt to eliminate any possible amorphous chromium chloride impurity. The reaction yielded ~15nm thick nanoplatelets of Cr_5Te_8. It was found that DDA could replace the OLA in the reaction, giving the same results with one change in procedure: the injection is done between 70-80 ºC to prevent the DDA from solidifying.

Characterization. The resulting solid powders were analyzed by X-ray diffraction (XRD) on a Scintag X-2 Advanced Diffraction System using Cu Kα radiation (λ=1.54 Å). Scanning electron microscopy (SEM) images were taken on a JEOL JSM-6500 F FE-SEM equipped with a Thermo Electron EDS detector. Low-resolution TEM images were obtained on a JEOL JEM 2000 at an accelerating voltage of 160 kV. High resolution Transmission electron microscopy (TEM) images were taken using a Phillips CM200 STEM with an accelerating voltage of 200 kV. The TEM is equipped with a Princeton Gamma Tech Prism 2000 EDS detector, which was used for elemental analysis

of the product. TEM samples were prepared by dip-casting a sonicated solution of the nanoparticles in hexanes onto carbon-coated copper TEM grids (200 mesh, Ted Pella). X-ray photoelectron spectroscopy (XPS) data was obtained using a Physical Electronics PHI 5800 ESCA System. Magnetic measurements were obtained on a JEOL MPMS SQUID Magnetometer.

1.3 Results and Discussion

The reaction method discussed in the Experimental section yielded a black powder, which was analyzed first using X-ray diffraction (XRD). The results are shown in Figure 1.1, with the collected data indexing to the trigonal Cr_5Te_8 (JCPDS 00-050-1153). There do not appear to be any additional phases or other crystalline products, as all peaks index to the Cr_5Te_8.

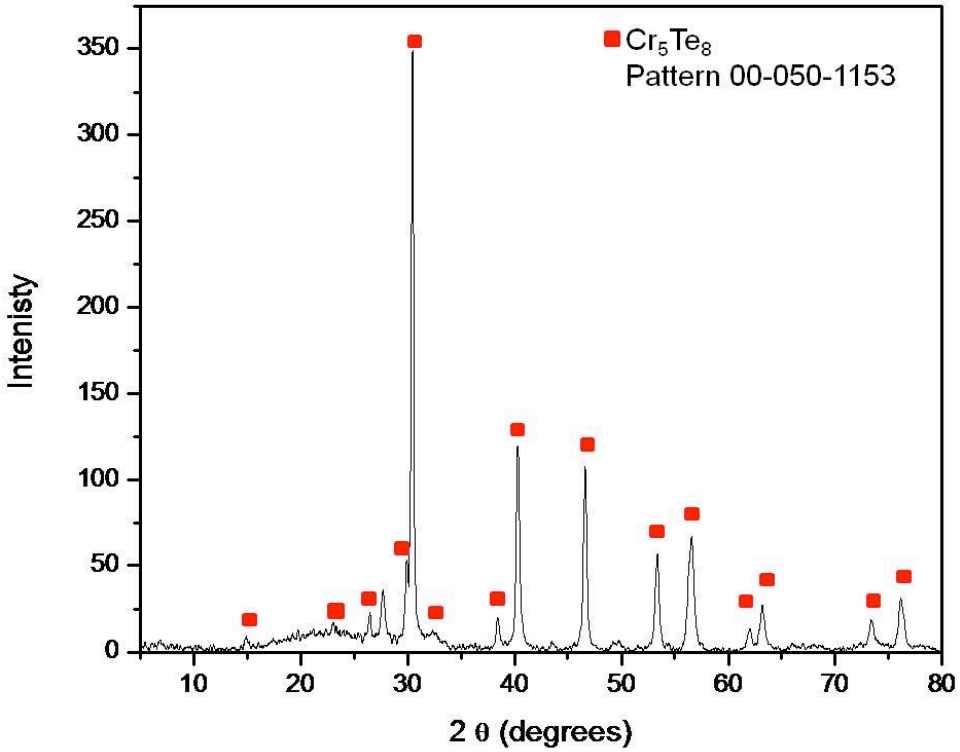

Figure 1.1: X-ray powder diffraction pattern of the solid product. All peaks index to trigonal Cr_5Te_8 (JCPDS 00-050-1153).

After the resulting product was confirmed, the size and morphology of the particles was established using SEM and TEM. From the SEM images presented in Figure 1.2, the resulting product is thin platelets approximately 15 nm thick. It was difficult to determine the other dimensions of the platelets, as the amount of agglomeration prevented a good image of a flat platelet. It became clearer why this was so challenging upon TEM analysis. In the TEM images there is evidence of the nanoplatelets rolling into scrolls, a phenomenon that happens in nanomaterials that involve a layered structure. TEM images are presented in Figure 1.3 in which there is a high-resolution side-view image of a rolled "scroll".

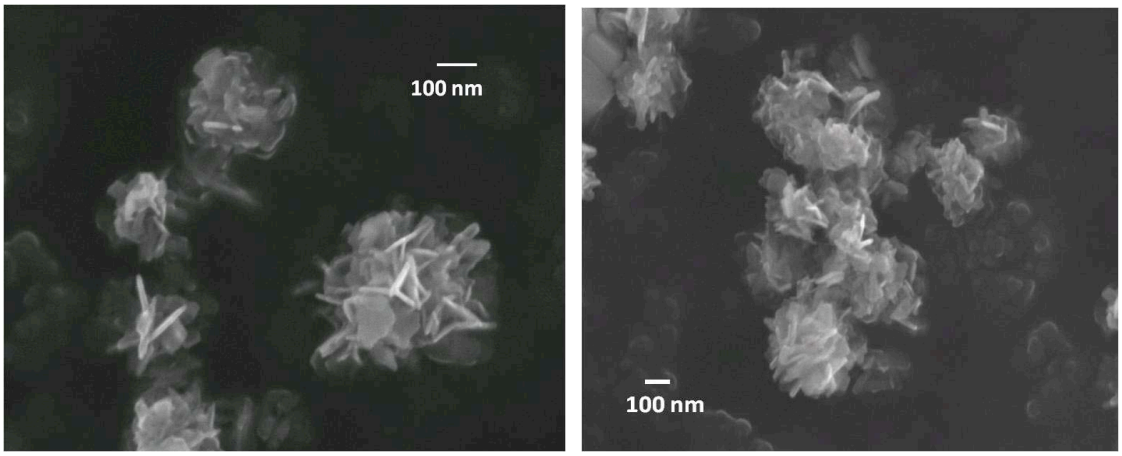

Figure 1.2: SEM images of the Cr_5Te_8 platelets. The nanoparticles are approximately 15 nm thick. Analysis of their other dimensions is difficult due to rolling and possibly stacking.

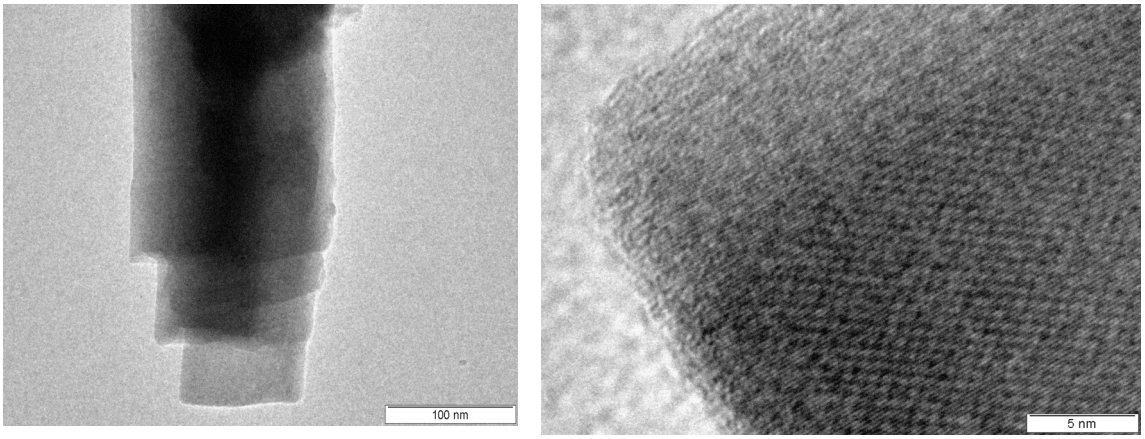

Figure 1.3: HR-TEM images of the Cr_5Te_8 platelets. Image on the left shows a side view of a platelet that has rolled into a scroll. Left shows the edge of the scroll.

It is very intriguing that the resulting product of this reaction is the 5:8 stoichiometric compound. The structure of the material is a five-layer superstructure of the simple CdI_2 structure type. The compound is mixture of chromium (III) and chromium (IV), with a 4:1 ratio of Cr^{3+}:Cr^{4+}. The two precursors used in the synthesis are $CrCl_2$. The initial oxidation state of the chromium is 2^+ and ends as a mixture of 3^+ and 4^+, which means that a redox reaction is occurring during the hot injection reaction. It is unlikely that this can be attributed to the oleylamine, as amines are typically considered to be reducing. It is possible that this could be attributed to the trioctylphosphine. One of the known impurities of this surfactant is trioctylphosphine oxide (TOPO). It is possible that the redox reaction is occurring between the chromium (II) and the TOPO, oxidizing the chromium (II) to the mixture of chromium (III) and (IV) while reducing the TOPO to TOP.

The next step in the analysis of the Cr_5Te_8 is to compare the magnetic properties for the nanoplatelets to that data reported for the bulk in the literature. Magnetic data was obtained on a superconducting quantum interference device (SQUID). The magnetic moment was measured while sweeping the temperature from liquid helium temperatures (5 K) to 300K. These results are shown in Figure 1.4 and the bulk data are reproduced from reference (60) in Figure 1.5 in order to make a visual comparison of the data. Comparing with the bulk data the shape of the curve is the same while the transition temperature for the nanoparticles is lower than that of the bulk: the transition to ferromagnetism occurs at around 220 K in the bulk and around 200 K in the nanoplatelet Cr_5Te_8 sample.[60] The most obvious difference from the bulk to the nano-sample is the added feature located at ~20 K. This could be indicitive of an additional low-temperature

magnetic ordering, or there is also the possibility that there is an amorphous impurity phase. The other major difference is in the scale of the magnetic component on the y-axis. The data for the nanoplatelets gives significantly lower values than that of the bulk. This difference in values could be attributed to the fact that the nanoplatelets likely have residual organic surfactant on the surface, affecting the value of the mass used in the calculation, lowering the final value.

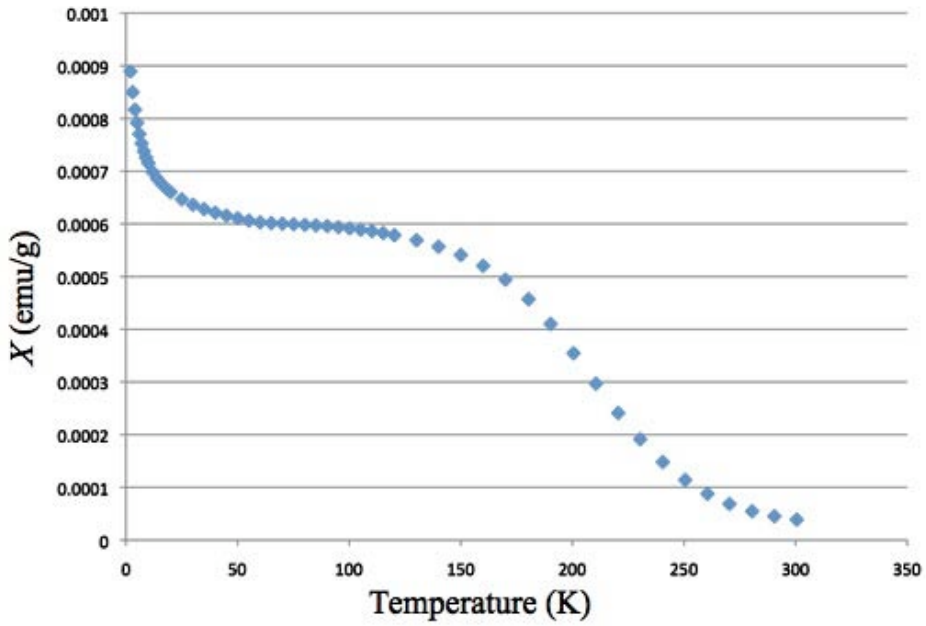

Figure 1.4: Magnetic susceptibility as a function of temperature. Note the two observed transition temperatures at ~220 K and ~20 K.

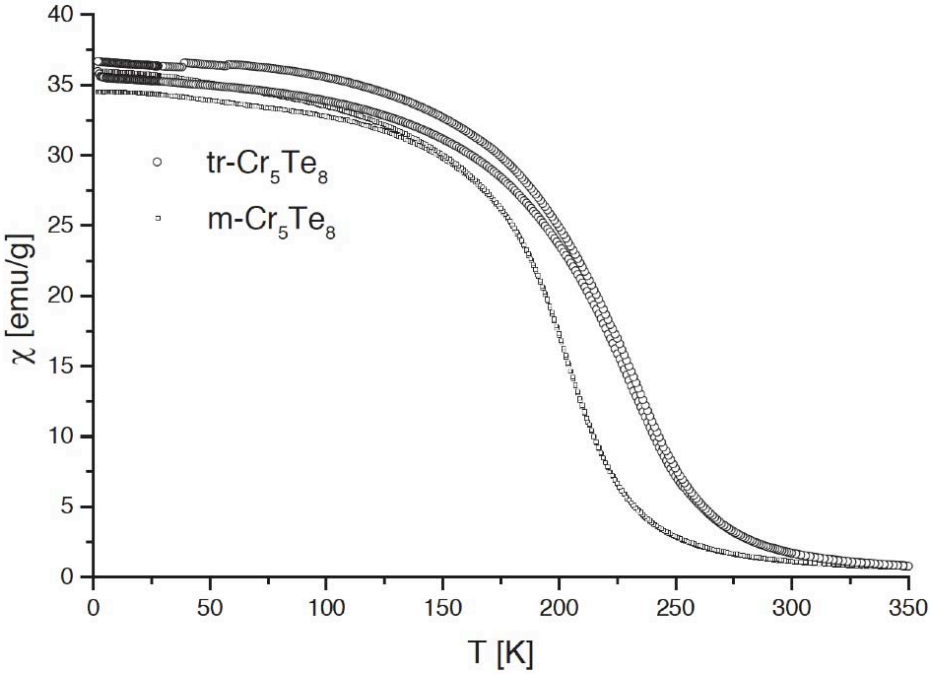

Figure 1.5: Magnetic susceptibility as a function of temperature for the bulk material. This work was reproduced from reference (60) for the purpose of comparing the bulk data with that of the naoparticles.

In order to determine if the low-temperature feature can be attributed to an amorphous impurity in the product an attempt to collect XPS data on the Cr_5Te_8 was made. Chromium and tellurium XPS analysis yield near-identical spectra, with peaks close enough that even longer high-resolution scans cannot resolve them. In the meantime, limitations of the reaction were being explored and it was found that the exact same parameters can be used to make the pure selenium analogue, as well as chromium sulfides. Preliminary analysis on these products has been done. XRD confirmation of the products is found in Figure 1.6 for the selenium reaction and in Figure 1.7 for the sulfur reaction. It is interesting that the sulfur and selenium analogues readily form from the reaction without any adjustment of the parameters. This will allow for a more thorough investigation of this family of materials in the future.

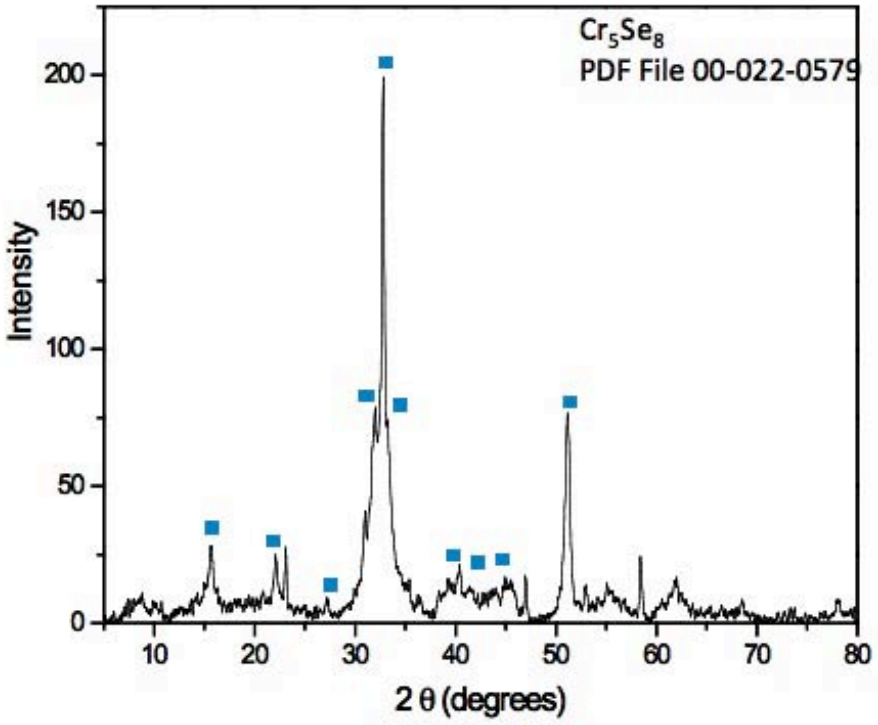

Figure 1.6: XRD data for the selenium reaction. Most peaks index to Cr_5Se_8, with a few left unindexed that did not match any of the chromium tellurides, chromium chloride or selenium powder.

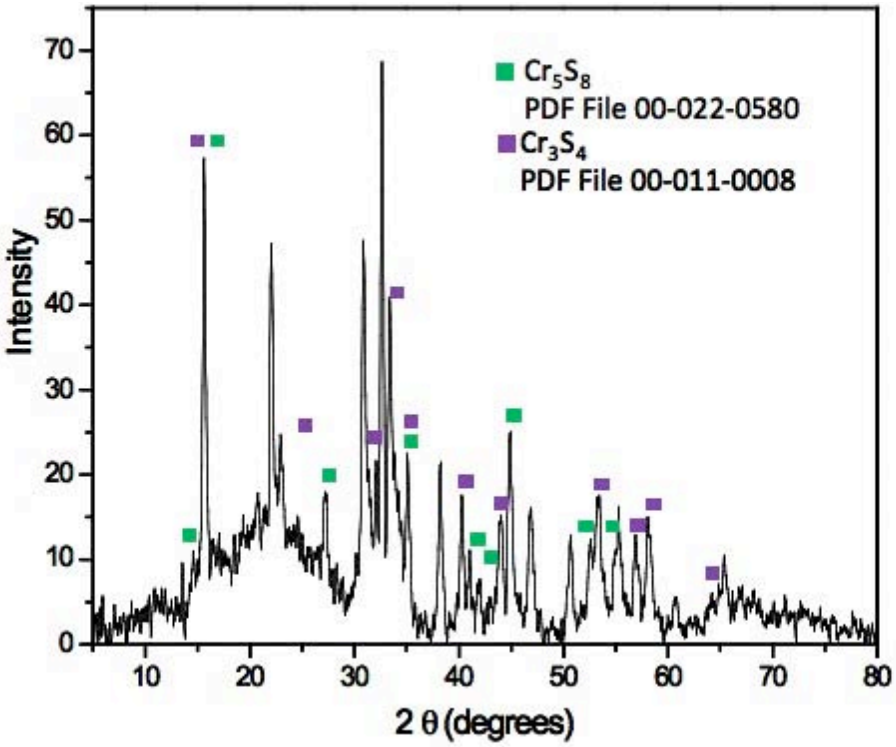

Figure 1.6: XRD data for the sulfur reaction. Peaks index to multiple Cr-S compounds.

XPS data could now be obtained to check for impurities resulting from the reaction, as the problem of overlapping peaks does not arise for Se and Cr, as it does for Te and Cr. The XPS results for the Cr_5Se_8 are shown in Figure 1.8, which shows the survey scan, and Figures 1.9 and 1.10, showing high-resolution data for the chromium and selenium respectively.

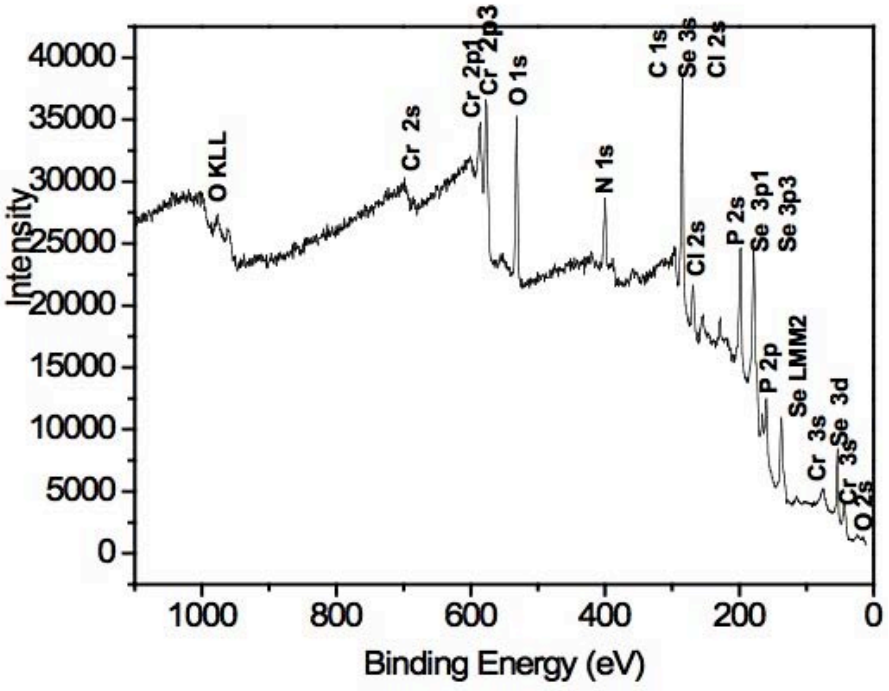

Figure 1.8: XPS survey scan of the Cr_5Se_8 product. Note the phosphorus and nitrogen peaks, which are likely from residual surfactant. There are also Cl peaks present, which could indicate that some chloride is left over from the synthetic reaction.

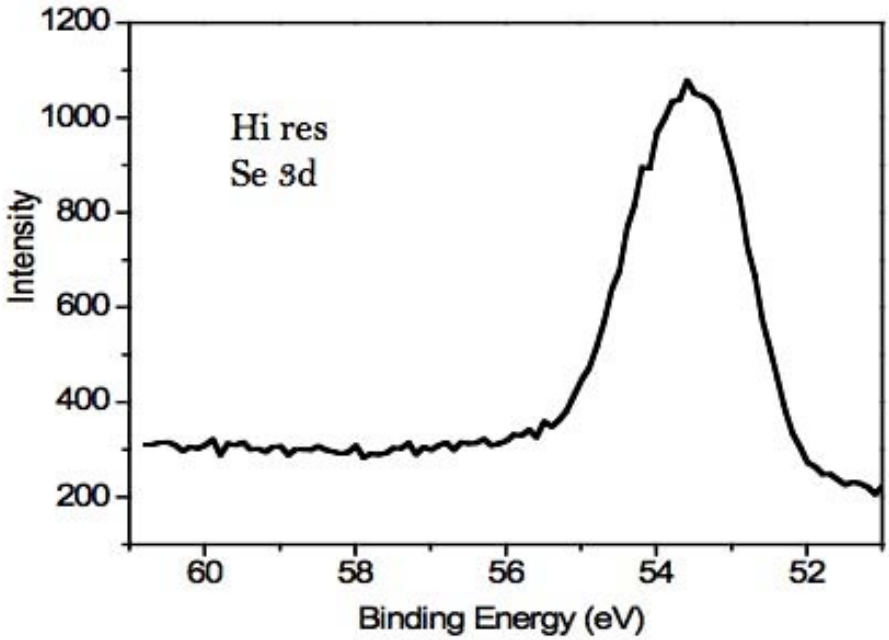

Figure 1.9: High resolution scan of the Se-3d peak. Demonstrates that only one oxidation state exists in the sample for selenium.

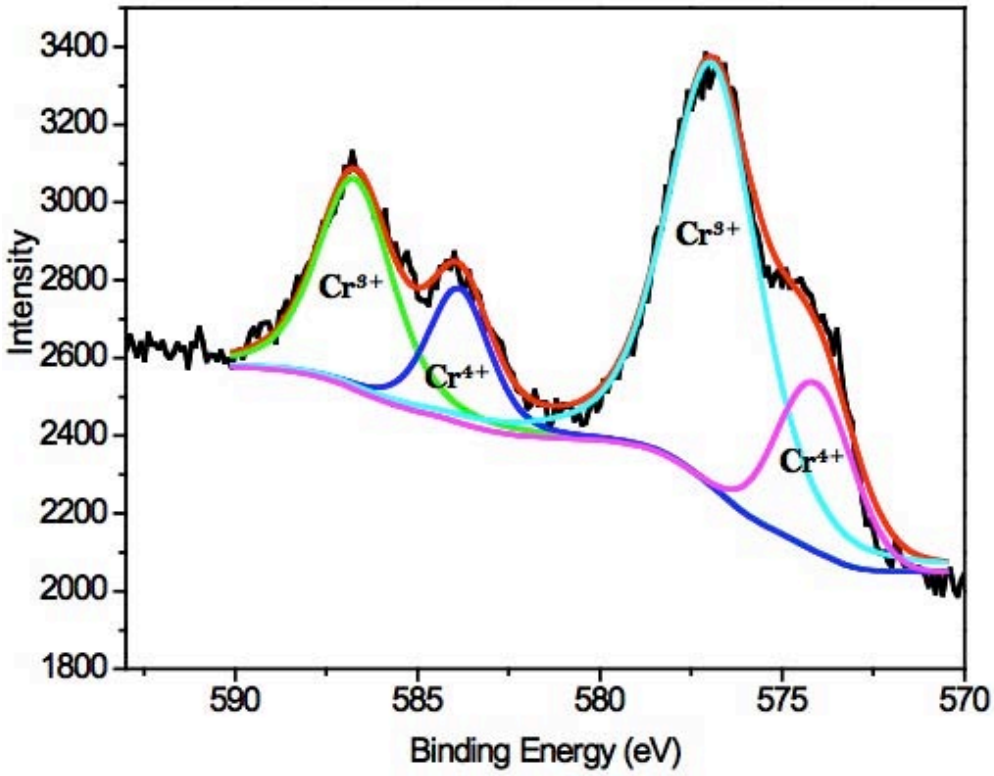

Figure 1.9: High-resolution scan of the chromium. Fitting the peaks confirms that there is Cr^{3+} and Cr^{4+} in the sample, as would be expected.

1.4 Conclusions

The survey scan shows evidence of residual organics, as evidenced by the presence of nitrogen and phosphorus, from the OLA and TOP, respectively. It is also important to note the presence of chloride peaks. It is possible that there is there is an amorphous chromium chloride impurity still remaining in the sample, despite efforts to rinse the product. This could be the origin of the added feature in the magnetic data. In the future it will be necessary to investigate this further. The high-resolution scans show the presence of one oxidation state of selenium as well as the presence of chromium (III) and chromium (IV), as would be expected.

1.4 Conclusions

A reliable synthesis for Cr_5Te_8 nanoplatelets, as a result of unexpected redox chemistry occurring during the reaction, has been developed and the product confirmed by XRD and the particle size and morphology examined using SEM and TEM. This is likely due to the choice of surfactant: trioctylphosphine (TOP). The oxidized version, trioctylphosphine oxide (TOPO) is a known impurity in the TOP available from manufacturers. It is feasible that the oxidation/reduction reaction is occurring between the chromium (II) precursor and the fully oxidized version of the surfactant. Initial data on the magnetism has been collected and compared with the bulk, though more work remains in this area. The magnetic data that have been taken suggest that Cr_5Te_8 is not an optimal material to pursue in spintronic device fabrication, though the changes observed between the bulk and the nanoparticles are intriguing. Although there was a significant decrease in the transition temperature, the accompanying decrease in magnetic moment cannot be solely explained by residual surfactant: the drop in magnetic moment is several

orders of magnitude. This is consistent with information available in the literature suggesting that the chromium-rich CrTe has the optimal half-metallic ferromagnetic properties desired for spintronic applications. There are a number of ways to approach the task of targeting these more Cr-rich compounds in the Cr-Te family. Starting with the Cr_5Te_8 reaction presented here, and altering the conditions to favor the formation of the more chromium-rich compounds could be one possible route. Another approach might be to start with the solid product and design a solid-state conversion to remove some of the tellurium, leaving behind a more chromium-rich compound. This approach is reasonable as tellurium has a much higher vapor pressure relative to chromium, and could, therefore, be removed using proper heating parameters.

It has also been shown that selenium and sulfur analogues can be obtained without changing the reaction conditions. In the future it will be useful to explore routes to other chromium chalcogenides. This goal can be achieved by varying the hot injection reaction parameters such as temperature, time, surfactant ratio, and the precursor choice; as well as by exploring the redox chemistry that is happening. Control over the product will follow as a better understanding of the reaction is obtained.

References:

(1) Moore, G. E. *Electronics* **1965**, *38*.
(2) Keyes, R. W. *Solid-State Circuits Newsletter, IEEE* **2006**, *20*, 25.
(3) Ball, P. *Nature* **2000**, *404*, 918.
(4) Flatte, M. E. *IEEE Transactions on Electron Devices* **2007**, *54*, 907.
(5) Bandyopadhyay, S.; Cahay, M. *Nanotechnology* **2009**, *20*, 412001.
(6) Prinz, G. A. *Science* **1998**, *282*, 1660.
(7) Johnson, M.; Silsbee, R. H. *Physical Review Letters* **1985**, *55*, 1790.
(8) Binasch, G.; Grunberg, P.; Saurenbach, F.; Zinn, W. *Physical Review B* **1989**, *39*, 4828.
(9) Baibich, M. N.; Broto, J. M.; Fert, A.; Dau, F. N. V.; Petroff, F.; Etienne, P.; Creuzet, G.; Friederich, A.; Chazelas, J. *Physical Review Letters* **1988**, *61*, 2472.
(10) Datta, S.; Das, B. *Applied Physics Letters* **1990**, *56*, 665.
(11) de Groot, R. A.; Mueller, F. M. *Physical Review Letters* **1983**, *50*, 2024.
(12) Dowben, P. A.; Skomski, R. *Journal of Applied Physics* **2004**, *95*, 7453.
(13) Groot, R. A. d.; Mueller, F. M.; Engen, P. G. v.; Buschow, K. H. J. *Journal of Applied Physics* **1984**, *55*, 2151.
(14) Fang, C. M.; Wijs, G. A. d.; Groot, R. A. d. *Journal of Applied Physics* **2002**, *91*, 8340.
(15) Galanakis, I. *Journal of Physics: Condensed Matter* **2002**, *14*, 6329.
(16) Galanakis, I.; Dederichs, P. H.; Papanikolaou, N. *Physical Review B* **2002**, *66*, 174429 (9pp).
(17) Galanakis, I.; Dederichs, P. H.; Papanikolaou, N. *Physical Review B* **2002**, *66*, 134428 (10pp).
(18) Pickett, W. E.; Singh, D. J. *Physical Review B* **1996**, *53*, 1146.
(19) Singh, D. J.; Pickett, W. E. *Physical Review B* **1998**, *57*, 88.
(20) Kamper, K. P.; Schmitt, W.; Guntherodt, G.; Gambino, R. J.; Ruf, R. *Physical Review Letters* **1987**, *59*, 2788.
(21) Leuken, H. v.; Groot, R. A. d. *Physical Review B* **1995**, *51*, 7176.
(22) Lewis, S. P.; Allen, P. B.; Sasaki, T. *Physical Review B* **1997**, *55*, 10253.
(23) Penicaud, M.; Siberchicot, B.; Sommers, C. B.; Kubler, J. *Journal of Magnetism and Magnetic Materials* **1992**, *103*, 212.
(24) Irkhin, V. Y.; Katsnel'son, M. I. *Physics-Uspekhi* **1994**, *37*, 659.
(25) Park, J.-H.; Vescovo, E.; Kim, H.-J.; Kwon, C.; Ramesh, R.; Venkatesan, T. *Nature* **1998**, *392*, 794.
(26) Weng, H.; Kawazoe, Y.; Dong, J. *Physical Review B* **2006**, *74*, 085205.
(27) Galanakis, I.; Mavropoulos, P. *Physical Review B* **2003**, *67*, 104417.
(28) Lee, J. I.; Hong, S. C.; Jang, Y.-R. *Journal of Magnetism and Magnetic Materials* **2007**, *310*, 2250.
(29) Pask, J. E.; Yang, L. H.; Fong, C. Y.; Pickett, W. E.; Dag, S. *Physical Review B* **2003**, *67*, 224420.
(30) Sanyal, B.; Bergqvist, L.; Eriksson, O. *Physical Review B* **2003**, *68*, 1.
(31) Sasioglu, E.; Galanakis, I.; Sandratskii, L. M.; Bruno, P. *Journal of Physics: Condensed Matter* **2005**, *17*, 3915.

(32) Xie, W.-H.; Xu, Y.-Q.; Liu, B.-G.; Pettifor, D. G. *Physical Review Letters* **2003**, *91*, 037204.
(33) Xing, Y.; Liu, Y.; Li, S.-N.; Zhao, Y.-H.; Xie, W.-H. *Physica Status Solidi b* **2010**, *247*, 2268.
(34) Kanomata, T.; Sugawara, Y.; Kaneko, T.; Kamishima, K.; Aruga Katori, H.; Goto, T. J. *Journal of Alloys and Compounds* **2000**, *297*, 5.
(35) Block, T.; Tremel, W. *Journal of Alloys and Compounds* **2006**, *422*, 12.
(36) Comstock, R. L.; Lissberger, P. H. *Journal of Applied Physics* **1970**, *41*, 1397.
(37) Kraschinski, S.; Herzog, S.; Bensch, W. *Solid State Sciences* **2002**, *4*, 1237.
(38) Sreenivasan, M. G.; Teo, K. L.; Jalil, M. B. A.; Liew, T.; Chong, T. C.; Du, A. Y. *IEEE Transactions on Magnetics* **2006**, *42*, 2691.
(39) Zhang, J. H.; Birdwhistell, T. L. T.; O'Connor, C. J. *Solid State Communications* **1990**, *74*, 443.
(40) Liu, Y.; Bose, S. K.; Kudrnovsky, J. *Physical Review B* **2010**, *82*, 094435 (8pp).
(41) Ipser, H.; Komarek, K. L.; Klepp, K. O. *Journal of the Less-Common Metals* **1983**, *92*, 265.
(42) Bensch, W.; Helmer, O.; Nather, C. *Materials Research Bulletin* **1997**, *32*, 305.
(43) Bi, J. F.; Sreenivasan, M. G.; Teo, K. L.; Liew, T. *Journal of Physics D: Applied Physics* **2008**, *41*, 045002.
(44) Shimada, K.; Saitoh, T.; Namatame, H.; Fujimori, A.; Ishida, S.; Asano, S.; Matoba, M.; Anzai, S. *Physical Review B* **1996**, *53*, 7673.
(45) Sreenivasan, M. G.; Bi, J. F.; Teo, K. L.; Liew, T. *Journal of Applied Physics* **2008**, *103*, 043908.
(46) Cao, G. *Nanostructures and Nanomaterials*; Imperial College Press: London, 1973.
(47) DiVentra, M.; Evoy, S.; Heflin, J. R. J. *Introduction to Nanoscale Science and Technology*; Kluwer Academic Publishers: Norwell, MA, 2004.
(48) Roduner, E. *Nanoscopic Materials: Size-Dependent Phenomena*; RCS Publishing: Cambridge, 2006.
(49) Murray, C. B.; Norris, D. J.; Bawendi, M. G. *Journal of the American Chemical Society* **1993**, *115*, 8706.
(50) Peng, Z. A.; Peng, X. *Journal of the American Chemical Society* **2001**, *123*, 183.
(51) Peng, Z. A.; Peng, X. *Journal of the American Chemical Society* **2002**, *124*, 3343.
(52) Peng, X.; Manna, L.; Yang, W.; Wickham, J.; Scher, E.; Kadavanich, A.; Alivisatos, A. P. *Nature* **2000**, *404*, 59.
(53) Peng, X.; Wickham, J.; Alivisatos, A. P. *Journal of the American Chemical Society* **1998**, *120*, 5343.
(54) Yin, Y.; Alivisatos, A. P. *Nature* **2005**, *437*, 4165.
(55) Wang, Y.-H. A.; Bao, N.; Shen, L.; Padhan, P.; Gupta, A. *Journal of the American Chemical Society* **2007**, *129*, 12408.

(56) Joo, J.; Na, H. B.; Yu, T.; Yu, J. H.; Kim, Y. W.; Wu, F.; Zhang, J. Z.; Hyeon, T. *Journal of the American Chemical Society* **2003**, *125*, 11100.
(57) Wang, D.-S.; Zheng, W.; Hao, C.-H.; Peng, Q.; Li, Y.-D. *Chemistry: A European Journal* **2009**, *15*, 1870.
(58) Luther, J. M.; Law, M.; Beard, M. C.; Song, Q.; Reese, M. O.; Ellingson, R. J.; Nozik, A. J. *Nano Letters* **2008**, *8*, 3488.
(59) Panthani, M. G.; Akhavan, V.; Goodfellow, B.; Schmidtke, J. P.; Dunn, L.; Dodabalapur, A.; Barbara, P. F.; Korgel, B. A. *Journal of the American Chemical Society* **2008**, *130*, 16770.
(60) Lukoschus, K.; Kraschinski, S.; Nather, C.; Bensch, W.; Kremer, R. K. *Journal of Solid State Chemistry* **2004**, *177*, 951.

PART 2: LOCAL ATOMIC STRUCTURE STUDIES USING THEORY TO SIMULATE POLARONS IN SUPERCONDUCTING CUPRATES AND EXPERIMENT TO ANALYZE ALTERNATIVE ENERGY NANOMATERIALS

Chapter 2: Modeling the Effects of Stripes in High-T_c Superconducting Cuprates Using a Real Space Approach[ii]

2.1 Introduction

Since discovery of high-Tc superconductivity in the layered copper oxides (or cuprates) by Bednorz and Muller in 1986, much effort has been placed on studying the structural and electronic trends observed in these complex materials, trying to uncover the mechanism associated with this phenomenon[1-4] In spite of the ongoing research for the past 25 years following this groundbreaking discovery, possible mechanisms for superconductivity are still the subject of extensive debate. Although agreement on the mechanism for superconductivity remains elusive, certain aspects of the material are well understood. The cuprates take on a perovskite-type structure, and the superconducting properties result from the movement of electrons through the copper-oxygen layers, with the surrounding lanthanum/strontium layers stabilizing the structure while providing means to dope the parent compound with holes or electrons.[5] As the parent compound, $La_{2-x}Sr_xCuO_4$, is doped with charge carriers superconductivity arises. The phase diagram shows that there is a very specific doping/temperature region in which the material is superconducting.[6-9] Another key conclusion that researchers agree on is that cuprate superconductivity arises form the formation of Cooper pairs, two electrons bound in a

[ii] Simulation boxes and interatomic potentials used in this work were developed by Juan S. Lezama-Pacheco, A. David Andersson, and Luis A. Casillas-Trujillo. The data herein were obtained by Angel J. Garcia-Adeva and Mary B. Martucci.

paired state at low temperatures, a phenomenon first described by Leon Cooper in 1956.[10-13]

There have been several key developments in this field to progress the understanding of high T_c superconductivity. The presence of structural instabilities near the transition temperature was demonstrated by means of XAFS, $YBa_2Cu_3O_7$ and other related compounds.[14,15] It was suggested that these instabilities could be explained as strong electron-lattice interactions, i.e. polarons, with evidence suggesting these play an important role in the superconducting properties of this class of materials.[16-19] Further evidence emerged in support of these results including unconventional isotope effects in both the optimally and underdoped regime, as well as Angle Resolved Photoemission (ARPES) experiments.[20-26] A key feature is the dynamic nature of these structural instabilities, as evidenced by XAFS, inelastic X-ray scattering and ultra-fast optical probes, suggesting lattice fluctuations, and not static structural instabilities.[18,22,27] Bianconi and coworkers modeled these lattice fluctuations as ordered atomic displacements in a quasi-2D pattern now known as stripes (Bianconi-Saini-Oyanagi stripes, B-S-O stripes).[28-30] The stripes arise at a temperature T* that corresponds with the opening of a gap in the electronic density of states that has come to be known as pseudo-gap.[21,22,25,31-36] Although much research has focused on understanding these stripes, the role that these B-S-O stripes have in the mechanism of high-Tc superconductivity has yet to be revealed.[37-41] Our goal is to try to increase the understanding of how these lattice fluctuations interact with charged particles and see if they lead to some kind of self-organization (such as pairing) or other phenomena.

Using a real space approach to model charge-structure relationships by means of empirical potentials that describe the elastic properties of a given system, we want to simulate the effects of polarons in the cuprate lattice. The material is described by means of short and long-range forces, making these simulations useful in modeling charge-lattice interactions, though magnetic effects are left out. We have studied the interaction between charge and B-S-O stripes embedded in a $La_{2-x}Sr_xCuO_4$-like (LSCO) lattice, by means of Buckingham potentials, long range Coulomb forces, Morse potentials, and harmonic potentials in order to investigate the effects of these lattice fluctuations over moving charges in the Cu-O plane. The simulations are static in nature and do not include magnetic properties, but we are able to simulate the effects of these stripes as instantaneous energy landscapes in which the stripes are described by an effective field that distorts the LSCO lattice in a localized region. The results indicate that polarons favor specific sites due to the presence of the stripe and suggest long-range bipolaron formation. In a separate set o experiments we will utilize the feff program as a way to add in a magnetic component to our calculations. Feff is capable of calculating a spin-based electronic density of states for the lattice. Our hope is to demonstrate the relevance of the effects of charge and magnetism utilizing these two theoretical approaches.

2.2 Simulation Procedure

In order to simulate this complex material, two different space groups were utilized. The low-temperature orthorhombic (LTO, space group B m a b) configuration was employed, based on reference 10. The stripe is introduced into the central copper-oxygen plane of the simulation box using a modified low-temperature tetragonal structure

(LTT, space group P 42/n c m), again based on information from reference 10. A summary of the lattice information is summarized in Table 2.1 and a diagram showing the two structures can be found in Figure 2.1. In order to study the effects of charge ordering in cuprate superconductors, two $La_{2-x}Sr_xCuO_4$-type 6x10x1 simulation boxes (see Figure 2.2) were created from the LTO cuprate unit cell: one containing Bianconi-Saini stripes, the other an equivalent to the first, without the stripe. Periodic boundary conditions were applied for all simulations. The stripe was inserted in the central Cu-O plane of the simulation box and was 18 by 4 oxygen atoms in area (see Figure 2.3) The size of the simulation box was optimized so no effects due to periodicity were present.

In modifying the geometry to fit the information on the LTT and LTO geometries, the structure of the LTO for the Cu-O octahedra is tilted in the (110) direction, with two atoms in the plane and two atoms out of the plane. In the modified LTT structure, the tilting of the Cu octahedra is in the (100) direction and approximately ten times as much as occurs in the LTO structure (see Figure 2.1 and Table 2.1).

Table 2.1: Summary of crystallographic information for the LSCO lattice.

	Structure	**Space Group**	**a (Å)**	**b (Å)**	**c (Å)**	**Description**
Cuprate unit cell	Low-teperature orthorhombic (LTO)	*B m a b*	5.329	5.339	13.199	Tilting of Cu-O octahedra in (110) direction; two atoms in, two out of the plane
B-S-O stripe	Low-temperature tetragonal (LTT)	$P\ 4_2 / n\ c\ m$	5.317	5.317	13.199	Tilting of Cu-O octahedra ~10 times as much as LTO in (100) direction

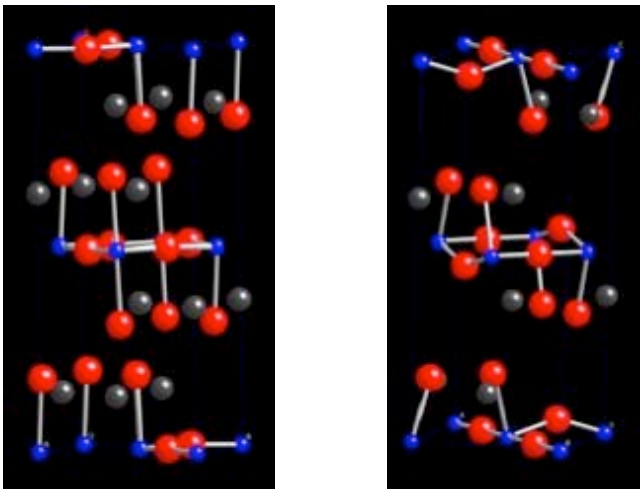

Figure 2.2: Left shows the modified LTO structure. Right shows the modified LTT structure. Note that the tilt for the LTT geometry is ~10 times that in the LTO. Lattice mismatch is ~0.1%.

Atomic interactions within the lattice were modeled using empirical or semi-empirical potentials that include long-range Columbic forces, short-range Buckingham potentials, Morse potentials, and three body angular terms (harmonic potentials). Buckingham potentials were derived previously by LANL coworkers and modified to match structural and elastic properties within acceptable ranges for both the LTO and LTT structures in LSCO. Morse potentials were obtained from the literature.[42] Interactions involving the LTO-LTT interface were assumed to be given by either LTT or LTO potentials. It was previously shown that results are qualitatively the same for both cases. The interfacial potentials were described consistently as LTT pair potentials in this study. Simulations were run using the General Lattice Utility Program (GULP).[43] Energy minimization calculations were performed at constant pressure using a conjugate gradient algorithm for minimization.

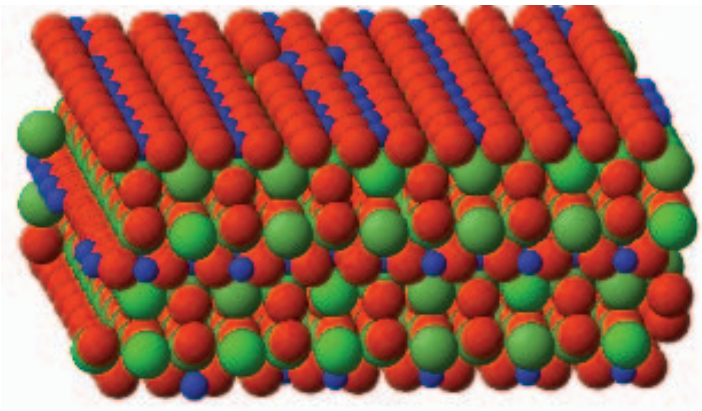

Figure 2.2: Representation of the simulation box utilized in the studies. Red represents O; blue corresponds to Cu; green indicates La/Sr sites. Note the central copper-oxygen plane. This is the part of the lattice in which the stripe was inserted.

In order to investigate effects of charge organization in the LSCO lattice, charged O^- defects (+1 hole = O^{-1}) were inserted at specific sites within the central Cu-O plane of the simulation box. Buckingham terms were included to account for the charge lattice interaction depending on the site occupied by these charges. These charged defects are representative of the mobile "polarons" observed within the material. Placing one of these O^- species in one of the oxygen sites in the simulation box creates a charge imbalance. In order to remedy this, charge balance was achieved by the introduction of Sr dopants substituting for La atoms in the LSCO lattice distributed over the entire lattice in a disordered fashion, making the occupation of Sr per La site is $x=n_{charge}/N_{La}$. It is not necessary to assign this substitution to a Sr-doping level within the superconducting region for this material, as Buckingham and three body terms are the same regardless of the % substitution of Sr atoms. This provides a convenient way to achieve charge balance in the simulation box.

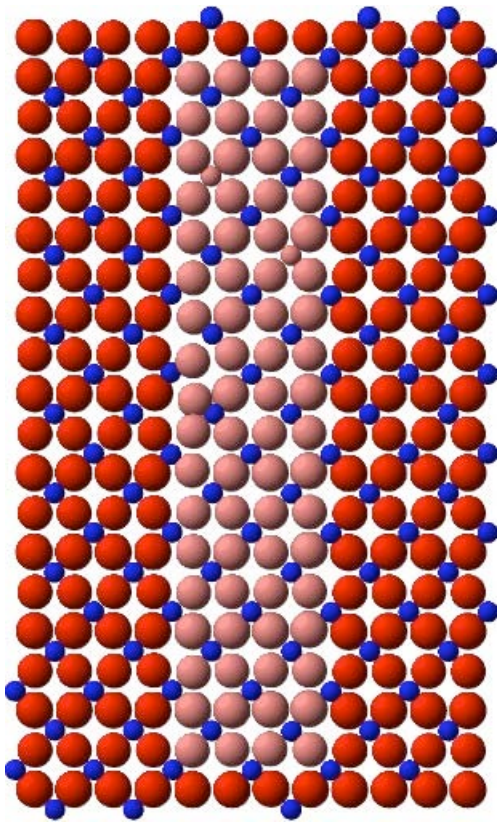

Figure 2.3: Side view of the central Cu-O plane of the simulation box. Red circles represent oxygen sites, blue indicate copper and the pink circles indicate where the stripe was located.

The lattice was then relaxed via GULP yielding several output files including a Cartesian coordinates file of the relaxed lattice and an output file that shows the cycling of the energy relaxation which include the total lattice energy value following the energy minimization.We were then able to introduce various numbers of these “polarons” into our simulation box and observe trends in the total energy of the system, specifically comparing the lattice containing the stripe to one without a stripe. The initial studies lead to the investigation of possible pairing interactions in cases involving multiple polarons as well as changing the symmetry of the stripe to create “fractal” configurations in the lattice. The specific cases studied will be described in detail in the results and discussion section to follow.

2.3 Results and Discussion

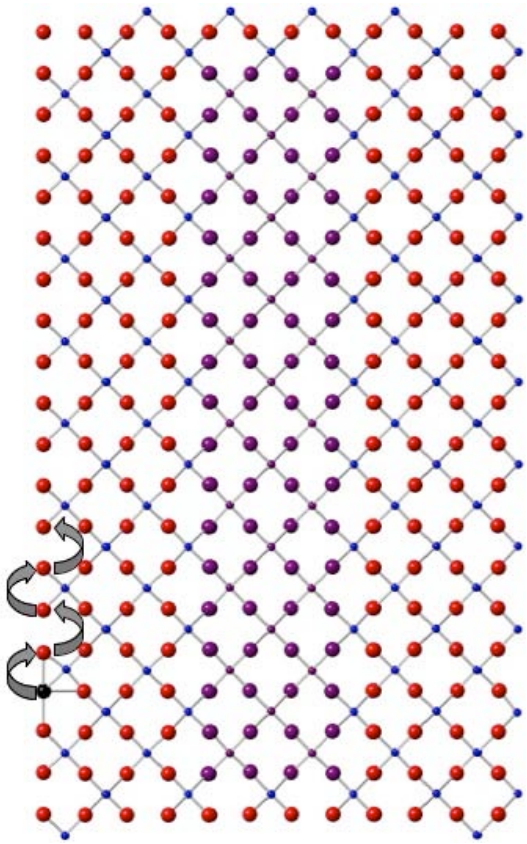

Figure 2.4: Schematic depicting the methodology for the single-polaon system simulation. One "mobile" polaron (black circle) is moved to every oxygen site on the Cu-O plane. Red shows the LTO phase; purple represents the location of the stripe. Changes in the total lattice energy were observed as the polaron is moved to each site.

For the single-polaron system, one "mobile" O^- polaron was moved through all 240 oxygen sites in the central Cu-O plane. A schematic of this process is depicted in Figure 2.4. Moving the polaron to each oxygen site yields a total lattice energy value. The data can be plotted as a 3-D energy landscape (see Figure 2.5), showing the total lattice energy as a function of the position of the polaron in the copper-oxygen plane. This energy landscape shows the most stable location of the polaron as an energy minimum. Looking at the top view of the same energy landscape, shown in Figure 2.6, there are clear energetic trends observed within the central Cu-O plane.

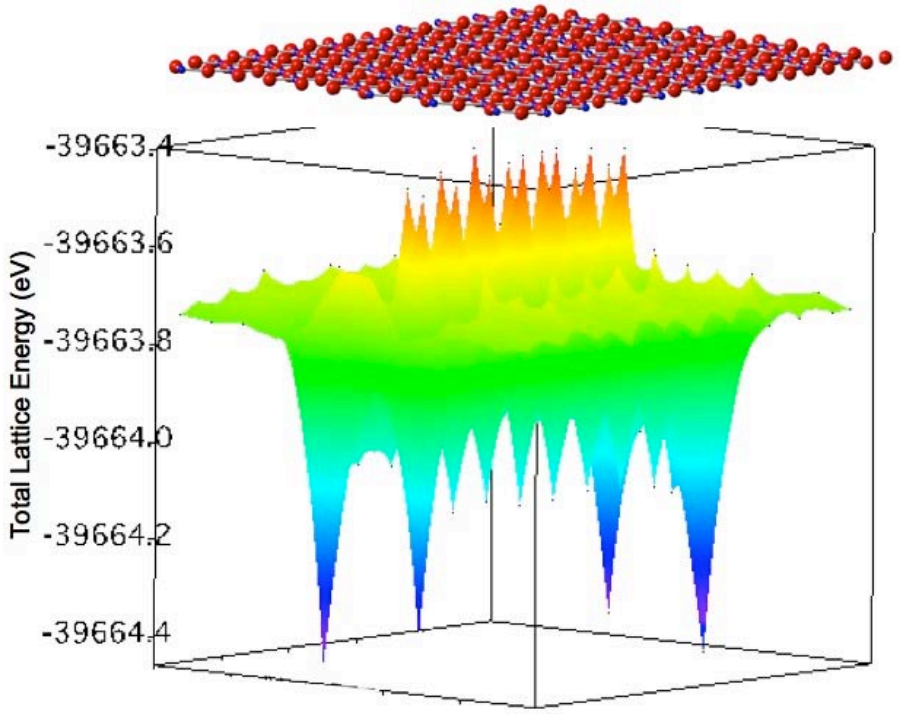

Figure 2.5: Total lattice energy as a function of the position of the polaron (x,y coordinates) on the copper-oxygen plane.

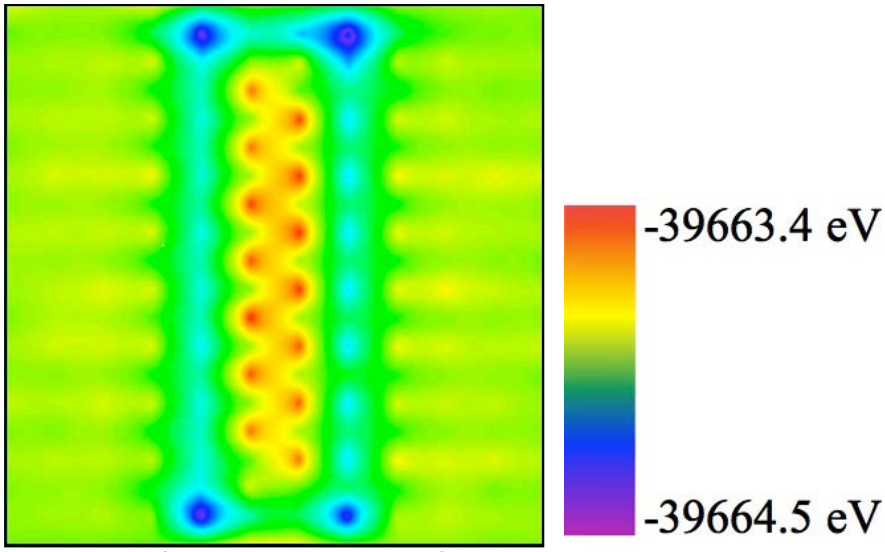

Figure 2.6: Top view of the energy landscape for the single polaron system including a stripe in the central Cu-O plane. Total lattice energy was calculated for each unique case as the mobile polaron is moved to each oxygen site available.

It is clear from Figures 2.5 and 2.6 that a higher energy configuration occurs inside the stripe; moving away from the stripe into the LTO the energy remains

consistently around the same value; energy minima are found at the interface, in particular at the corners. The resulting energy landscape shows that energy minima are found at the interface, with the lowest minima occurring at the four corners of the LTT stripe. These results give reasonable values for energy differences from the baseline energy values, the LTO energy results located away from the stripe, to the minima and maxima that occur in the plot.

Subsequently, a pure LTO case, omitting the LTT stripe, was created to compare with the LTT-LTO data. The mobile O^- polaron was again placed on each oxygen site within the copper-oxygen plane in the simulation box. These results are presented in Figures 2.7. It is clear from comparing the data for the stripe case to the pure LTO results that the addition of the stripe directly influences where the polaron will find an energy minimum. The energy minima that arise in the stripe case at the LTT-LTO boundary are likely due to additional volume resulting from the interfacing of two different space groups.

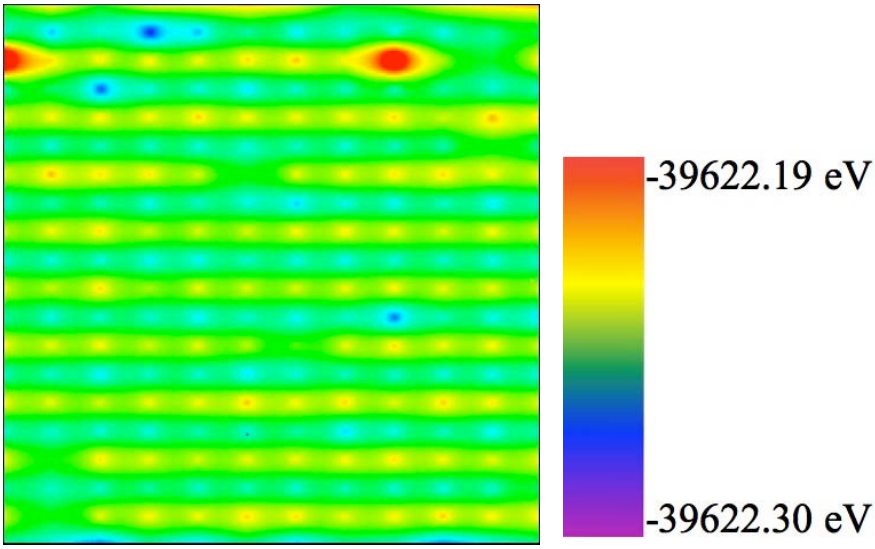

Figure 2.7: Top view of the energy landscape for the single polaron system in the pure LTO lattice (LTO stripe is excluded). Total lattice energy was calculated for each unique case as the mobile polaron was moved to each oxygen site available.

For the two-polaron (bipolaron) system, the first, "stationary", O^- polaron was pinned at one of the ten unique planar oxygen sites on the stripe-bulk interface. The second "mobile" polaron was moved through every other oxygen site in the central Cu-O plane. A schematic of this process is depicted in Figure 2.8. These simulations yield an energy landscape, showing the total lattice energy as a function of the position of the polaron. These energy landscapes, presented in Figure 2.9.a- 2.9.j, again show the most stable location of the polaron as an energy minimum. There are clear energetic trends within the central Cu-O plane. It is clear from the plots that a higher energy configuration occurs inside the stripe; moving away from the stripe into the LTO the energy is at a baseline; energy minima are found at the interface.

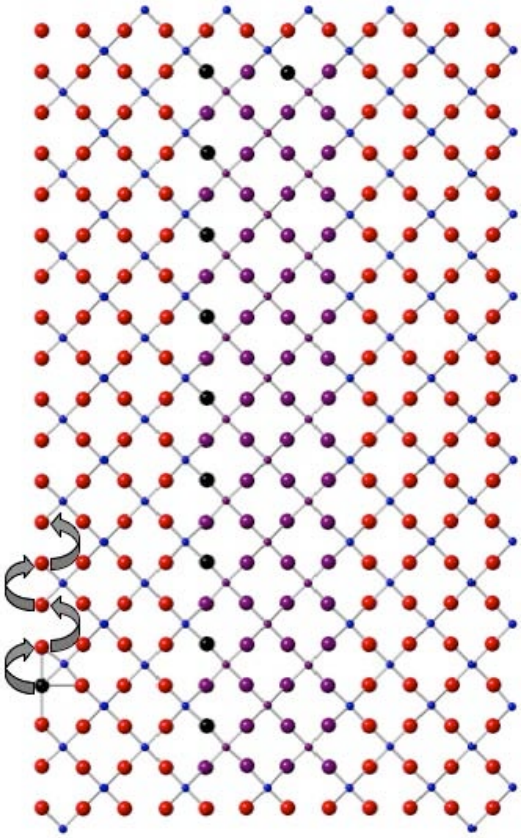

Figure 2.8: Schematic depicting the methodology for the two-polaron system simulations. One polaron is pinned at one of the ten unique O sites on the LTT-LTO interface (black circles) while the second "mobile" polaron is moved to every other unique oxygen site (red and purple) in the Cu-O plane.

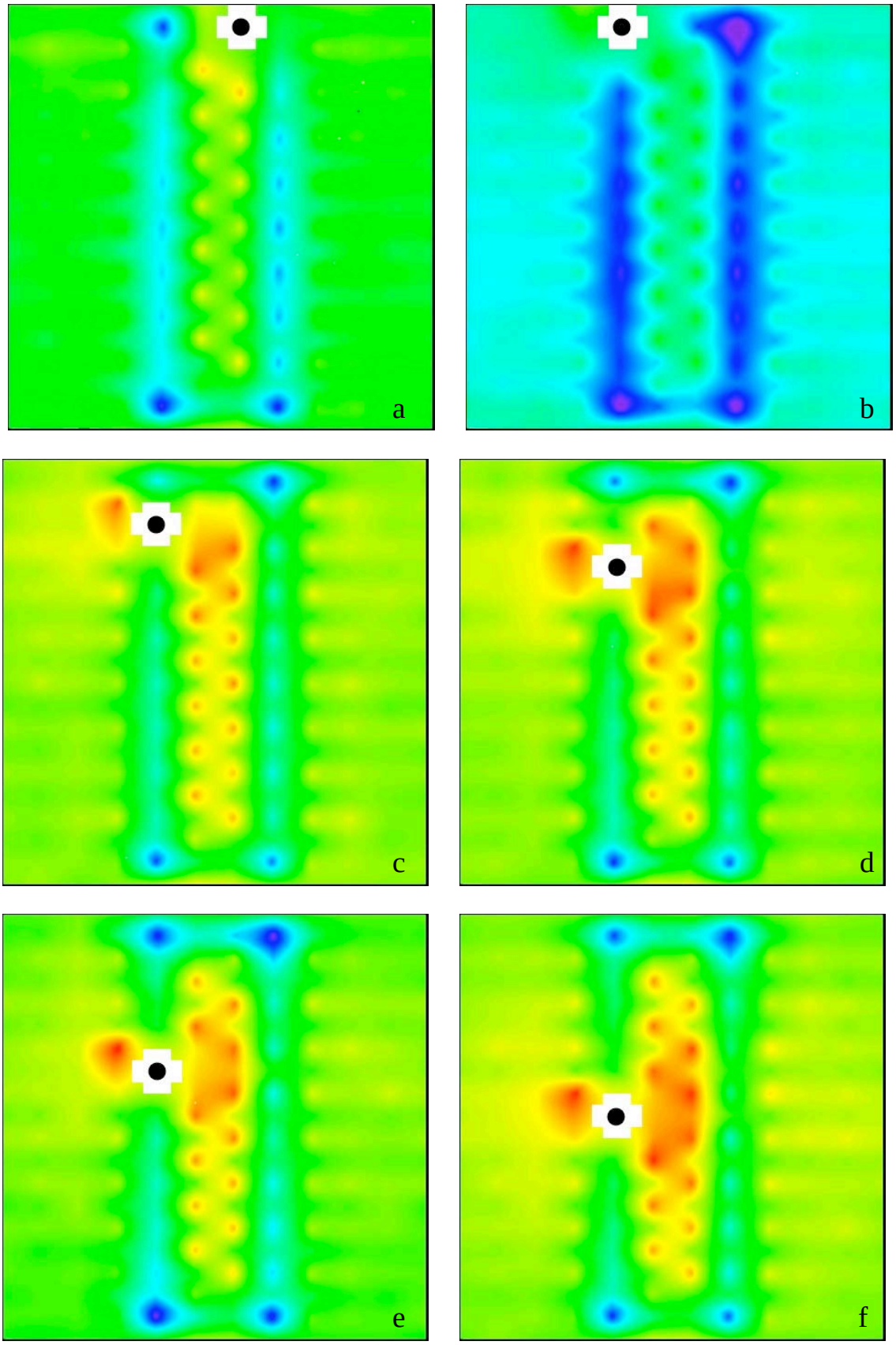
a
b
c
d
e
f

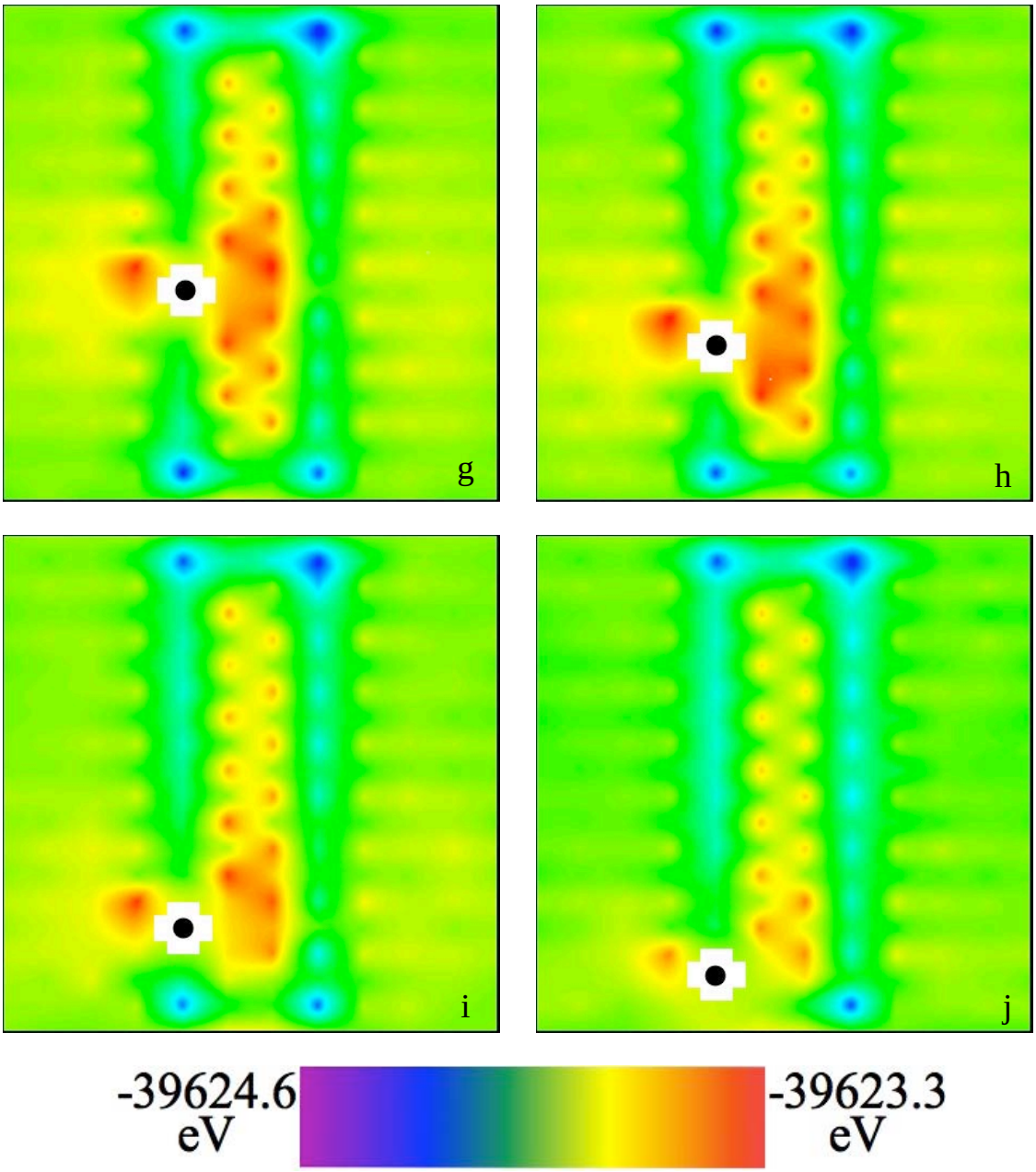

Figure 2.9.a-j: Top view of the energy landscape for the bipolaron system including a stripe in the central Cu-O plane. For each separate image, the black dot indicates the stationary polaron at the LTT-LTO interface; total lattice energy is calculated for each unique bipolaron case as the mobile polaron is moved to every additional oxygen site available.

In Figure 2.9.a the stationary polaron is pinned at the top end of the stripe. The resulting energy landscape shows that energy minima are found at the interface, with the lowest minima occurring at the four corners of the LTT stripe. The stationary polaron is pinned at the corner site in Figure 2.9.b. Again the energy landscape exhibits energy

minima at the interfacial sites and higher energies inside the LTT stripe. In this particular scenario, the entire energy landscape appears to be lower relative to the rest of the bipolaron cases. This results from pinning the immobile polaron in the corner site, which is already a lower energy site. In the remaining plots (Figures 2.9.c-2.9.j) the stationary polaron is placed at the subsequent unique planar interfacial oxygen sites. In all of these cases the trends remain the same with the minimum energy site located at the interface, particularly low minima at the corners of the stripe, and higher energies inside the stripe. These results again give reasonable values for energy differences from the baseline energy values (LTO values away from the stripe) to the minima and maxima that occur in the plot, as seen with the single polaron case.

In order to confirm that the aforementioned energy trends are a direct result of the insertion of the stripe into the lattice, we can compare our LTT-LTO lattice with that of a pure LTO case. Data for ten more bipolaron cases were generated for the "non-stripe" equivalent lattice, in which the stationary polaron was placed in the ten equivalent sites as for the case that included the stripe. These results are presented in Figures 2.10.a-j. We can garner important conclusions from these plots: the first is that the addition of the stripe clearly affects where the polaron will find an energy minimum. This is expected because the addition of the stripe creates an interface within the material, thus creating a local environment with extra volume in between the two space groups, yielding energetically favorable sites for the larger O^- species. The second result inferred from these data is that in the absence of the stripe the two polarons repel each other, finding energy minima when the second polaron is moving away from the immobile one. Another obvious difference between these results is that the overall energy scale for the

pure LTO lattice is higher than that of the mixed LTO-LTT lattice. In spite of the expected added strain from interfacing two different space groups with in the copper/oxygen plane, the stripe case yields lower energy values than that of the LTO lattice. This is due to the differences in the description of the potentials for each separate case, and not necessarily that the addition of the stripe lowers the total lattice energy of the system.

In each of these figures (both for the scenarios with and without the stripe), it is also important to note again the white space immediately surrounding the stationary polaron. These represent the four nearest neighbor sites (directly above, below and to the left and right of the pinned polaron), which are excluded from these data sets. Input files were generated for these cases, but they failed to produce results in GULP. These runs gradually approach negative infinity as GULP cycles through attempting to find a global minimum. It is possible that this issue stems from a limitation of the potentials used to describe interactions among atoms in the lattice. The other possibility is that this is a result of the limitations of the minimization algorithm used by the general lattice utility program to find the lowest energy configuration of atoms. In the future it will be necessary to use a separate program to run these nearest neighbor cases in order to pinpoint the origin of this limitation and also to obtain the total lattice energy values for these scenarios.

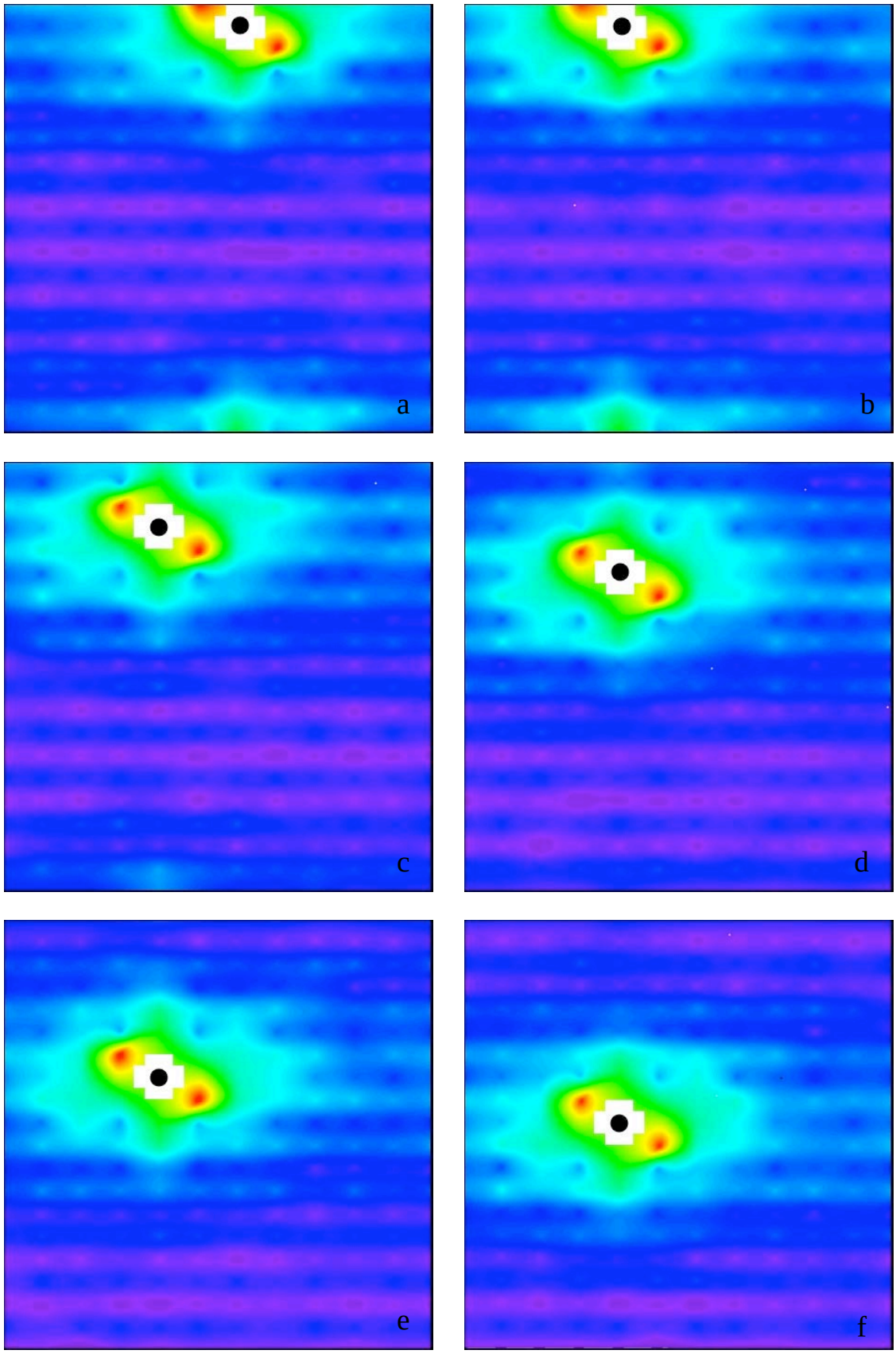
a
b
c
d
e
f

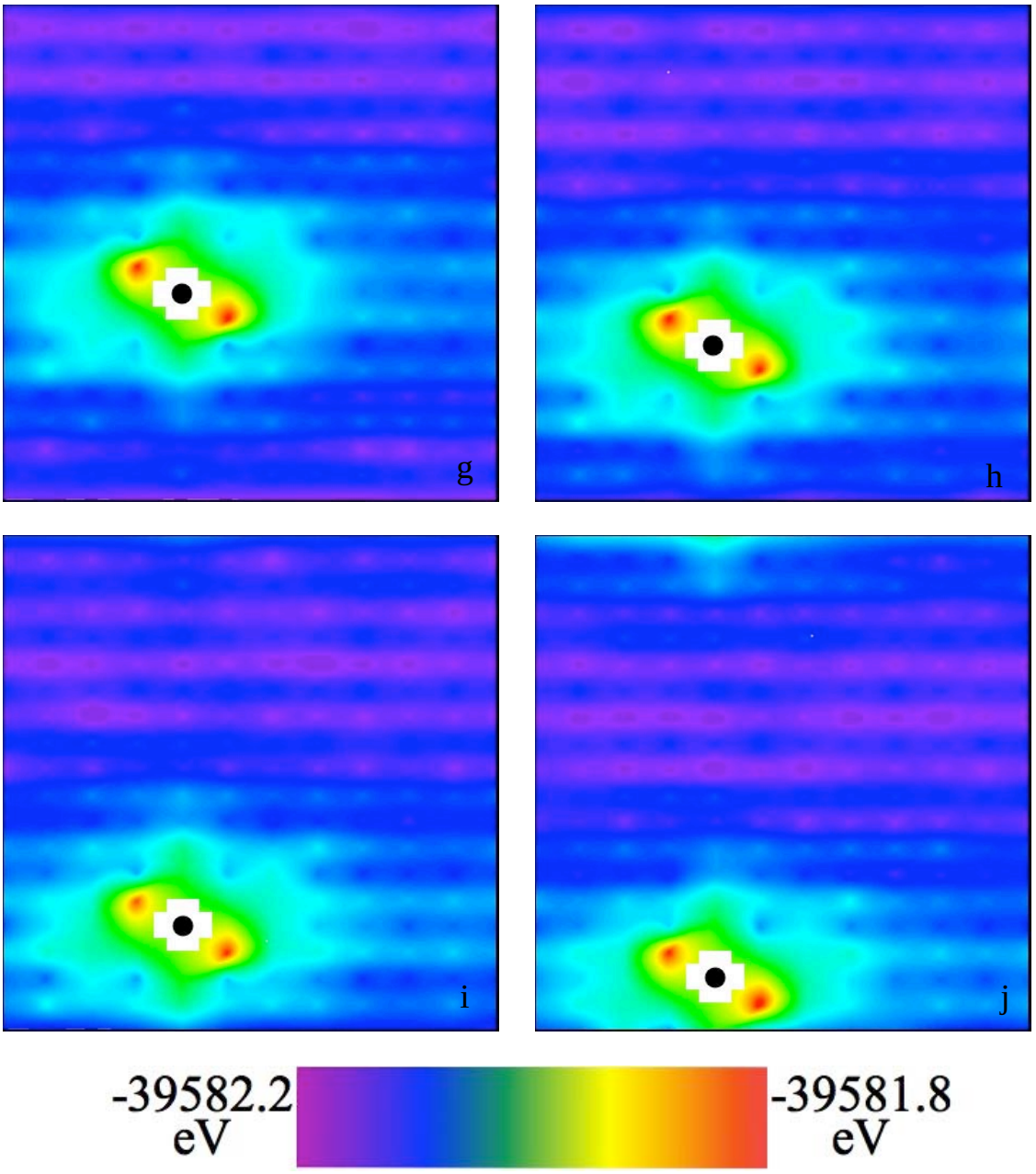

Figure 2.10.a-j: Top view of the energy landscape for the two-polaron system for the pure LTO lattice (LTT-stripe is excluded). For each separate image, the black dot indicates the stationary polaron pinned at the identical location as for the equivalent stripe case. Total lattice energy is calculated for each unique case as the mobile polaron was moved to every additional oxygen site available.

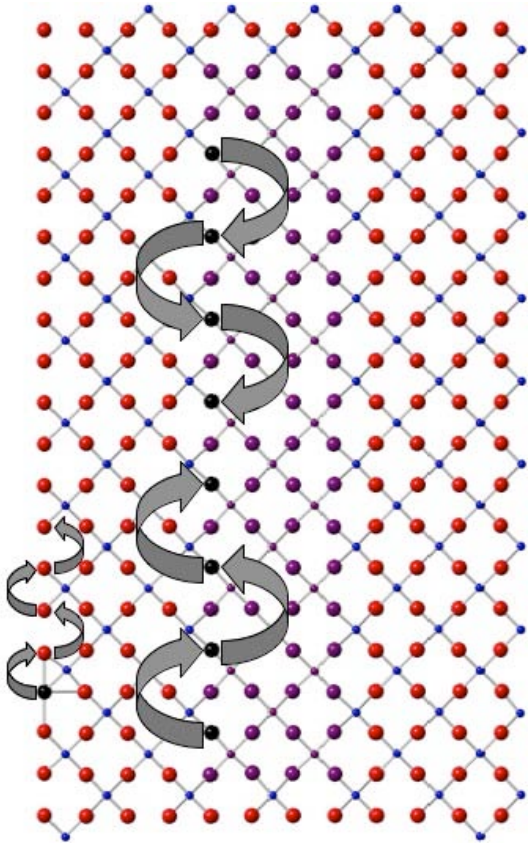

Figure 2.11: Schematic depicting the methodology for the three-polaon system simulations. Two polarons are pinned at the LTT-LTO interface (black circles) while the third "mobile" polaron is moved to every other unique oxygen site (red and purple) on the Cu-O plane. Changes in the energy landscape were observed as the positions of the two stationary polarons are moved closer to each other.

For the three-polaron systems, several different scenarios were studied in which two stationary polarons were pinned at planar interfacial oxygen sites while moving the third polaron around the remaining oxygen sites in the Cu-O plane. The first set of experiments pinned the immobile polarons as far apart as possible, without placing one on a corner site. In the successive experiments, the two stationary polarons are moved closer to each other until they are one site apart (see Figure 2.11 for a schematic). The third mobile O^- polaron is moved to all the remaining oxygen sites in the Cu-O plane and the energy landscapes generated. These results are shown in Figures 2.12.a-2.12.d.

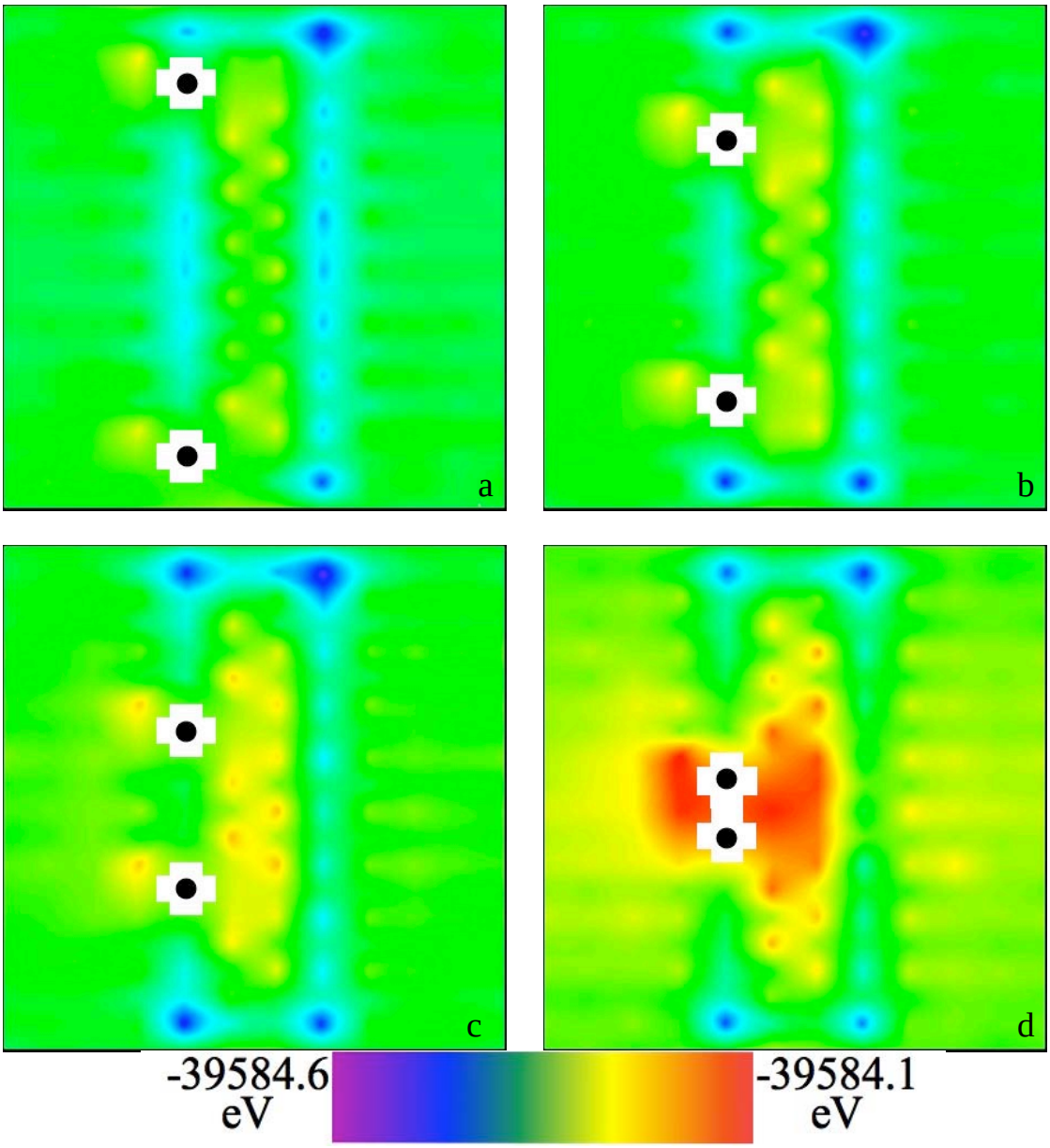

Figure 2.12.a-d: Top view of the energy landscape for the three-polaron system in which the LTT-stripe is included in the central Cu-O plane. For each separate image, the two black dots indicate the stationary polarons at the LTT-LTO interface; total lattice energy is calculated for each unique case as the mobile polaron is moved to every additional oxygen site available.

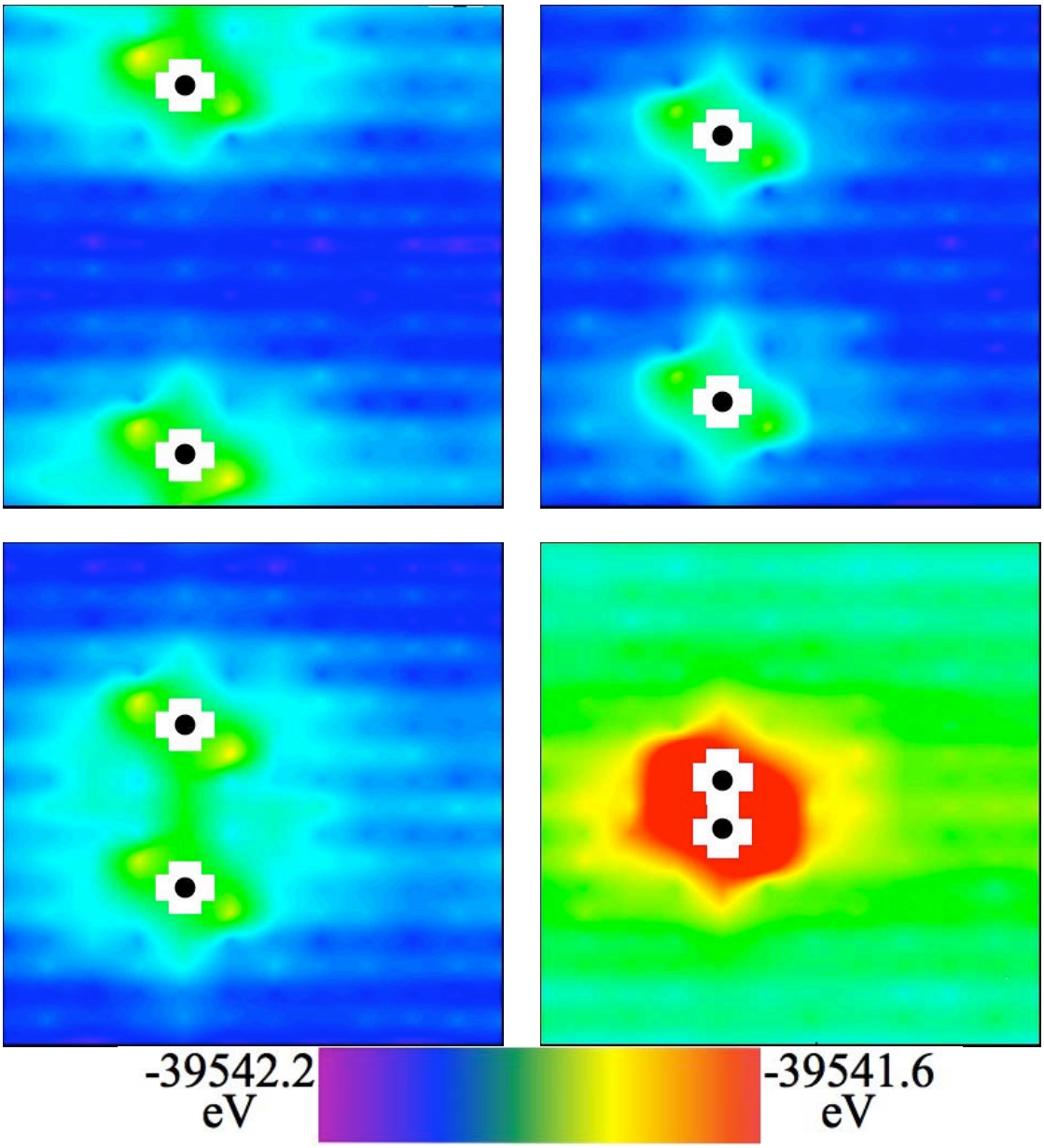

Figure 2.12a-d: Top view of the energy landscape for the three-polaron system for the pure LTO lattice (LTT-stripe is excluded). For each separate image, the two black dots indicate the stationary polarons located at the same location as for the equivalent stripe case; total lattice energy is calculated for each unique case as the mobile polaron is moved to every additional oxygen site available.

Again we observe similar trends to that of the monopolaron and bipolaron cases. The polarons find energy minima at the interface, in particular the corners and a higher energy configuration exists inside the stripe. It is also important to note that as the two pinned polarons move closer to each other, the third polaron repels them, creating the

highest energy configuration when the three polarons are closest to each other (shown in Figure 2.12.d). In comparing the stripe case with the pure LTO equivalent, it is again observed that in the case without the stripe the polarons repel each other, finding energy minima as the get further apart from each other. The stripe clearly has an effect on the where the polaron will stabilize.

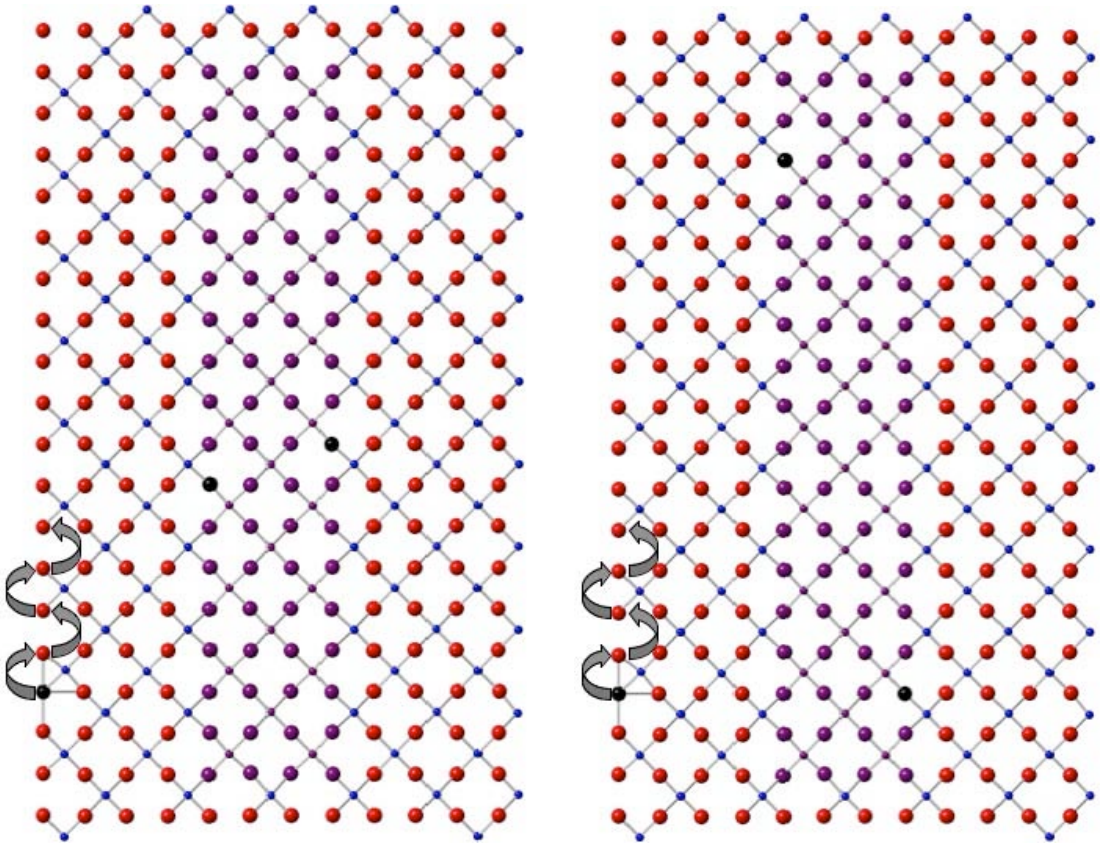

Figure 2.14: Schematic depicting the methodology for the three-polaon system simulations in which the two stationary polarons are held in close proximity to each other on eith side of the stripe, and a second case in which they are held as far apart as possible on either side of the stripe, without being placed on a corner, while the third "mobile" polaron is moved to every other unique oxygen site (red and purple) on the Cu-O plane.

In the last set of the stripe vs. pure LTO studies, two more tripolaron scenarios were run: the first placed the two pinned polarons directly across from each other on either side of the LTT stripe. The second placed them as far apart as possible on the stripe interface, without being placed in one the unique corner sites. A schematic of the

polaron placement in these simulations is depicted in Figure 2.14. Again, when the two stationary polarons are directly across from each other, the higher energy sites find significantly higher maxima than when the two pinned polarons are held as far apart as possible on the interface (see Figure 2.15). Comparing with the pure LTO phase (Figure 2.16), the polarons repel each other in the absence of the stripe.

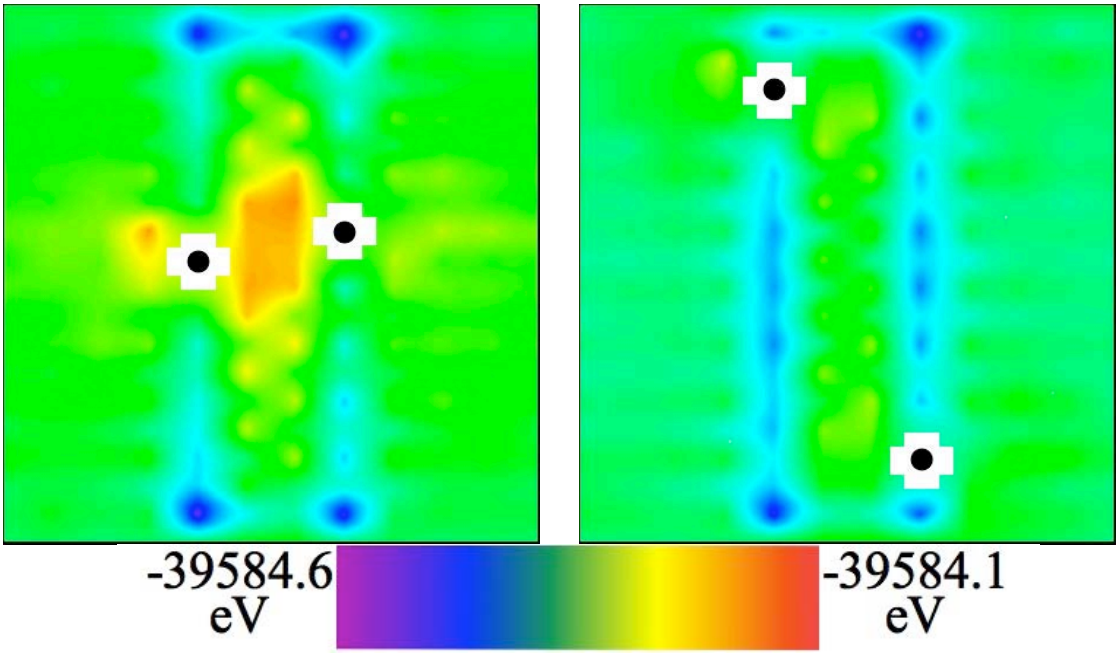

Figure 2.15: Top view of the energy landscape for the three-polaron system in which the LTT-stripe is included in the central Cu-O plane. For each separate image, the two black dots indicate the stationary polarons; total lattice energy is calculated for each unique case as the mobile polaron is moved to every additional oxygen site available.

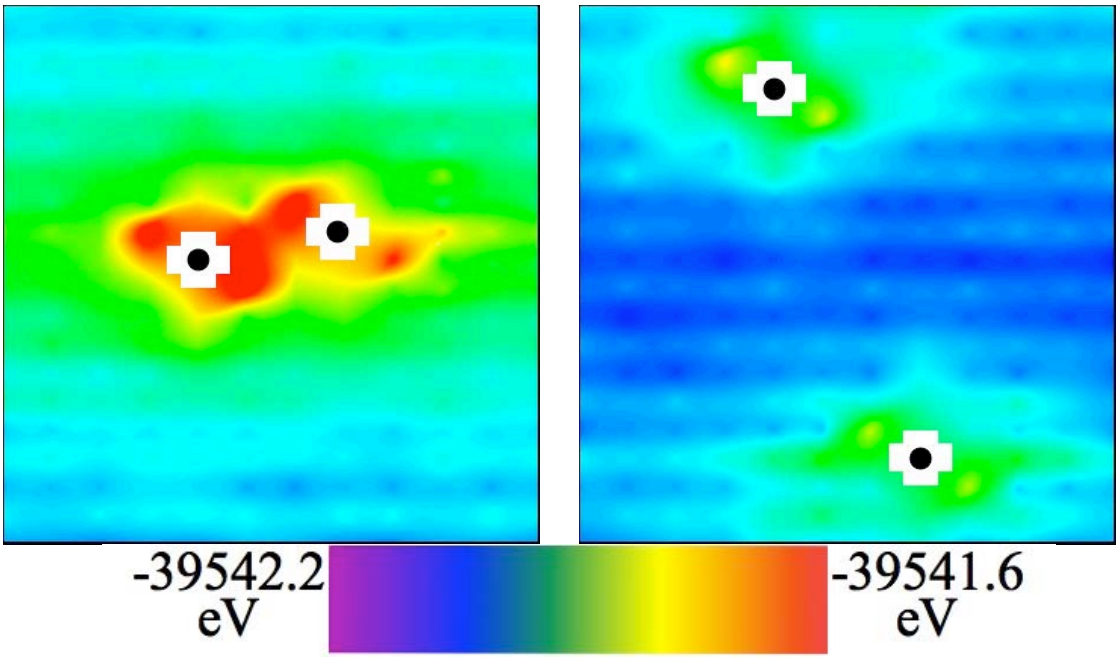

Figure 2.16: Top view of the energy landscape for the three-polaron system for the pure LTO lattice (LTT-stripe is excluded). For each separate image, the two black dots indicate the stationary polarons located at the same location as for the equivalent stripe case; total lattice energy is calculated for each unique case as the mobile polaron is moved to every additional oxygen site available.

From the total lattice energy data we can obtain another important piece of information: the pairing energy values for the bipolaron cases. This calculation determines if a bipolaron configuration is more stable than the two single polaron cases on the same two oxygen sites. The pairing energy is calculated using Equation 2.1.

$$\left(\text{Lattice energy containing no polaron} + \text{Lattice energy of the bi-polaron case for polarons 1 and 2}\right) - \left(\text{Lattice energy of polaron 1 for the single poalron case} + \text{Lattice energy of polaron 2 for the single poalron case}\right)$$

Equation 2.1: Calculation for all pairing energy results for the bipolaron systems.

The results of the calculations for all ten bipolaron cases are presented in Figure 2.17.a-j. It is important to note that although in the initial energy landscapes of the total lattice energy there were clear energetic trends exhibing high and low energy sites consistently

in the same regions on the Cu-O plane, this calculation is concerned with the bipolaron energy relative to the sum of two monopolaron energies. These data indicate when it is favorable to have bipolaron formation, meaning, when the two-polaron system is lower in energy than the sum of the two monopolaron cases in the same oxygen sites. For the results of this calculation, a negative value indicated a favorable bipolaron formation, as the overall energy is lower by having the two polarons on those sites. If the calculation results in a positive number, this indicates the energy of the system is not lowered by the bipolaron. A result of zero suggests neither a favorable or unfavorable interaction of the bipolaron. There is no difference energetically between the two one-polaron cases and the equivalent bipolaron case. It is clear from the plots that there are favorable bipolaron configurations. What is interesting to note is that there appear to be pairing interactions occurring even at longer distances across the Cu-O plane.

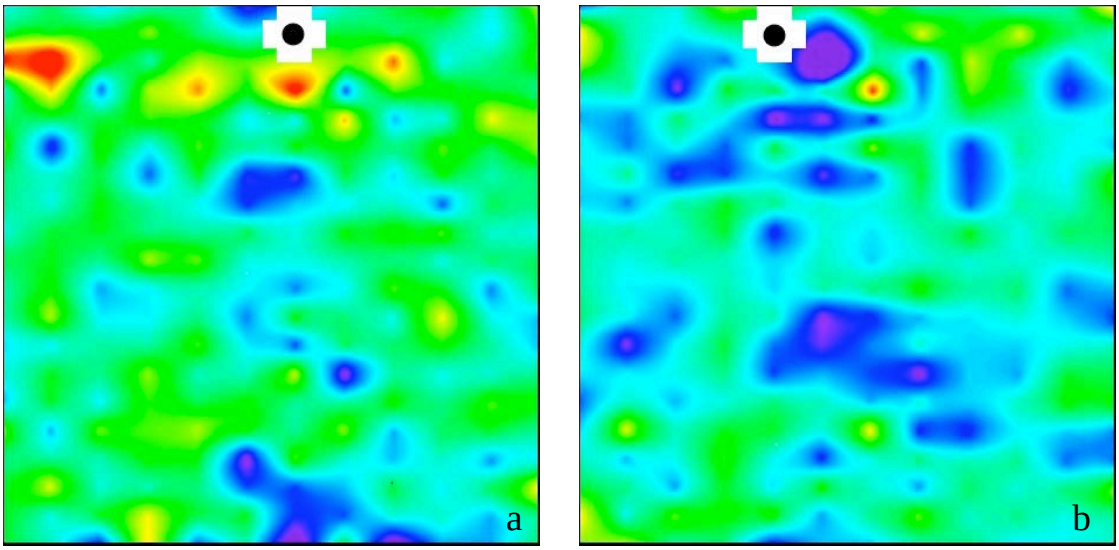

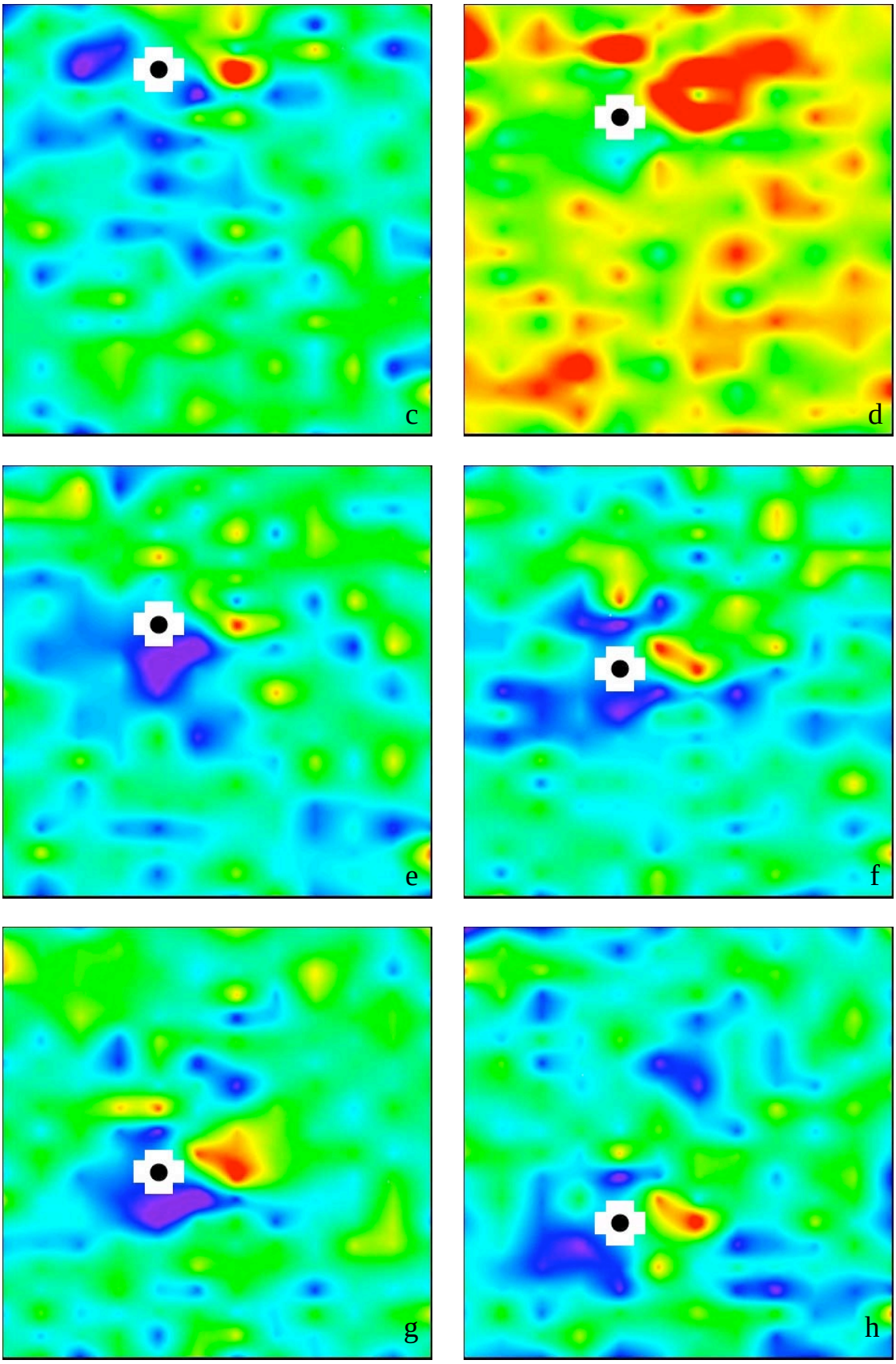
c
d
e
f
g
h

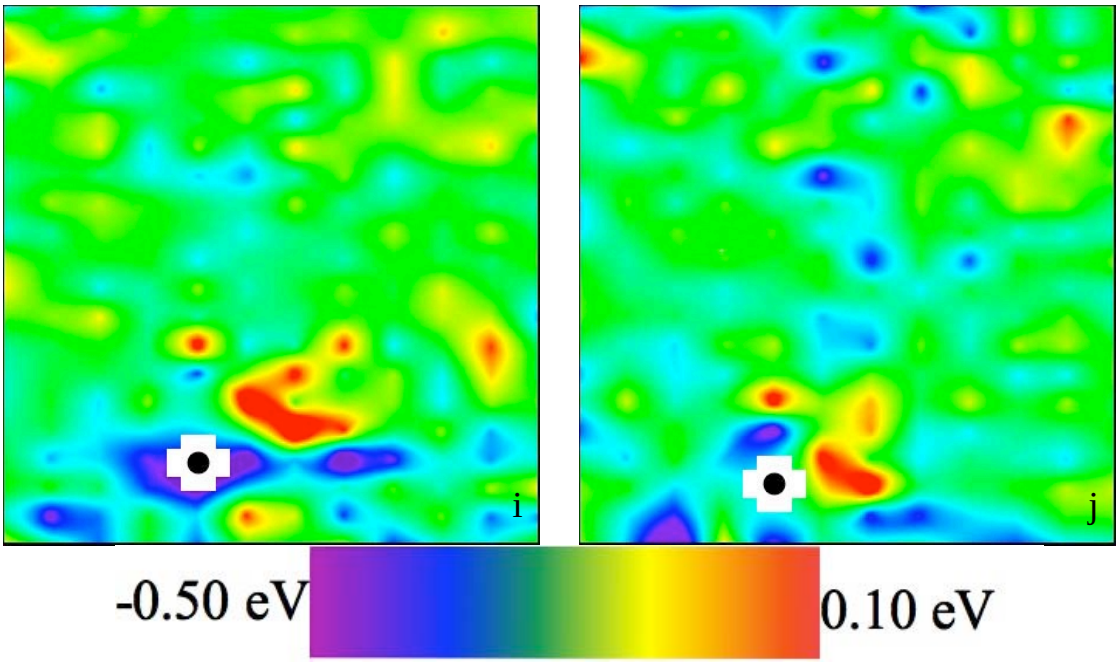

Figure 2.17.a-j: Pairing energy landscapes for the bipolaron systems. Refer to Figure 2.7 for stationary polaron placement on the interface.

These longer-range pairing interactions could be due to strain propagation through the lattice. In the future it will be necessary to further investigate this by generating displacement maps to see if there is correlation between strain and the observed lower energy bipolaron cases. It is important to note that for equivalent cases in separate systems, the pairing energy is not equivalent. For example you would expect that looking at Figures c and e, when the Figure c mobile polaron is on the equivalent of the pinned site in Figure e, it should yield the same pairing energy as when the Figure e mobile polaron is on the equivalent of the pinned site in Figure c. This is not always what is observed. It is possible that this is due to an effect of the goemtry as the lattice relaxes.

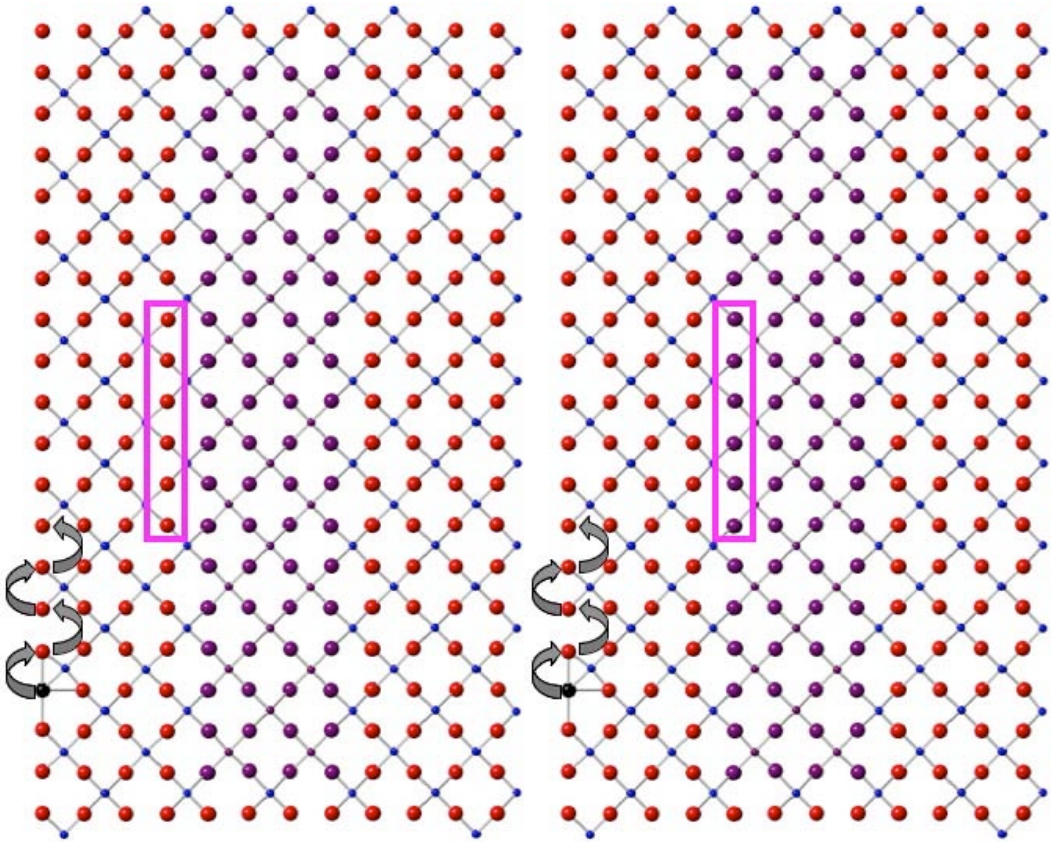

Figure 2.18: Left shows the six oxygen sites added to the stripe to create the "bump" fractal. Right diagram shows the six oxygen sites taken away from the original stripe design to create the "dent" fractal.

Recently, Bianconi and coworkers have shown that fractal distribution of dopants may enhance superconductivity using scanning synchrotron-radiation X-ray microdiffraction.[44,45] We simulated two different "fractal" stripes by creating two different asymmetrical stripes from our original stripe design. The first was a "bump" fractal with the six middle oxygens to the left of the stripe being added to the LTT stripe phase, creating a "bump" on the original stripe design (see Figure 2.18 for schematic). The second was a "dented" fractal with the six center oxygens on the left side of the stripe being added to the LTO phase, creating a sort of "dent" on the original stripe design (also shown in Figure 2.18). Bipolaron cases were run for both of these systems, pinning a staionary polaron at each of the planar oxygen sites on the interface.

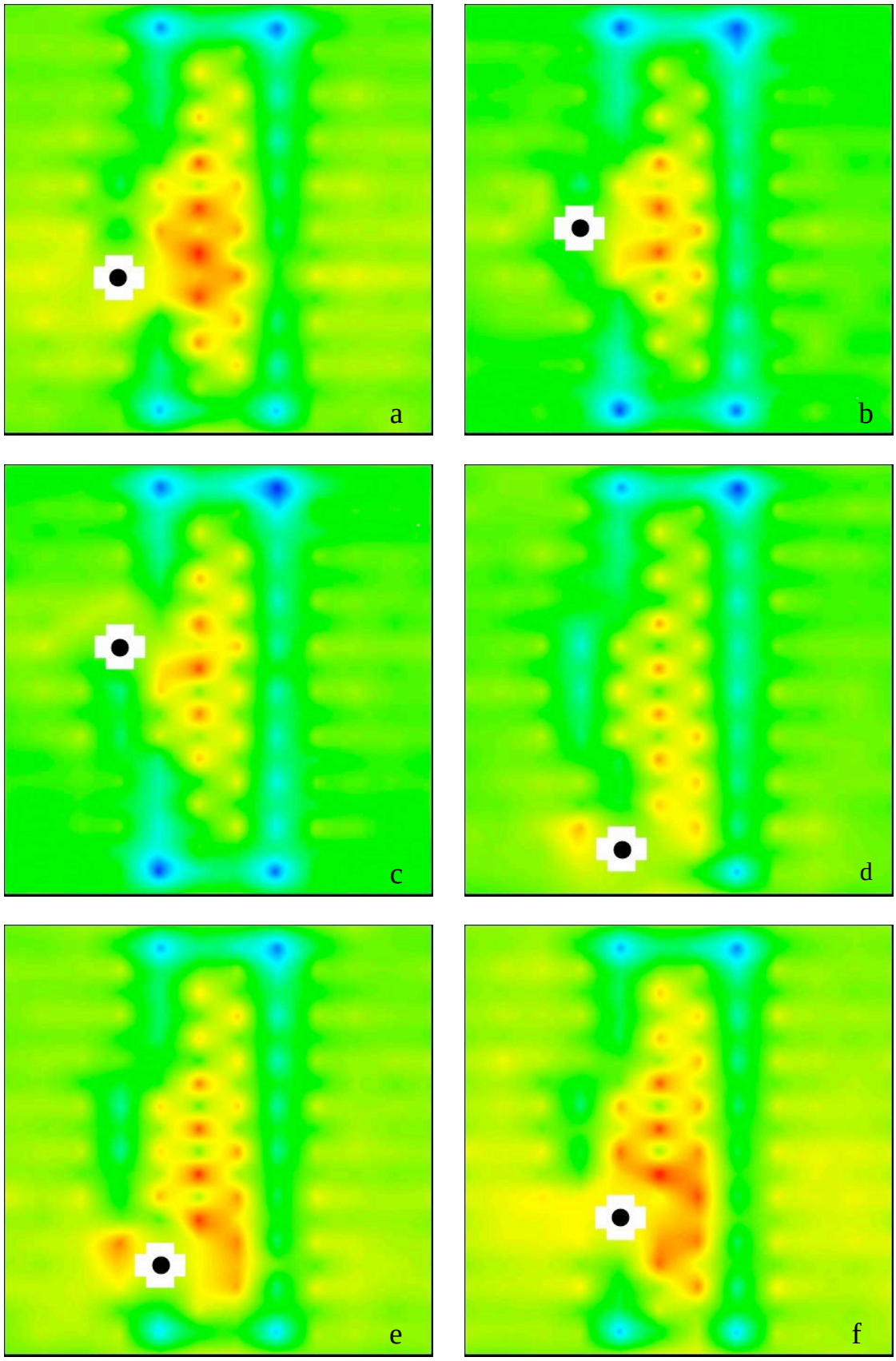
a
b
c
d
e
f

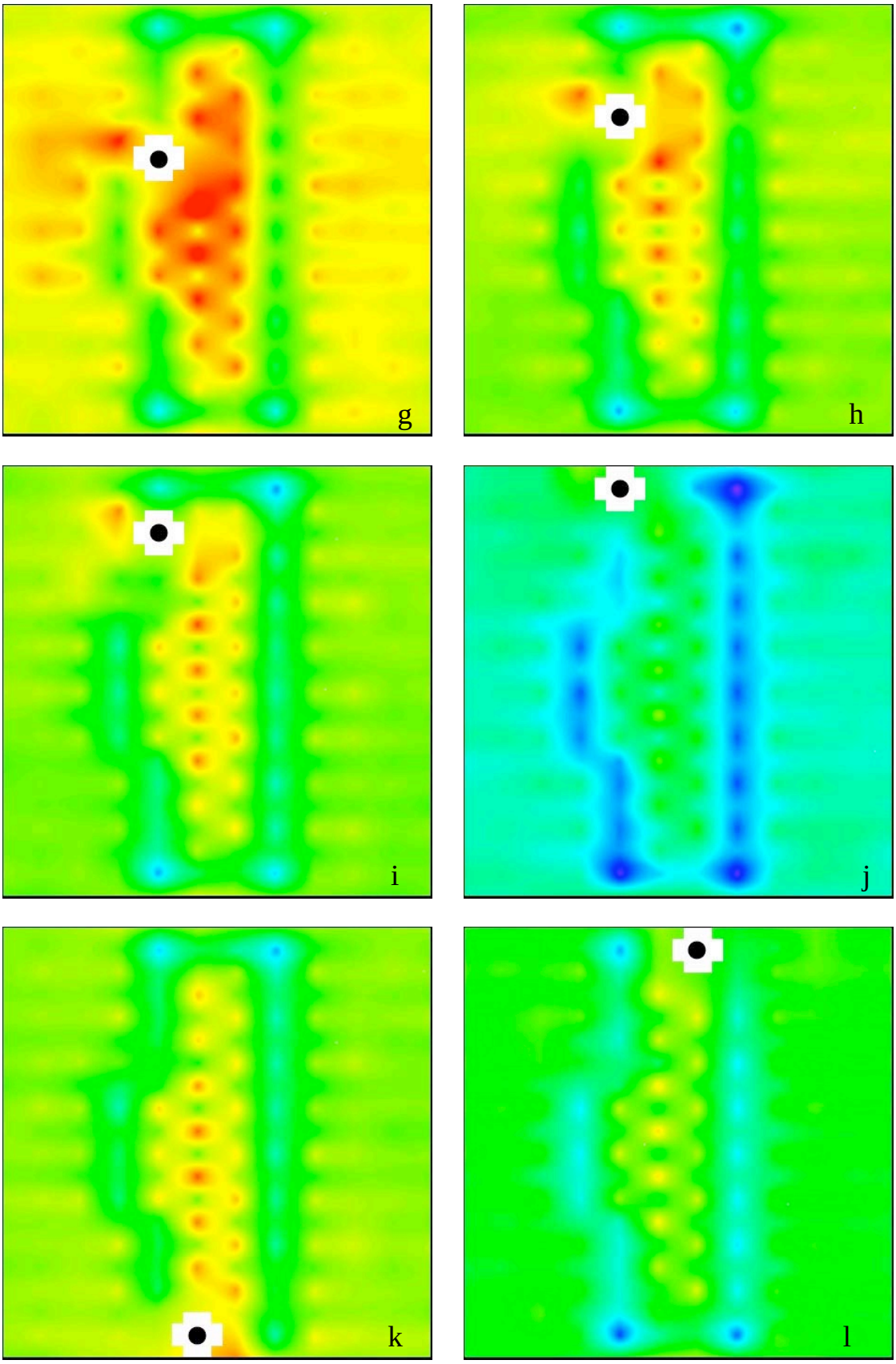
g
h
i
j
k
l

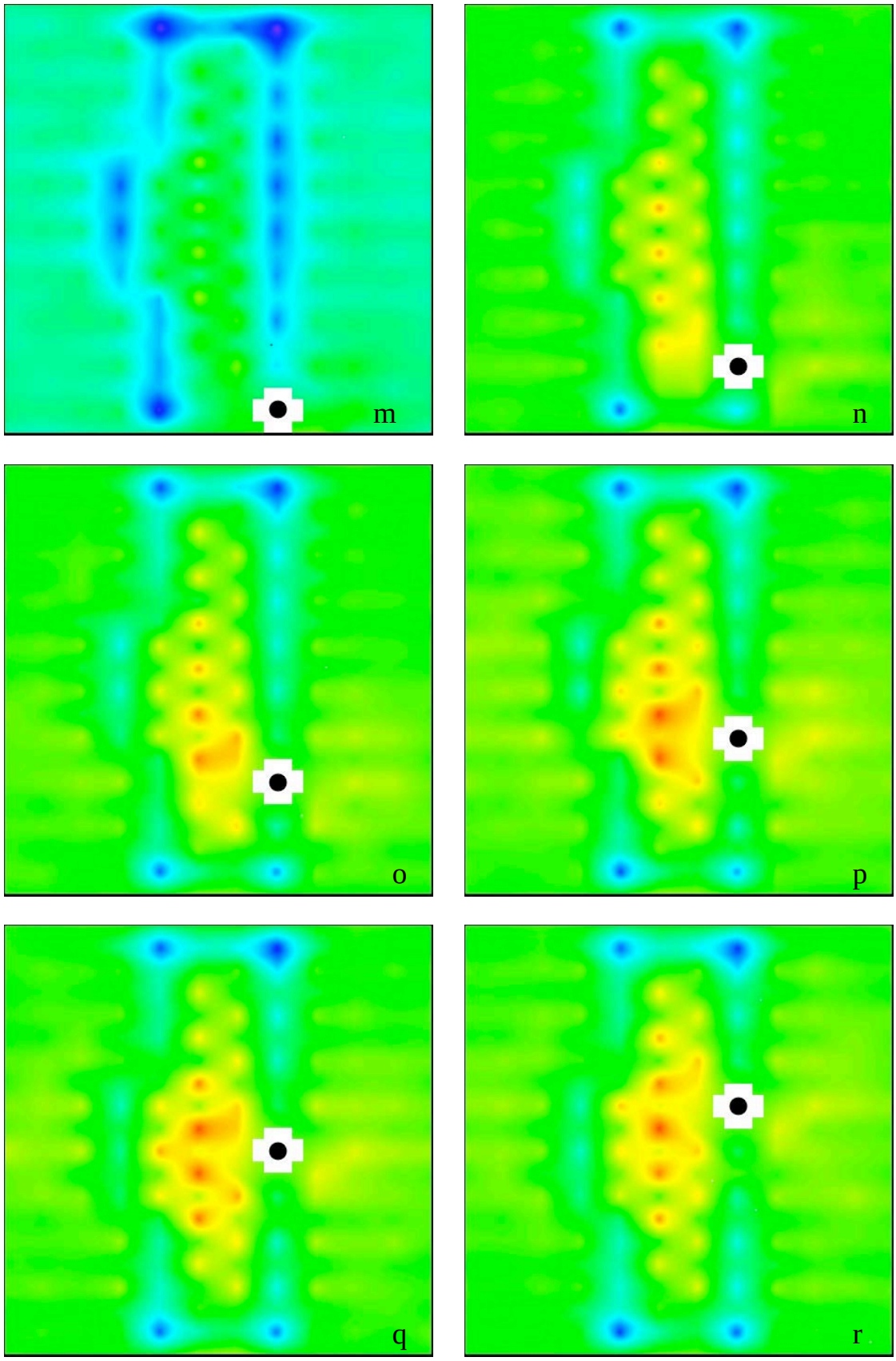
m
n
o
p
q
r

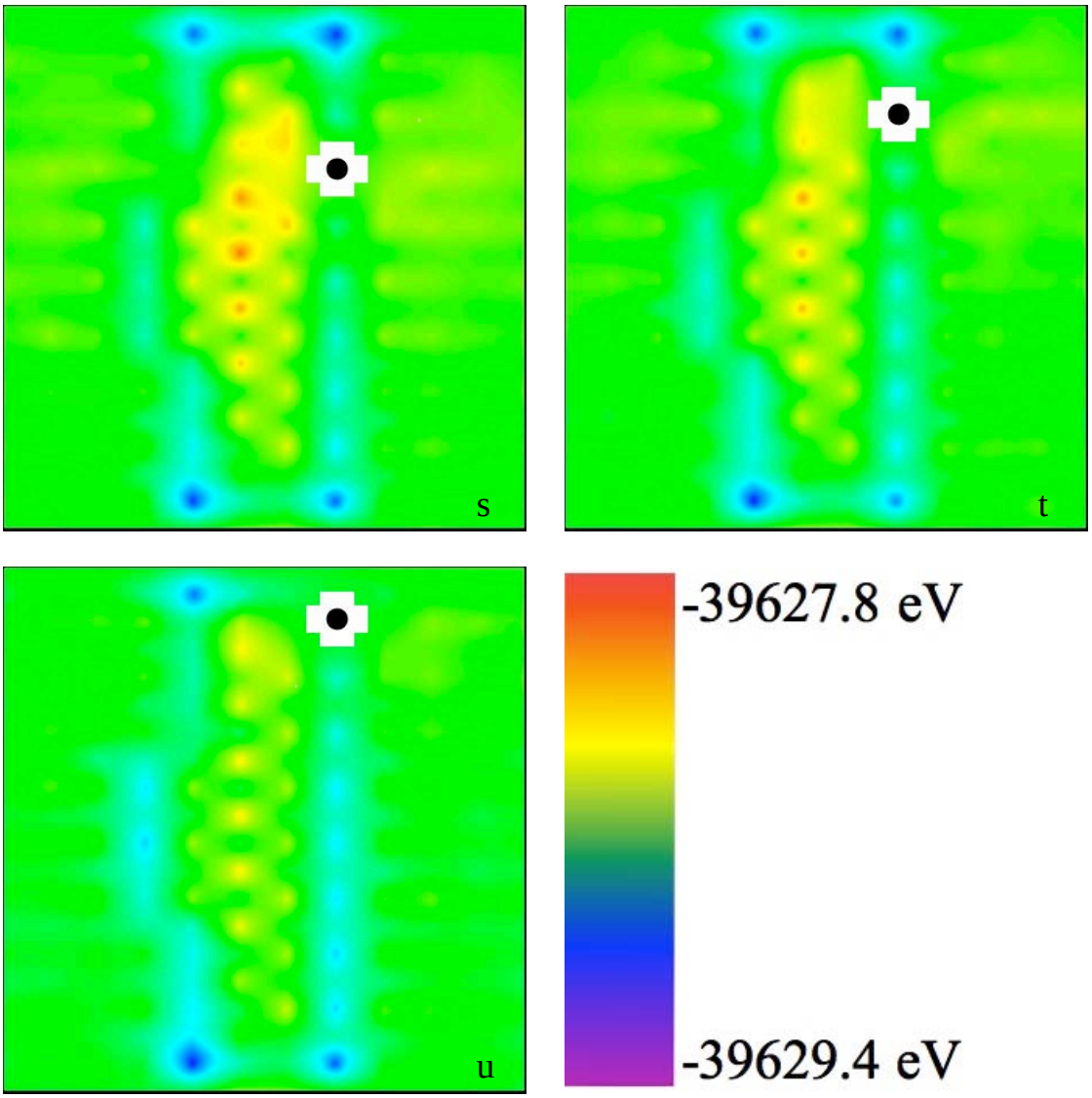

Figure 2.19.a-u: Results for the bump fractal system.

The results for the bump stripe configuration are presented in Figures 2.19.a-2.19.u. The results for the dented fractal configuration are shown in Figures 2.20.a-2.20.u. For both fractal data sets, the trends seem to remain the same with higher energy configurations inside the LTT stripe, and energy minima located at the interface. It is interesting to note that bump fractal when the polaron is pinned in a newly created "inside corner" (see Figure 2.19.g) the overall energy of the system is relatively higher.

In the dented fractal, the overall energy of the system appears to be higher when the stationary polaron is located on oxygen sites that are on the dent. It is also interesting to note that although these new input files have created new corner sites, these new corners do not exhibit as low minima as the four corners of the original stripe configuration. This would suggest that although the corners are lower energy sites, the four corners in the original stripe configuration could be giving energy values lower than would actually be expected. This could be attributed to the fact that there is only one row of atoms between one stripe and the next because of the periodicity of the system. In the future, it will be useful to check this by creating either a shorter stripe in which the repeating units would have the stripes further apart from each other. Another possibility to check this would be to generate a file in which the stripe extends the entire length of the simulation box, creating a sort of infinite stripe in the system, without corner sites.

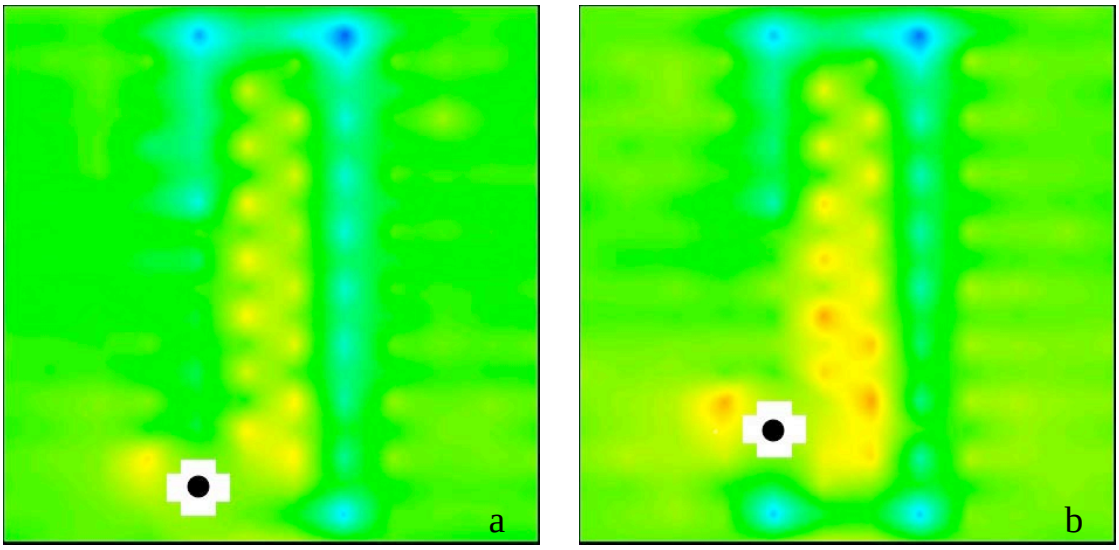

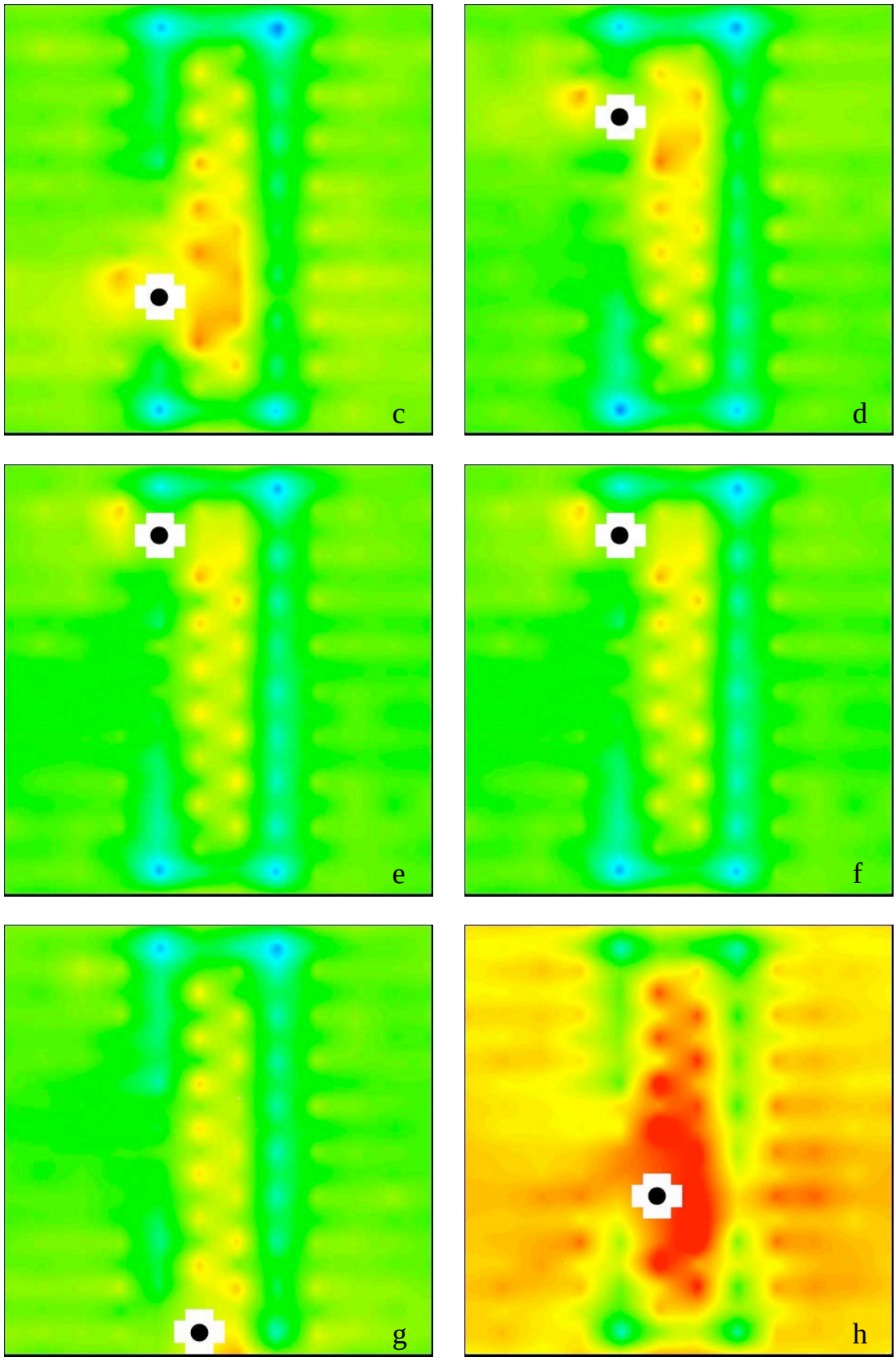
c
d
e
f
g
h

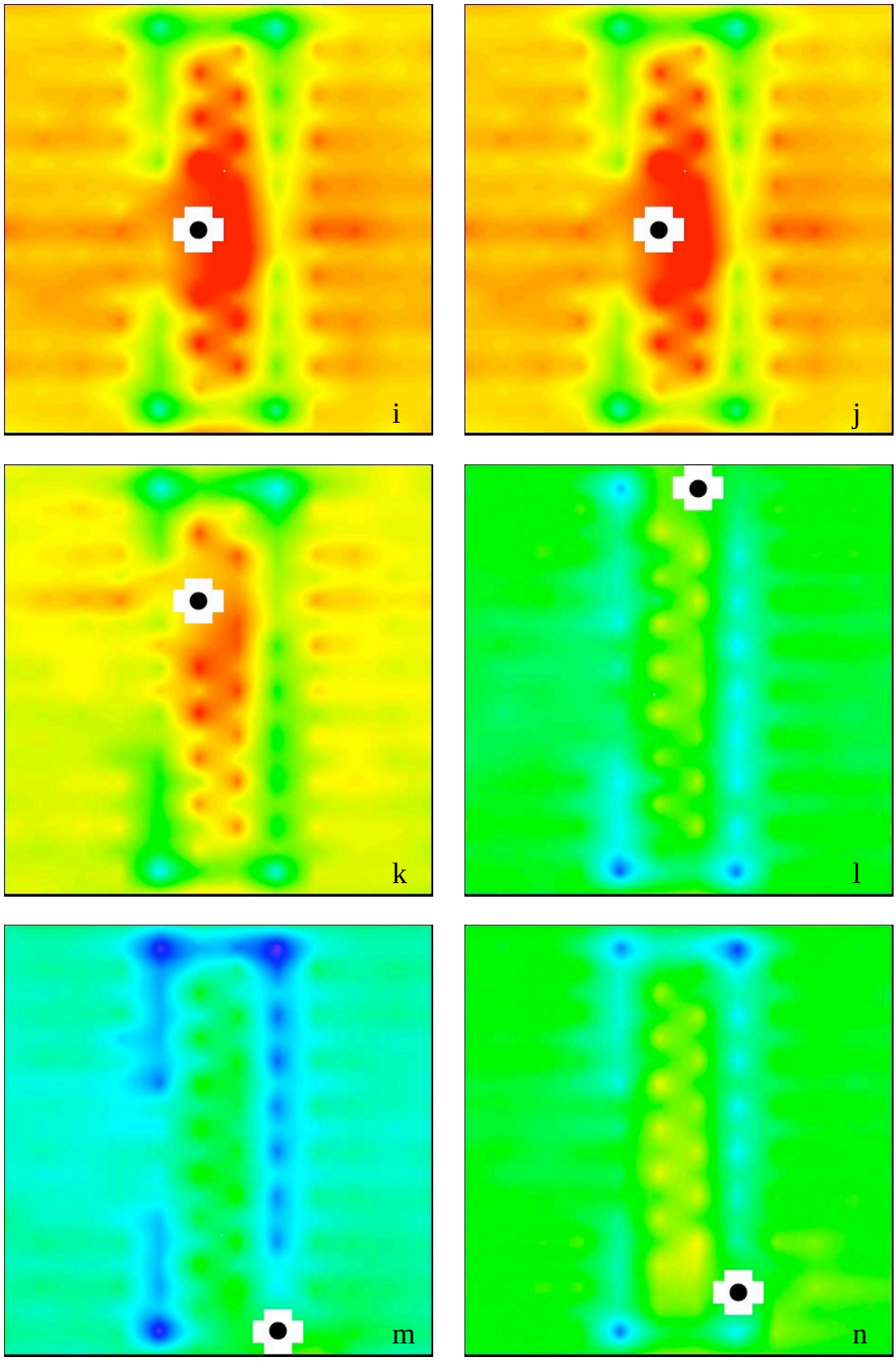
i
j
k
l
m
n

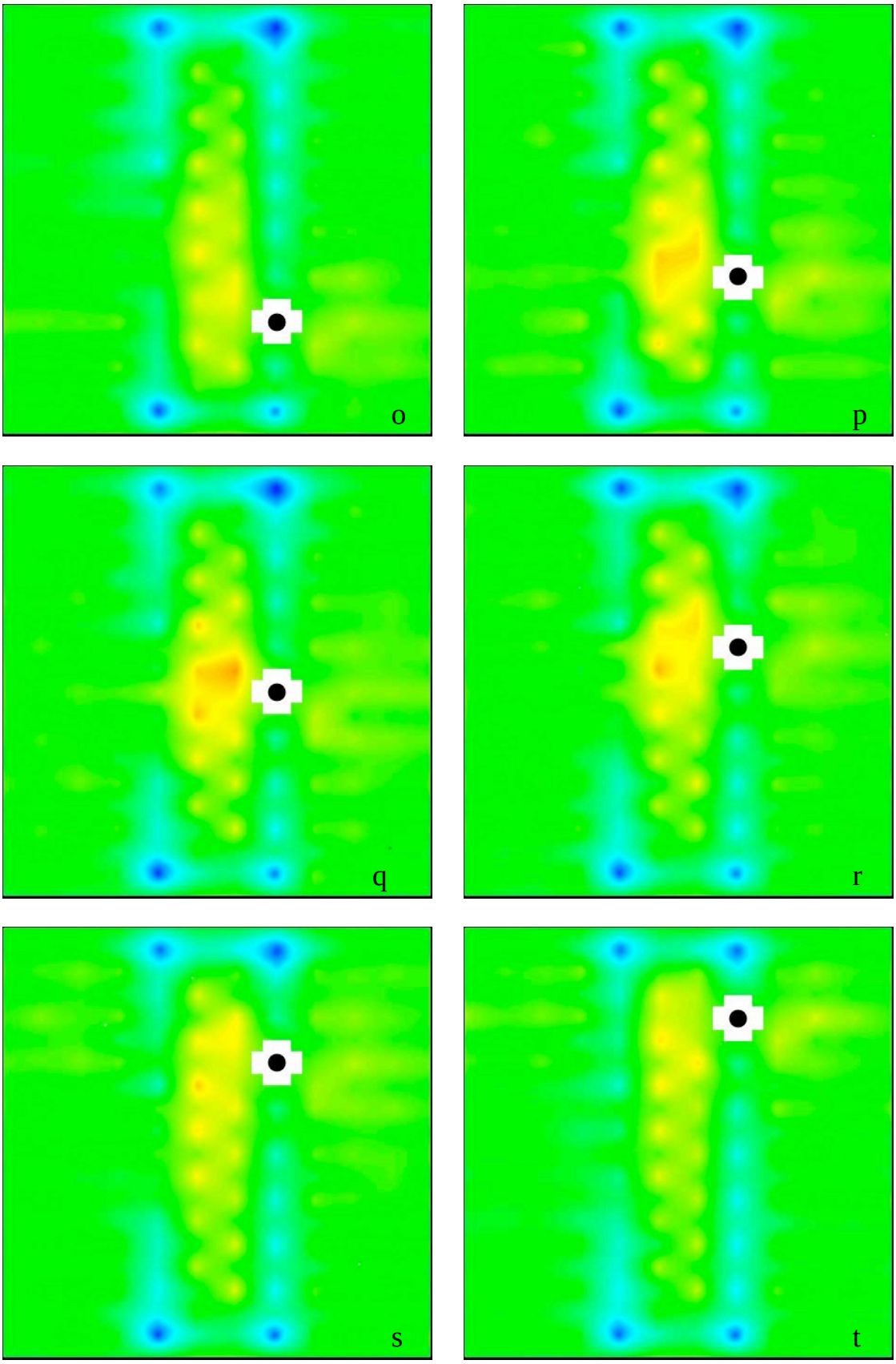
o
p
q
r
s
t

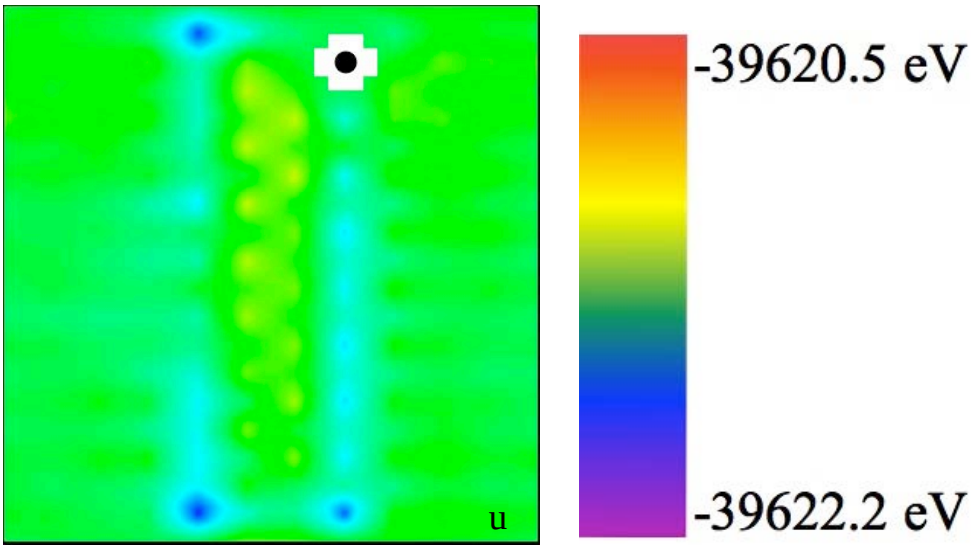

Figure 2.20.a-u: Results for the dent fractal system.

Given that we now have three different stripe configurations to consider, it would be useful to compare them to each other. In order to do this, the data was normalized to one baseline point in the LTO away from the LTT stripe. The configurations compared in Figure 2.21a-c comprise of one data set from each stripe variation, in which the stationary polaron is not pinned at a corner site, nor is it near the added feature in the newer configurations (the bump and the dent).

From this comparison it seems that the symmetrical stripe gives the lowest energy minima. There appears to be greater differences between the baseline and the energy maxima in the dent and bump configurations. Based on these plots, it would appear that the symmetrical stripe is the most energetically favorable configuration. In the future, it will be useful to do more comparisons such as this one to see if these results are consistent throughout all the data sets.

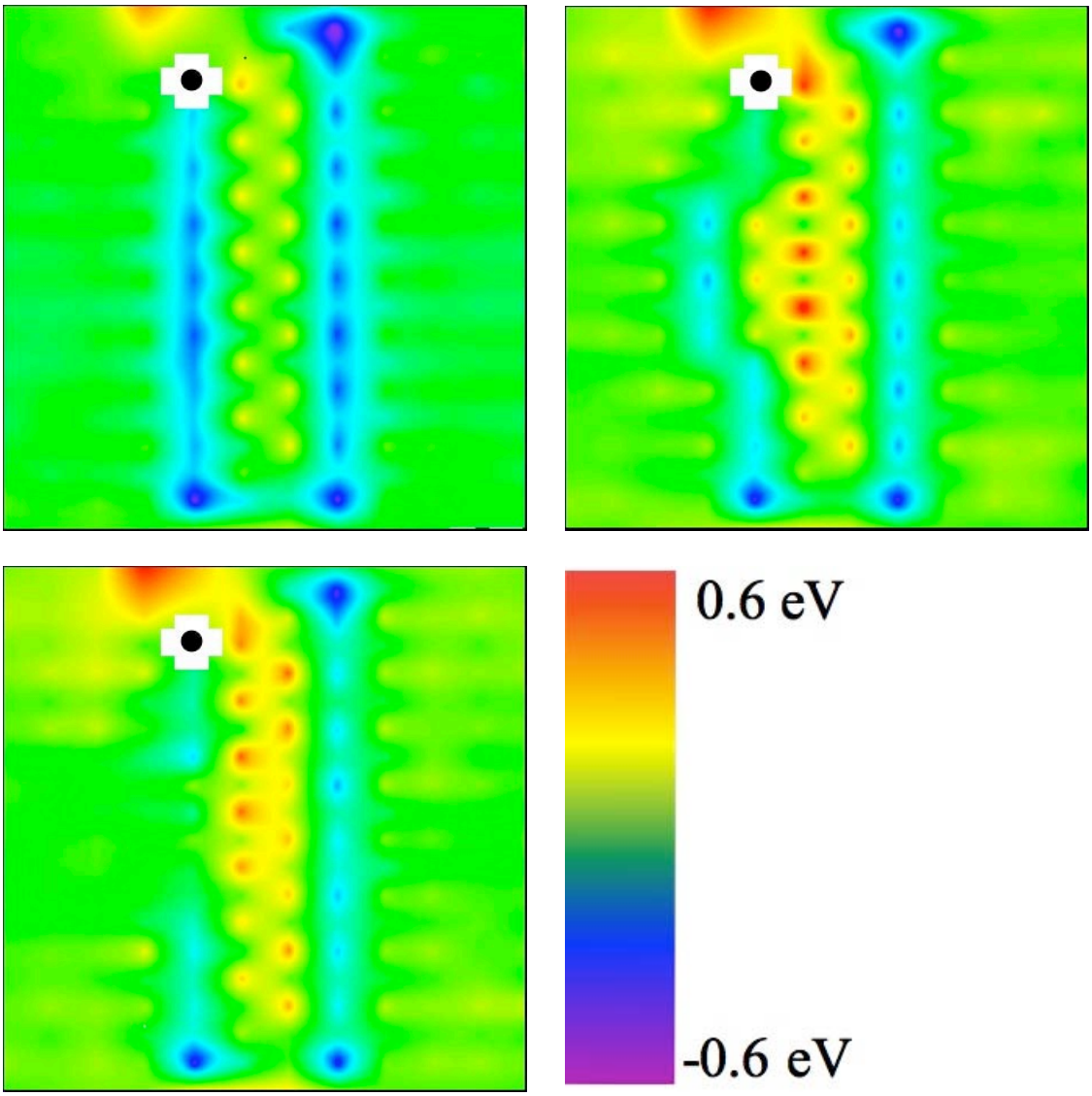

Figure 2.21a-c: Comparison of the normalized data for the three different stripe configurations. Figure (a) depicts the original symmetrical stripe; (b) shows the bump stripe and (c) shows the dented fractal.

2.4 Conclusions

We have developed a real space approach to simulating the effects of polarons in an LSCO-type lattice to help better understand their behavior in the superconducting cuprates. We have demonstrated a way to model these complex materials using the LTO-LTT simulation box, inserting polarons and examining their interactions as O^- species.

We have demonstrated that the polarons find energy minima at the LTT-LTO interfacial sites, with the corner sites exhibiting particularly low minima relative to the energy landscape. The polaron results in a higher energy configuration when placed inside the LTT stripe. We have also done pairing energy calculations showing pairing interactions even at longer distances, which could be attributed to strain propagation through the lattice. These data seem to be consistent with experimental results suggesting polaron organization in the stripe could be favorable, creating energy minima and allowing pairing interactions among polarons.

In the future it will be necessary to add in a magnetic component to this study, as it is an important aspect of these materials. This can be achieved through spin-based Feff calculations. This program will allow us to use the GULP output to generatre a spin-based calculation of the density of states for our relaxed lattice. We will be able to qualitatively compare DOS results from this program for stripe and pure LTO cases, thus observing the magnetic effects of the stripe addition to the LSCO-type lattice.

References

(1) Bednorz, J. G.; Muller, K. A. Z. Phys. B- Condensed Matter 1986, 64, 189.
(2) Bednorz, J. G.; Muller, K. A. Reviews of Modern Physics 1988, 60, 585.
(3) Bednorz, J. G.; Takashige, M.; Muller, K. A. Materials Research Bulletin 1987, 22, 819.
(4) Bednorz, J. G.; Takashige, M.; Muller, K. A. Europhysics Letters 1987, 3, 379.
(5) Leggett, A. J. Nature Physics 2006, 2, 134.
(6) Armitage, N. P.; Fournier, P.; Greene, R. L. Reviews of Modern Physics 2010, 82, 2421.
(7) Sokol, A.; Pines, D. Physical Review Letters 1993, 71, 2813.
(8) Tallon, J. L.; Buckley, R. G.; Haines, E. M.; Presland, M. R.; Mawdsley, A.; Flower, N. E.; Loram, J. Physica C 1991, 185-189, 855.
(9) Vershinin, M.; Misra, S.; Ono, S.; Abe, Y.; Ando, Y.; Yazdani, A. Science 2004, 303, 1995.
(10) Cooper, L. N. Physical Review 1956, 104, 1189.
(11) Kadin, A. M. Journal of Superconductivity and Novel Magnetism 2007, 20, 285.
(12) Anderson, P. W. Science 1987, 235, 1196.
(13) Li, L.; Wang, Y.; Komiya, S.; Ono, S.; Ando, Y.; Gu, G. D.; Ong, N. P. Physical Review B 2010, 81, 054510 99pp).
(14) Conradson, S. D.; Raistrick, I. D. Science 1989, 243, 1340.
(15) Saini, N. L.; Oyanagi, H.; Bianconi, A. Journal of Superconductivity 2004, 17, 103.
(16) Bussmann-Holder, A.; Keller, H. J. Supercond. Nov. Magn. 2009, 22, 123.
(17) Bussmann-Holder, A.; Keller, H.; Mustre de Leon, J.; Simon, A.; Bishop, A. R.; Muller, K. A. J. Supercond. Nov. Magn. 2010, 23, 295.
(18) Saini, N. L.; Oyanagi, H.; Wu, Z.; Bianconi, A. Superconductor Science and Technology 2002, 15, 439.
(19) Yavidov, B. Physica C 2010, 470, 85.
(20) Bussmann-Holder, A.; Muller, K. A.; Micnas, R.; Buttner, H.; Simon, A.; Bishop, A. R.; Egami, T. Journal of Physics: Condensed Matter 2001, 13, L169.
(21) Bussmann-Holder, A.; Keller, H.; Bishop, A. R.; Simon, A.; Muller, K. A. J Supercond Nov Magn 2008, 21, 353.
(22) Di Castro, C.; Grilli, M.; Caprara, S. Journal of Physics and Chemistry of Solids 2002, 63, 2219.
(23) Rubio Temprano, D.; Mesot, J.; Janssen, J.; Conder, K.; Furrer, A. Physical Review Letters 2000, 84, 1990.
(24) Lanzara, A.; Zhao, G.-m.; Saini, N. L.; Bianconi, A.; Conder, K.; Keller, H.; Muller, K. A. Journal of Physics: Condensed Matter 1999, 11, L541.
(25) Hashimoto, M.; He, R.-H.; Tanaka, K.; Testaud, J.-P.; Meevasana, W.; Moore, R. G.; Lu, D.; Yao, H.; Yoshida, Y.; Eisaki, H.; Devereaux, T. P.; Hussain, Z.; Shen, Z.-X. Nature Physics 2010, 6, 414.

(26) Kordyuk, A. A.; Zabolotnyy, V. B.; Evtushinsky, D. V.; Buchner, B.; Borisenko, S. V. Journal of Electron Spectroscopy and Related Phenomena 2010, 181, 44.
(27) Bianconi, A.; Saini, N. L. Structure and Bonding 2005, 114, 287.
(28) Bianconi, A.; Saini, N. L.; Lanzara, A.; Missori, M.; Rossetti, T.; Oyanagi, H.; Yamaguchi, H.; Oka, K.; Ito, T. Physical Review Letters 1996, 76, 3412.
(29) Bianconi, A.; Bianconi, G.; Caprara, S.; Di Castro, D.; Oyanagi, H.; Saini, N. L. Journal of Physics: Condensed Matter 2000, 12, 10655.
(30) Tranquada, J. M.; Sternlieb, B. J.; Axe, J. D.; Nakamura, Y.; Uchida, S. Nature 1995, 375, 561.
(31) Daou, R.; Chang, J.; LeBoeuf, D.; Cyr-Choiniere, O.; Laliberte, F.; Doiron-Leyraud, N.; Ramshaw, B. J.; Liang, R.; Bonn, D. A.; Hardy, W. N.; Taillefer, L. Nature 2010, 463, 519.
(32) Hanaguri, T.; Kohsaka, Y.; Davis, J. C.; Lupien, C.; Yamada, I.; Azuma, M.; Takano, M.; Ohishi, K.; Ono, M.; Takagi, H. Nature Physics 2007, 3, 865.
(33) Kristoffel, N.; Rubin, P. Solid State Communications 2002, 122, 265.
(34) Gomes, K. K.; Pasupathy, A. N.; Pushp, A.; Ono, S.; Ando, Y.; Yazdani, A. Nature 2007, 447, 569.
(35) Timusk, T.; Statt, B. Reports on Progress in Physics 1999, 62, 61.
(36) Ovchinnikov, A. A.; Ovchinnikova, M. Y. Physics Letters A 1998, 249, 531.
(37) Vojta, M. Advances in Physics 2009, 58, 699.
(38) Hackl, A.; Vojta, M. New Journal of Physics 2010, 12, 105011(17pp).
(39) Kivelson, S. A.; Bindloss, I. P.; Fradkin, E.; Oganesyan, V.; Tranquada, J. M.; Kapitulnik, A.; Howald, C. Reviews of Modern Physics 2003, 75, 1201.
(40) Parker, C. V.; Aynajian, P.; Neto, E. H. d.; Pushp, A.; Ono, S.; Wen, J.; Xu, Z.; Gu, G.; Yazdani, A. Nature 2010, 468, 677.
(41) Robertson, J. A.; Kivelson, S. A.; Fradkin, E.; Fang, A. C.; Kapitulnik, A. Physical Review B 2006, 74, 134507 (10pp).
(42) Catlow, C. R. A.; Tomlinson, S. M.; Islam, M. S.; Leslie, M. Journal of Physics C: Solid State Physics 1988, 21, L1085.
(43) Gale, J. D.; Rohl, A. L. Molecular Simulation 2003, 269, 291.
(44) Fratini, M.; Poccia, N.; Ricci, A.; Campi, G.; Burghammer, M.; Aeppli, G.; Bianconi, A. Nature 2010, 466, 841.
(45) Poccia, N.; Ricci, A.; Bianconi, A. Journal of Superconductivity and Novel Magnetism 2011, 24, 1195.

Chapter 3: Local structure of Ni-doped Mg nanoparticles via x-ray absorption fine structure (XAFS) spectroscopy and neutron scattering[iii]

3.1 Introduction

One of the primary challenges to the progress of the hydrogen economy is the development of a reliable and cost-effective form of storage for this innovative fuel source.[1,2] Current storage methods, which involve containing it as a gas in a pressurized cylinder or as a liquid in a cryogenic tank, face limitations in their applicability as an on-board fuel source in the transportation industry due to low energy density, complex equipment, and potential safety risks.[3] Much effort has been placed on developing new hydrogen storage systems that utilize the ability of certain metals and alloys to reversibly absorb hydrogen, many of which have shown much higher storage capacities than classic hydrogen storage methods. This solid-state approach to hydrogen storage shows great potential as a safe, volume-efficient solution for vehicle applications in the developing hydrogen economy.[3-7] However, for this method to be useful the material will have to sorb and desorb H_2 over a wide range of pressures, rates, and temperatures, without having to resort to a significant temperature differential or other energy input to reverse the process.

[iii] Samples for experiments were prepared by Nick S. Norberg and Timothy S. Arthur. XAFS experiments were performed at the Stanford Synchrotron Radiation Lightsource (SSRL) by Steven D. Conradson. Neutron scattering data were measured by Thomas Proffen at the Lujan Neutron Scattering Center at Los Alamos National Laboratory. All data were analyzed by Alison L. Costello, Francisco Javier Espinosa-Faller, Dylan R. Conradson and Mary B. Martucci.

One of the most promising candidates in this class of materials is magnesium and its alloys with certain metals. These materials with their corresponding hydrides have been studied as possible hydrogen storage systems.[8-11] Magnesium possesses many advantages over other comparable systems in that it is earth abundant, non-toxic, and it exhibits relatively high volumetric capacity (1.4 kg H_2/L) and gravimetric capacity (7.6 mass % H_2).[7,8,12] However, a major drawback in the application of this material for vehicular on-board fuel storage is the slow reaction kinetics involved in hydriding and dehydriding the bulk metal, requiring on the order of hours to complete a full hydrogenation cycle for the bulk material.[13,14] The diffusion rate of hydrogen through magnesium in this gas-solid reaction is a limiting factor for the kinetics.[15,16] Also, during the hydrogenation of magnesium, as the hydrogen diffuses it creates a hydride layer which inhibits subsequent hydrogen diffusion into the bulk material. As the hydrogenation process proceeds, diffusion through this hydride layer becomes the rate-limiting step.[17]

There have been two major advances that have vastly improved upon the slow kinetics. The first is the ball milling of bulk magnesium to create micro- and nanostructures, which results in shortened diffusion paths to the center of the material and also increases the surface area upon which the gas-solid reaction can initiate resulting in significantly improved cycling rates.[18-24] Moreover, ball milling creates numerous defects on the surface within the material. These resulting lattice defects aid in the diffusion of hydrogen by creating numerous sites with low activation energy of diffusion.[25,26] As a result, cycling time improves from hours to minutes.[27]

The second focus in current research for advancing the kinetic performance in the hydrogen cycling is through the employment of transition metals or metal oxides as catalytic additives. For example, Liang and coworkers examined the effects of Ti, V, Mn, Fe, and Ni on the hydrogen storage properties of mechanically milled magnesium, demonstrating that various transition metal catalysts could be used to enhance kinetics.[28] There are numerous other examples in the literature of the kinetics improvements resulting from these catalytic additions.[29-35] In addition to these, metal oxides have been extensively investigated as catalysts for hydrogen storage in the last decade.[36-44] Oelerich et al. have investigated the catalytic effects of a wide range of metal oxides milled with magnesium including Cr_2O_3, Fe_3O_4, CuO, V_2O_5, Al_2O_3, SiO_2, TiO_2, and Sc_2O_3, demonstrating that most of these oxides facilitate similar improvements to absorption rates and that iron oxide yields the fastest desorption kinetics.[45-47] Barkhordarian and coworkers studied the effects of Nb_2O_5 content as a catalytic additive to nanocrystalline magnesium. They found that the activation energy for the hydrogenation reaction decreased exponentially with increasing Nb_2O_5 additions.[48]

A key ingredient to the continued progress of this research will be to elucidate the microscopic mechanism and reversibility of the hydrogenation and dehydrogenation, which will afford a greater understanding of the of the tunability of the material and, in turn, the reaction. In this respect, the ball milled magnesium-catalyst materials are unfavorable because the process results in copious defects and inhomogeneous products, making it difficult to pinpoint optimal hydrogenation conditions.[19,38,41,49] Ares et al. reported on damaging effects to hydrogen absorption on account of contamination from ball milling tools.[50] In addition to this, although the aforementioned oxide catalysts result

in faster kinetics, the drawback to this development is that the mass of these dopants diminishes the mass of Mg available for hydrogen storage. Our group has developed a solution-phase synthesis of magnesium nanoparticles doped *in situ* with 5 wt.% nickel.[51] It will be possible to garner much more structural and mechanistic information about this system using this synthesis, as opposed to high-energy ball milling, as this method yields homogeneous particles with a narrower size distribution with more uniform and homogeneous dispersal of the catalyst. Moreover, the use of nickel as the catalyst could prove to prevent the attenuation of the effective mass upon catalyst addition, as Mg-Ni alloys are known hydrogen storage materials. There are multiple known Mg-Ni alloys, which are known hydrogen storage materials, including Mg_2Ni and $MgNi_2$.

This new synthesis has enabled the determination of the local, atomic scale, element specific structure of Ni-doped magnesium nanoparticles through the hydrogen cycling process using neutron scattering and x-ray absorption fine structure (XAFS) spectroscopy. Previously, Topler et al studied the bulk phases for the Mg and the Mg-Mg_2Ni systems using quasi-elastic neutron scattering. They determined that the faster kinetics observed in the Mg-Mg_2Ni system are likely influenced by surface effects, as they observed that hydrogen diffusion occurs more slowly through Mg_2Ni than through the pure magnesium phase.[15] To our knowledge, local structure information on nanocrystalline magnesium during the hydrogen cycling process is limited, due the extremely disordered nature of the products that result from ball milling the bulk material. The two structure characterization methods utilized, neutron scattering and Ni K edge XAFS, are highly complementary. At the 2 atomic-% level of the Ni, the neutrons are sensitive to the majority Mg because the Ni contributes its population-

weight multiplied by its scattering length and produces only around 4 % of the total scattering so that the scattering and resulting pair distribution function (pdf) are essentially monopolized by the Mg (Mg scattering cross section=3.71, Ni scattering cross section=18.5). Ordered materials will give diffraction patterns and species with only local order give signals in the pair distribution function. The element selectivity of XAFS spectroscopy renders it sensitive only to the local structure of the minority Ni fraction whatever degree of order it possesses. This pair of experiments should therefore be able to provide a relatively complete description of the structural chemistry of the Mg(Ni) nanoparticles with respect to hydrogen cycling. Using these techniques, we show that dramatic changes occur between the hydrogenation to the dehydrogenation steps. Studying these changes that occur during the hydriding and dehydriding process, which are unobservable in bulk diffraction analysis, using these alternative methods that are sensitive to the aperiodic components of the structure, including the Ni constituent, enable insights into the hydrogenation/dehydrogenation mechanisms that should allow tuning of the material in the future to maximize hydrogen cycling efficiency.

3.2 Experimental

Sample Preparation- Magnesium nanopowder samples doped with various wt.% nickel samples were synthesized, characterized and hydrogenated/dehydrogenated following the synthesis procedure presented in reference (41). Three separate samples were prepared for the XAFS measurements, putatively via the same procedure. A separate sample was prepared for the neutron scattering.

XAS and Neutron Diffraction Sample Preparation- All synthesized material was handled under a nitrogen atmosphere in a glovebox to prevent oxidation of the magnesium. Two samples were prepared for neutron scattering analysis: the first was the prepared 5 wt.% Ni-doped magnesium that had undergone deuterium cycling; the second was the prepared Ni-doped magnesium that had been cycled once and then re-deuterated. The two samples were loaded into vanadium cans and sealed with indium wire. Neutron scattering data was collected at Lujan Neutron Scattering Center at Los Alamos National Laboratory at Flight Path 1- Neutron Powder Diffractometer (NPDF).

Three samples were prepared for x-ray absorption measurements: the first was 1 wt.% Ni-doped Mg (sample 125); the second was 5 wt.% Ni-doped Mg (sample 127); and the third was 10 wt.% Ni-doped Mg (sample 151). All three samples were hydrogen-cycled once prior to analysis. Then, half of each sample was then separated out and hydrogenated again, to create three additional hydrided samples for analysis: 125h, 127h and 151h, respectively. X-ray absorption spectroscopy (XAS) samples were run at the Stanford Synchrotron Radiation Lightsource (SSRL), a directorate of the SLAC National Accelerator Laboratory at Stanford University.

Neutron scattering fits were performed using pdfGUI.[52] Fits were done by the inclusion of various structures of Ni to determine how the Ni was incorporated into the nanoparticles. X-ray measurements were performed and the data analyzed by standard procedures.[53]

3.3 Results and Discussion

Neutron scattering results- Mg(Ni). The neutron scattering data on the cycled metallic nanoparticles display a relatively weak diffraction pattern and what appear to be several very broad peaks and other structure in the baseline slightly above or at the noise level. These results are presented in Figure 3.1. The diffraction pattern exhibits the peaks for and refines to the structure of hexagonal magnesium metal, with lattice constants of a=b=3.2058 Å and c=5.2037 Å, compared to the reported values of a=b=3.2094 and c=5.2108 Å. It would be expected to see an increase in the cell volume, as the incorporation of the relatively larger nickel atoms would expand the lattice.

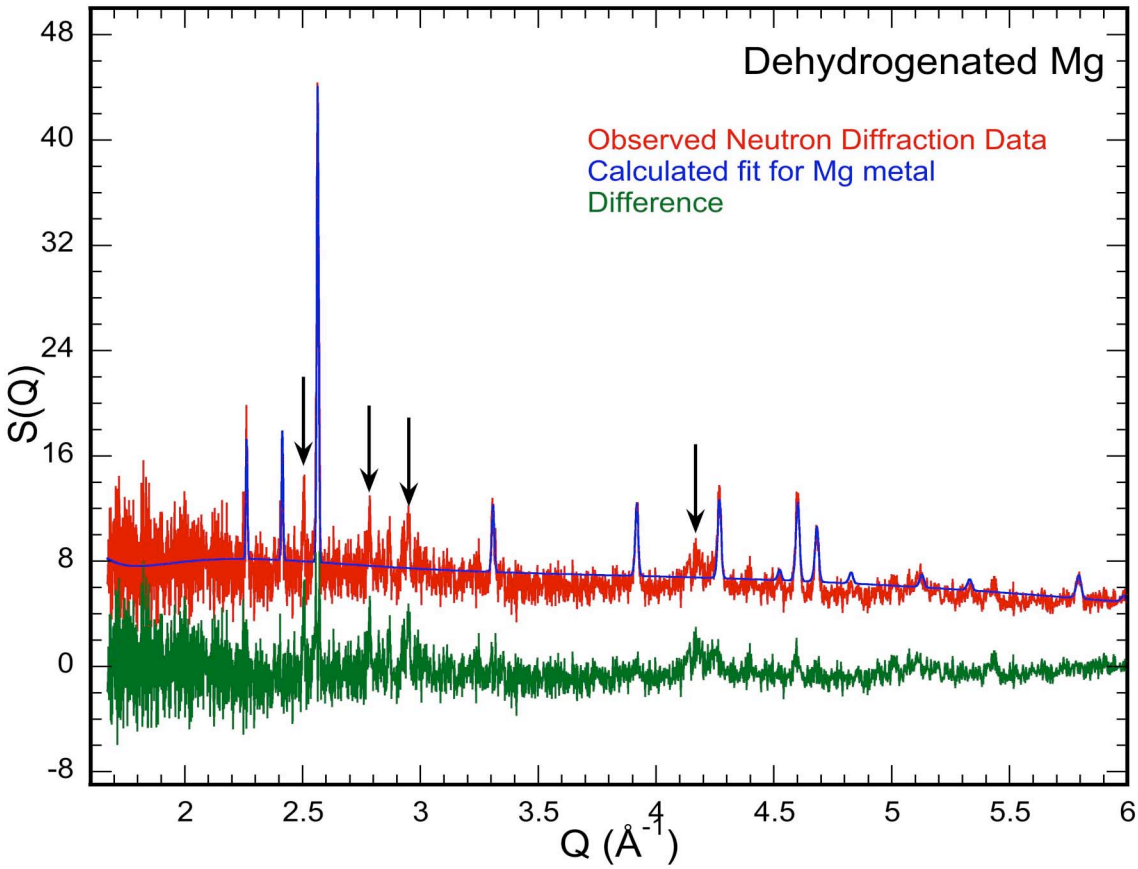

Figure 3-1: Neutron diffraction pattern modeled with a metallic Mg phase. Arrows indicate additional peaks, which do not index to Mg, Ni, an Mg-Ni alloy, or the vanadium can, suggesting a disordered Mg-Ni phase.

The approximately 1 ppt contraction is most likely due to the low temperature of the samples for the neutron measurements and therefore not significant. The peaks are not well fit, exhibiting diffuse scattering in the form of substantially broadened bases. Particle size effects may be the cause of this, but the most likely source is substantial disorder in the structures induced by the added Ni. The positions of the other peaks, although somewhat uncertain because of their width, do not correspond to Ni (fcc, a=3.524 Å) or Mg_2Ni (hexagonal, a=b=5.216 Å). They therefore most likely indicate the non-Mg fraction of the particle is a disordered or at least an aperodic Mg-Ni compound, which can be further tested by examination of the pair distribution function plots pdfs-g(r).

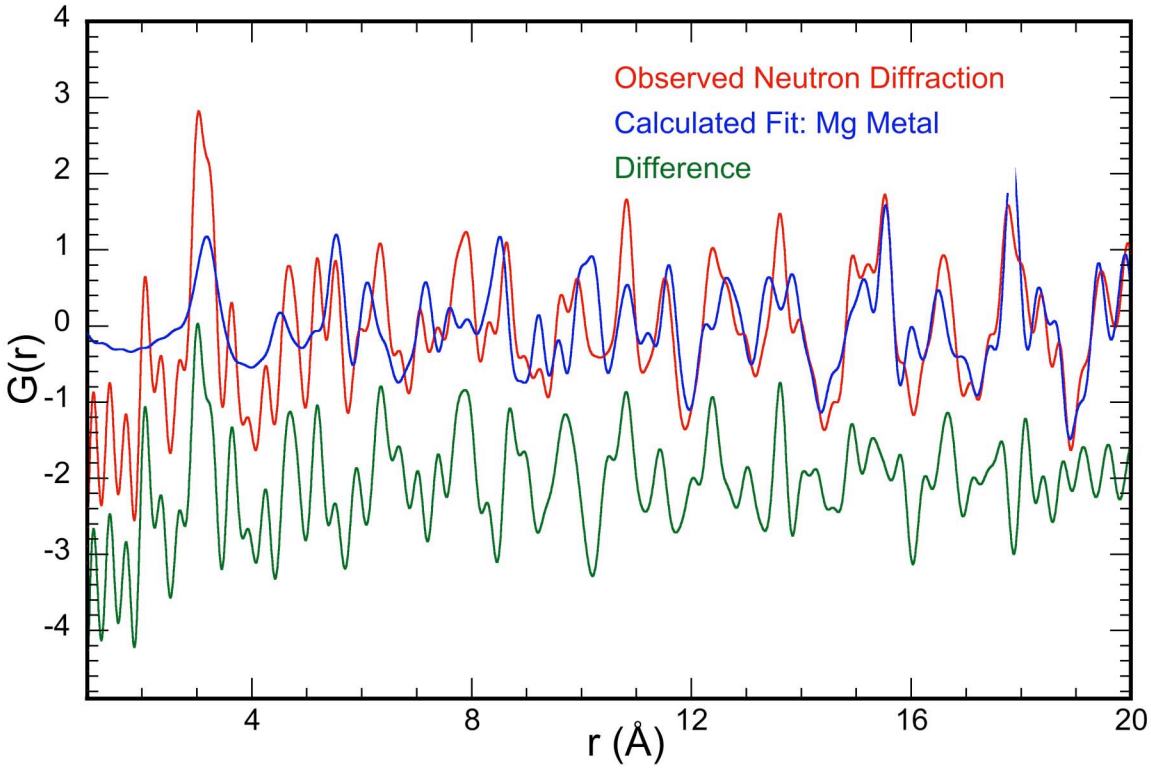

Figure 3-2: Pair distribution function fit with metallic Mg. Red line is the calculated data, blue shows the experimental data and green identifies the differences in the two spectra.

This is evident in the pair distribution function generated by taking the Fourier transform of the F(Q) function of the structure factor. The calculated Mg g(r), shown in

Figure 3-2, displays many of the same peaks that occur in the experimental data out through 20 Å, with only a few extraneous Mg pairs that would indicate the presence of compounds in addition to pure Mg metal. The diffraction pattern, however, demonstrates that bulk Mg occurs, so it is unclear why not all of the Mg peaks are found. Mg by itself, however, only accounts for around half of the peaks in the data, with an extra one apparent even in the nearest neighbor shell at a slightly lower distance than the Mg-Mg peak with which it overlaps. The attempt was made to fit these additional peaks with various possible compounds, including MgD_2 (Figure 3-3), Mg_2Ni (Figure 3-4a), and Ni (Figure 3-4b).

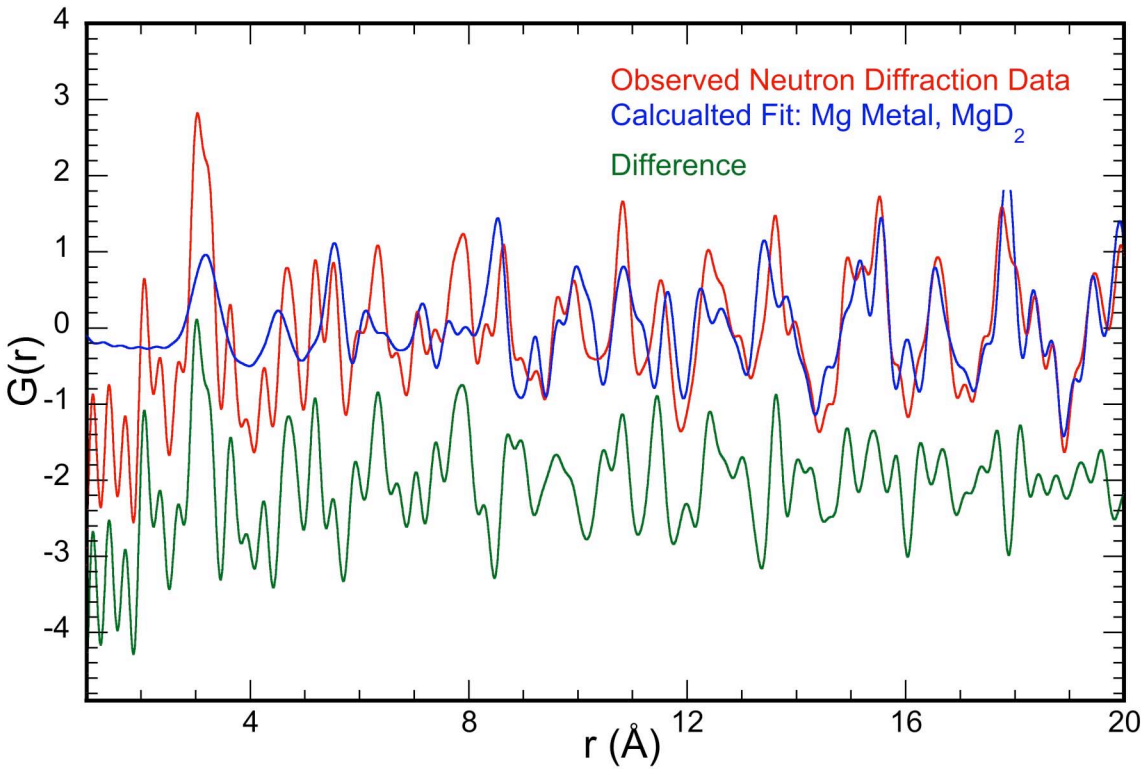

Figure 3-3: Pair distribution function modeled with Mg and MgD_2 phases. Red indicates the raw data, blue the calculated fit and green shows the difference between these two. Note that the fit is not improved with the addition of the MgD_2 to the Mg metal fit.

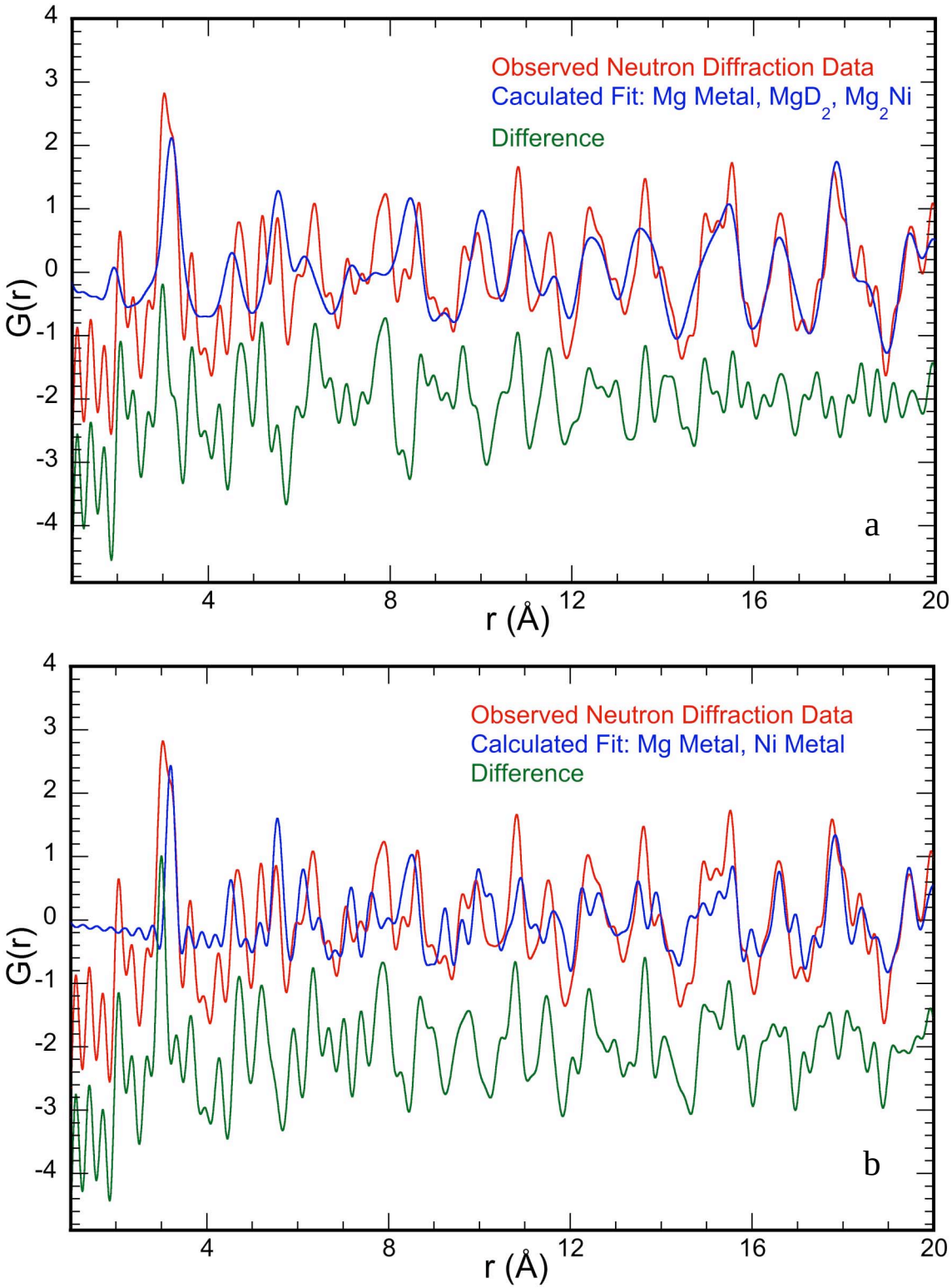

Figure 3-4: (a) Pair distribution function modeled with Mg, MGD_2, Mg_2Ni phases. (b) Pair distribution function fit with Mg, MgD_2, and Ni phases. Note that in both cases, the fit is not improved with the addition of another phase.

Adding the MgD_2 g(r) does not give a better fit. In the refinement its amplitude becomes very low because its structure contains very few of the non-Mg peaks in the data. Mg_2Ni does appear to share more of the non-Mg peaks with the data – although not the nearest neighbor one, but does not decrease the overall error more than the hydride. Having some of the same pairs bolsters the idea that the non-Mg fraction is a Mg-Ni mixture of some type that is definitely not the ordered alloy. Fitting with the addition of the nickel metal phase was also attempted (Figure 3-4b). Again no major improvement is seen in the fit with this added phase, which further supports the idea of a disordered or aperiodic Mg-Ni product after hydrogen cycling.

Table 3-1: Summary of neutron scattering pdf fitting results for the Mg sample.

Phase	χ^2	Mg Metal Scaling Factor	Mg_2Ni Scaling Factor	Ni Scaling Factor	MgD_2 Scaling Factor
Mg	929.961	0.197			
Mg, MgD_2	962.811	0.205			0.124
Mg, MgD_2, Mg_2Ni	769.387	0.303	-0.024		0.081
Mg_2Ni	1399.45		0.333		
Mg, MgD_2, Mg_2Ni	794.232	0.275	-0.249		0.003
Mg, Ni	991.804	2.847		-0.001	

Fits of the cycled Ni-doped Mg showed no contribution from deuterium structures to the structure suggesting that the samples were successfully dehydrogenated. The sample was predominantly Mg metal structure and inclusion of Mg_2Ni and Ni metal structures both returned negative phase contributions (see Table 3.1), indicating that these structures do not contribute to the ordering in the synthesized sample. Substituting Ni into the Mg fits likewise failed to give a positive phase contribution, which suggests that these phases are not contributing to the ordering in the structure. Because of the poor

quality of the fits and the lack of order in general within the material, it was not possible to generate reliable information on the strain or particle size for this sample.

Ni XAFS results- Mg(Ni). The Ni XAFS of these metallic nanoparticles support this interpretation. Relative to the XANES of Ni metal (shown in Figure 3-5), the energies of the leading edge are only a few eV higher, consistent with the low valence of a metal. The spectra are broad and featureless, consistent with a highly disordered local environment. There are some small differences, the spectrum of the 125 sample is slightly higher in energy and has somewhat lower intensity for a possible feature at 8348 eV that makes it more concave in that region.

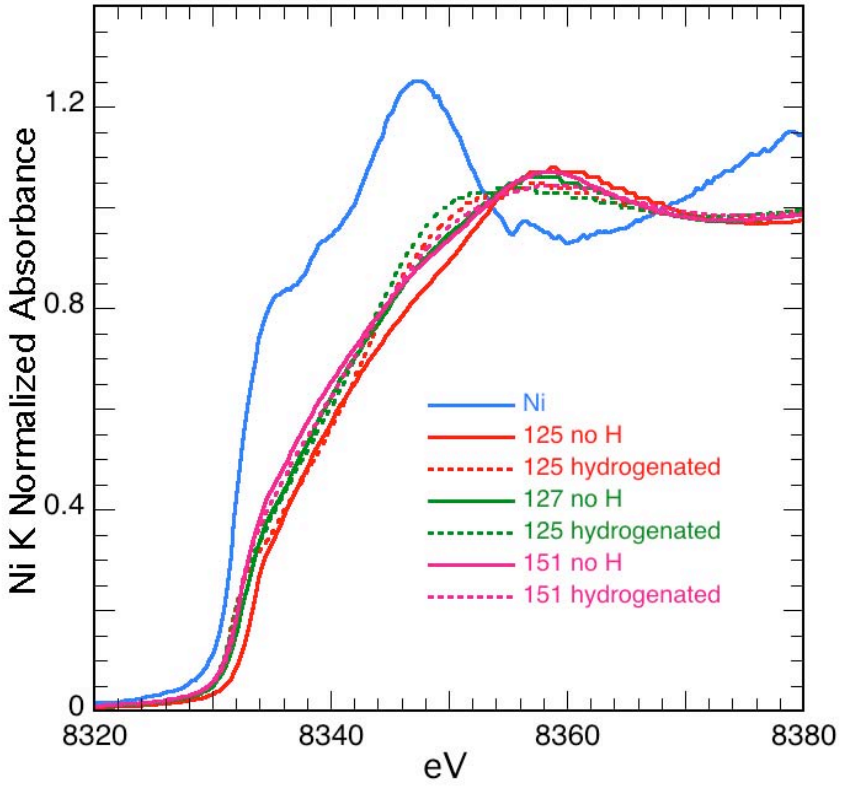

Figure 3-5: Ni edge XANES for all samples. Blue line shows the nickel standard as a comparison. Note the difference in energy values between the Ni standard and the set of synthesized samples, suggesting a highly disordered structure.

The three EXAFS spectra, presented in Figure 3-6, exhibit similar patterns in the real component for the primary nearest neighbor contribution that is the peak at R=2.26–

2.29 Å, that occurs at a significantly higher position than the R=2.15 Å value in Ni metal. The real component is asymmetric and higher just past the modulus peak. Again this differs from the spectrum of Ni that is asymmetric but with its higher feature on the low R side of its modulus peak. This spectral feature therefore cannot be composed solely of contributions from Ni neighbors but must also include Mg. The amplitudes of this peak are also similar, around 0.35–0.45. This must, however, be compared with this amplitude in the spectrum of Ni metal, which is close to 6. The presence of nearest neighbor Mg with its lower backscattering amplitude relative to Ni explains some of this reduction, but not all.

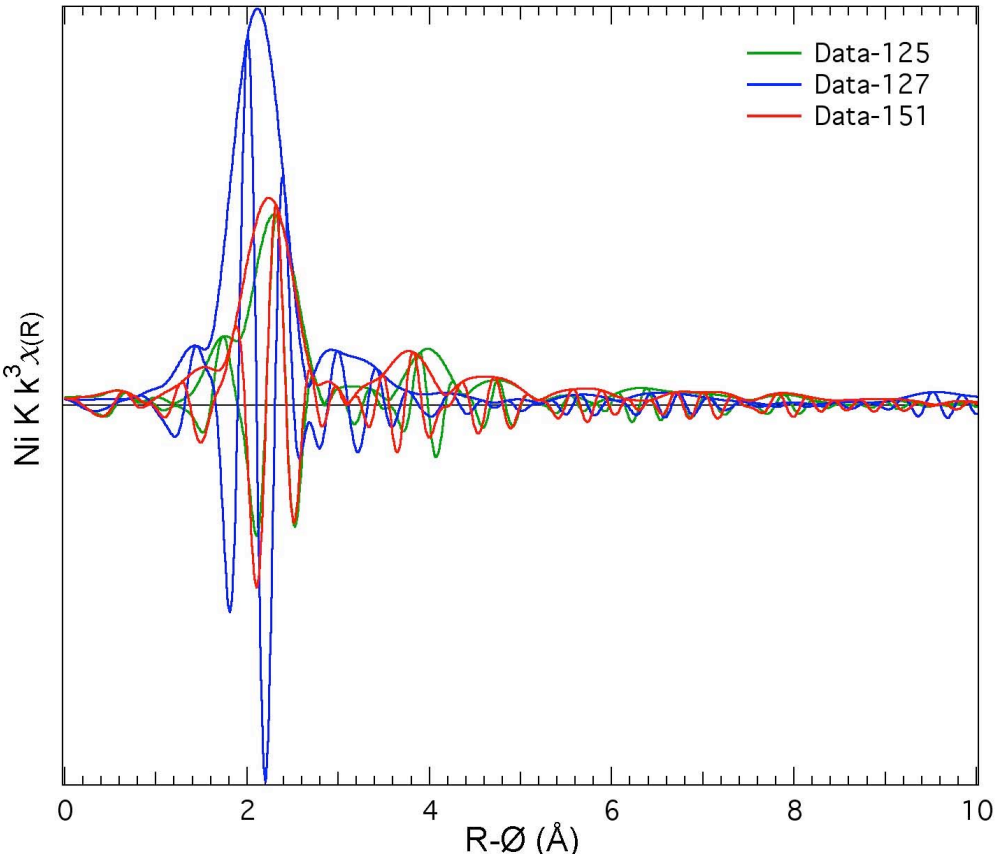

Figure 3-6: Ni EXAFS (χ(R) representation) of the indicated samples.

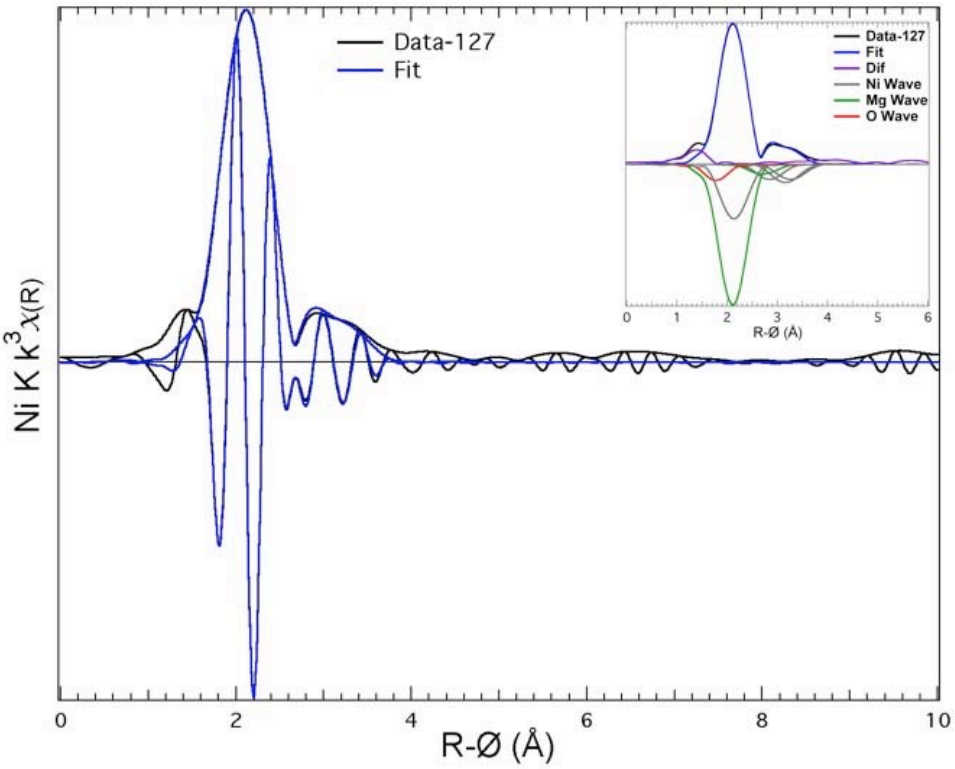

Figure 3-7: EXAFS data and fit for sample 127 showing the fitted data. The inset shows the difference in the data and fit (purple) as well as individual Ni, Mg, and O waves.

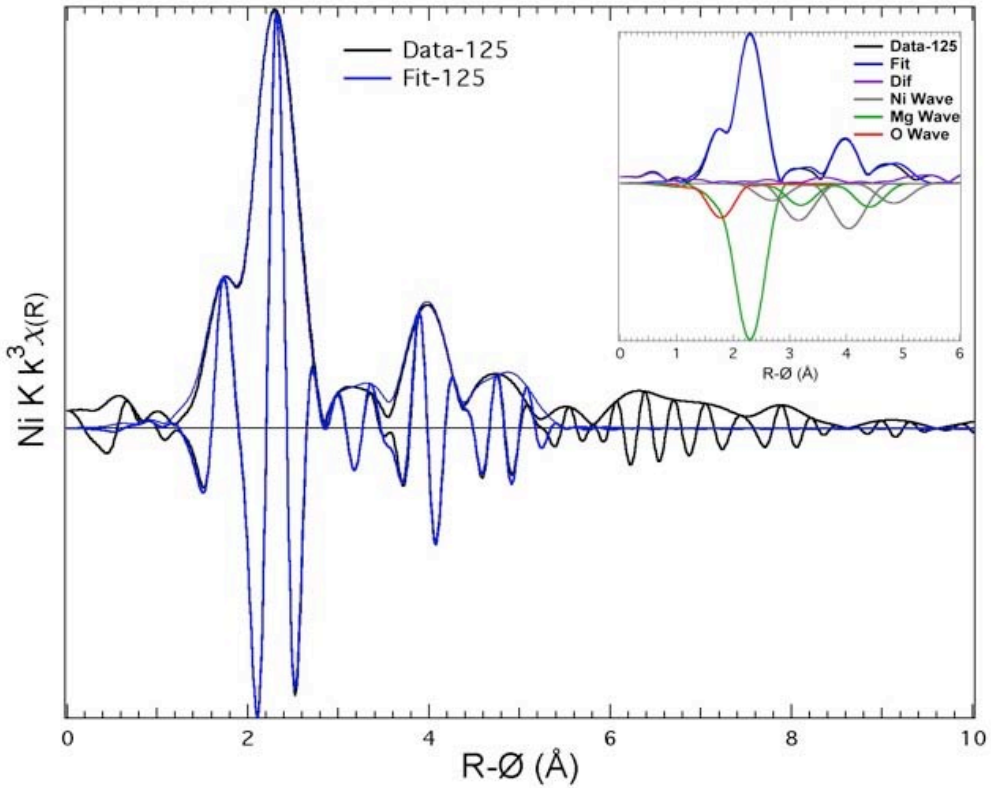

Figure 3-8: EXAFS results for sample 125 showing the fitted data. The inset shows the difference in the data and fit (purple) as well as individual Ni, Mg, and O waves.

The Ni environments in these magnesium nanoparticles are obviously much less ordered than in the pure metal, with this disorder most likely encompassing both fewer neighbors and anharmonic distributions. Where the spectra, and by inference the local environments, of the three samples differ substantially is in their extended structure beyond this nearest neighbor peak. The spectrum of sample 127, shown in Figure 3-7, displays a broad, complicated, and relatively large set of peaks at R=3–5 Å. The spectra of 125 (Figure 3-8) and 151 (Figure 3-9) display a series of small peaks, perhaps even as far as R=7 Å, but these do not resemble each other, leading to the conclusion that variation in the synthetic method do not modify the nearest, directly bonded neighbors but do affect how these smallest structural units consisting of the Ni and its nearest neighbors are incorporated into the nanoparticles.

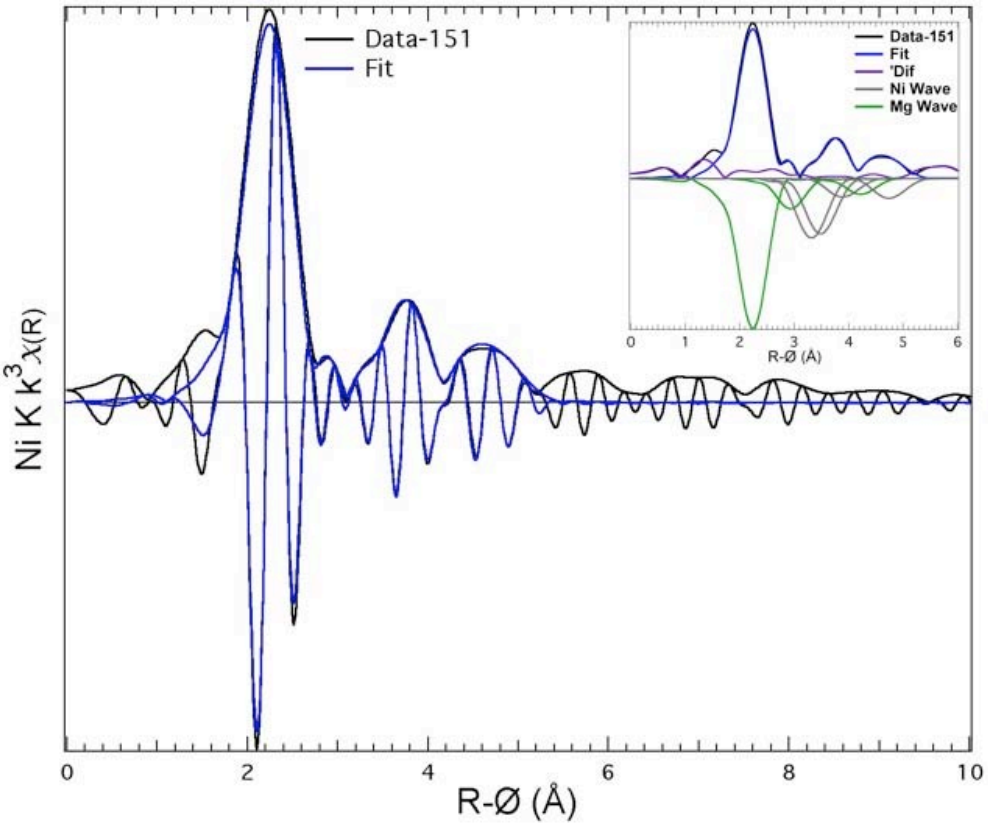

Figure 3-9: EXAFS results for sample 151 showing the fitted data. The inset shows the difference in the data and fit (purple) as well as individual Ni, Mg, and O waves.

The curve-fit results on the metal samples presented in Table 3-2 provide the metrical information that elucidates the actual structural parameters that produce these spectra. They corroborate and expand on the direct comparisons of the data. The most important parameter, both in terms of its relative contribution to the total EXAFS and the chemistry, is the identification of the nearest neighbor. In samples 125 and 151 an excellent fit to this highest amplitude peak is obtained with a single Mg shell at Ni-Mg distances of, respectively, 2.68 and 2.65 Å. These are in the 2.65–2.70 Å range of the Ni-Mg distances in the ordered intermetallic Mg_2Ni and therefore correspond well with known Ni-Mg bond lengths in zero valence systems. The largest peak in the spectrum of sample 127 requires both a Mg shell at a somewhat expanded 2.73 Å distance and a Ni shell at 2.46 Å. The overall amplitudes of these are comparable in the fit, which means that because of the greater backscattering amplitude of Ni and a slightly lower Debye-Waller factor (0.060 Å vs. a fixed value of 0.065 Å) the numbers of Ni atoms found by the fit is only around 20% of the number of Mg. Therefore, although both Mg and Ni shells are found, the Mg appears to dominate the Ni environment and does not differ too much from the others that are solely Mg. The low numbers of atoms found for this shell, 1.8, 1.2 (0.9 Mg, 0.3 Ni, with a lower Debye-Waller factor), and 1.8 are consistent with the very low amplitudes of this spectral feature relative to that in Ni metal and imply both coordinative unsaturation and a high degree of especially anharmonic static disorder.

Table 3-2: Crystallographic distances and $k^3 \chi(k)$ curve-fitting results.

Sample	Shell	Neighbor Atom	Distance	Coordination Number	Sigma	Delta Eo
nib125	6	O	2.17	0.2	0.050	2.59
	1	Mg	2.68	1.8	0.089	1.59
	3	Ni	2.99	0.1	0.070	3.59
	8	Ni	3.48	0.3	0.070	0.59
	7	Mg	3.58	0.4	0.070	2.59
	2	Ni	4.36	1.2	0.070	2.59
	4	Mg	4.80	0.8	0.070	1.59
	5	Ni	5.18	0.4	0.070	-0.41
nib125h	5	O	2.09	0.1	0.030	-1.96
	1	Ni	2.48	2.1	0.098	-0.96
	4	Ni	3.10	0.0	0.060	-1.96
	3	Mg	3.22	0.0	0.060	-0.96
	2	Ni	3.52	0.3	0.060	0.04
nib127	6	O	2.17	0.2	0.025	0.48
	8	Ni	2.46	0.3	0.060	0.48
	1	Mg	2.73	0.9	0.065	1.48
	3	Ni	3.03	0.2	0.070	2.87
	7	Ni	3.58	0.3	0.070	2.48
	2	Ni	4.34	1.6	0.070	0.48
	4	Mg	4.73	1.3	0.070	1.48
	5	Ni	5.18	0.5	0.070	-0.52
nib127h	5	O	1.00	0.0	0.040	-2.84
	1	Ni	2.47	1.7	0.092	-3.84
	4	Ni	3.06	0.1	0.060	-4.84
	3	Mg	3.26	0.4	0.060	-2.37
	2	Ni	3.51	0.3	0.060	-2.84
nib151	1	Mg	2.65	1.8	0.087	-3.53
	6	Mg	3.34	0.5	0.070	-2.53
	7	Ni	3.67	0.5	0.070	-2.53
	3	Ni	3.86	0.6	0.070	-5.53
	2	Ni	4.25	0.5	0.070	-2.53
	4	Mg	4.66	0.6	0.070	-3.53
	5	Ni	5.13	0.4	0.070	-5.53
nib151h	8	O	2.13	0.2	0.000	-1.16
	7	Mg	2.42	0.0	0.050	-1.16
	1	Ni	2.47	0.3	0.066	-2.16
	4	Ni	2.96	0.1	0.070	-1.16
	3	Mg	3.42	0.8	0.070	-0.28
	2	Mg	3.75	0.8	0.070	-1.16
	6	Mg	4.06	1.0	0.070	-1.16
	5	Mg	4.30	1.1	0.070	-1.16

The spectral features below the primary peak are partly fit by a C/N/H-type of atom. EXAFS, of course, cannot distinguish among these, so using the synthesis

chemistry the most likely candidate would be carbon. There is a reasonable correspondence between the fit and data and an improvement in the overall quality of the fit when this shell is included for the fits of the spectra from samples 125 and 127, but not 151. The Ni-C distances are 2.17 and 2.09 Å which are longer than anticipated for a Ni-C bond length (~1.86 Å). The numbers of atoms are quite low, 0.2 for both, with fixed Debye-Waller factors of 0.05 and 0.03 Å. However, because of the overall low amplitude of these spectra, even this small fraction makes a visible contribution to the data. It is possible that this is simply low frequency noise that is not removed during the background subtraction process. There is also spectral weight at still lower R, too low for physically reasonable neighbor shells. This again might be low frequency noise, or alternatively Atomic XAFS (AXAFS) that is again more prominent because of the low amplitude of the spectra.

Reasonable fits are obtained on the spectral features in the extended region beyond the nearest neighbor with a combination of Mg and Ni shells. Between the nearest neighbor peak and the features starting around R=4.4 Å the curve-fits of the three spectra from the metal samples, and especially 125 and 127, display some similarities and some differences in the arrangement of Ni and Mg neighbors that gives the best fit. These two elements are easily distinguished because of the differences in both phase and amplitude between them. However, consistent the differences in the spectra themselves in this region must be and are reflected in corresponding differences in the pattern of near neighbors and their locations found by the curve fits so there are no common neighbor shells or pattern. Beyond R=4.0 the three most distant shells are similar for all of the samples. These are the 0.5–1.3 Ni atoms at 4.24–4.36 Å, the 0.6–1.3 Mg atoms at 4.65–

4.80 Å, and the 0.4 Ni atoms at 5.13–5.18 Å. Sample 151 always gives the shorter distance and smallest number of atoms, 127 the largest number of atoms. These three shells might represent some type of common structural moiety, although it is not clear why it would occur at longer but not intermediate distances.

The overarching conclusion from the curve-fits of the metal samples is that the nearest neighbor, and specifically the preponderance or even monopoly of Mg atoms that are directly bonded to the Ni at a known Ni-Mg bond length, is by far the most dominant aspect of the Ni environment in the metal particles. An important aspect of this shell, however, is that it appears to be both disordered and highly unsaturated and this does not seem to be affected by varying the amount of added Ni dopant: the observed disorder appears to be consistent throughout all three samples.

Neutron scattering results- $MgD_2(Ni)$. Hydriding causes these materials to undergo substantial modifications in their structure. This is evident in the diffraction by the replacement of the Mg pattern with one that is obviously MgD_2, displayed in Figure 3-10. The tetragonal P 42/m n m space group for the data has lattice constants of a=b=4.5101 Å and c=3.0163 Å, while the reported ones are a=b=4.5147 Å and c=3.0193 Å. However, as with the metal sample, diffuse scattering from a combination of particle size effects and disorder broadens the bases of the Bragg peaks, sometimes asymmetrically, so that they are not fit well. This makes it difficult to discern if there are any features in the S(Q) that, also analogous to the metal, and perhaps more apparent in the difference plot, may not be associated with the MgD_2 pattern. Such features are observed, but mostly in proximity to diffraction peaks or sets of diffraction peaks so that they may just be overlap of the diffuse scattering.

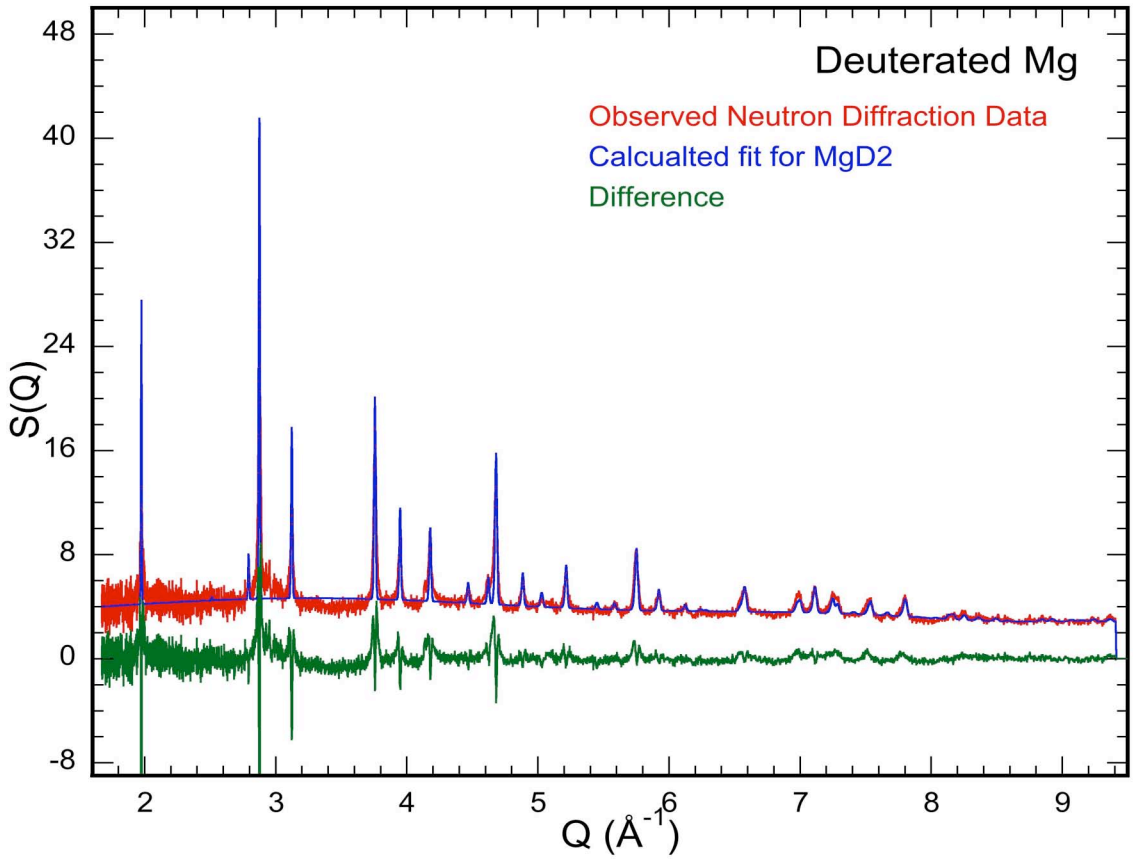

Figure 3-10: Neutron diffraction pattern of the hydrided sample modeled with the MgD_2 phase. Red indicates the raw data, blue the calculated fit, and green shows the difference between the two.

In the case of the MgD_2 pair distribution function, although the peaks in the data are broader than in the calculation of the magnesium deuteride g(r), almost all of them can be assigned to the ordered MgD_2 (see Figure 3-11). Nickel metal has the same peaks as the data in very few locations, as can be seen in Figure 3-12, indicating that these matches are likely coincidental. This is also true for the g(r) of the Mg_2Ni alloy, as is evident in Figure 3-13. Therefore, in the deuterated sample the aperiodic, both the diffraction and the pair distribution function indicate that the disordered component that we believe was a Mg-Ni mixture appears to have rearranged into a broadened but relatively ordered MgD_2 structure in tandem with the original metallic magnesium fraction.

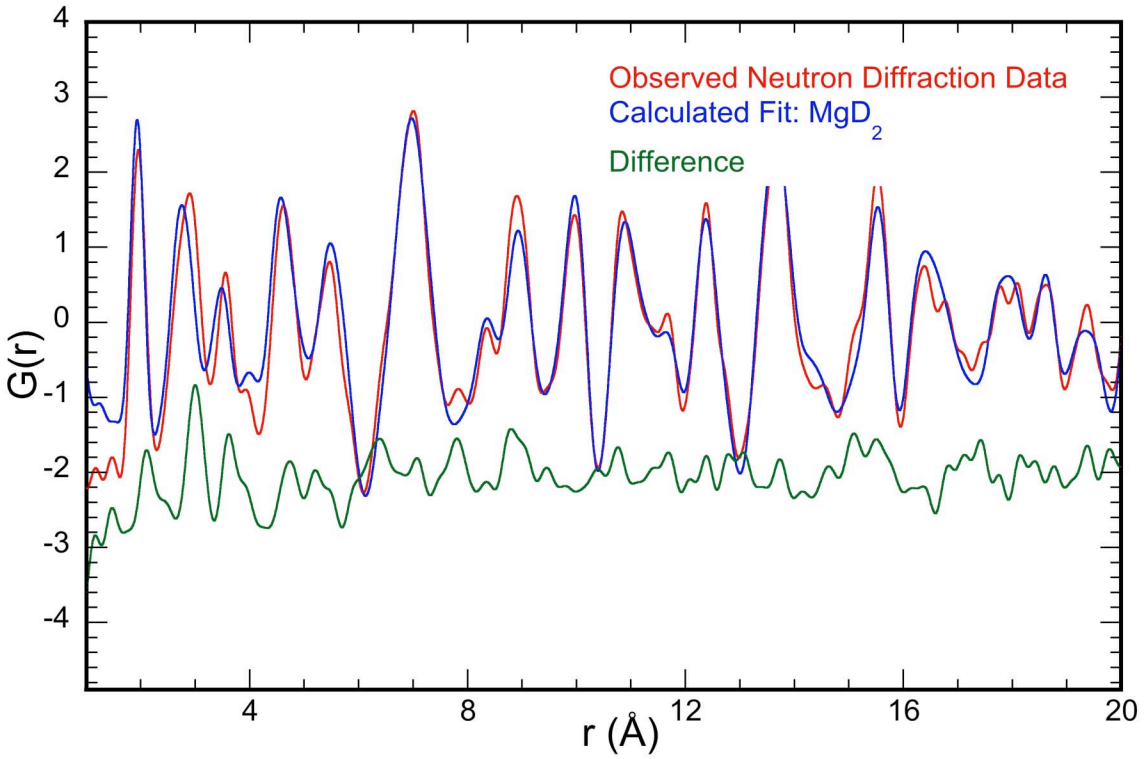

Figure 3-11: Pair distribution function for the magnesium deuteride sample modeled to the MgD_2 phase. Red indicates the raw data, blue the calculated fit, and green shows the difference between the two.

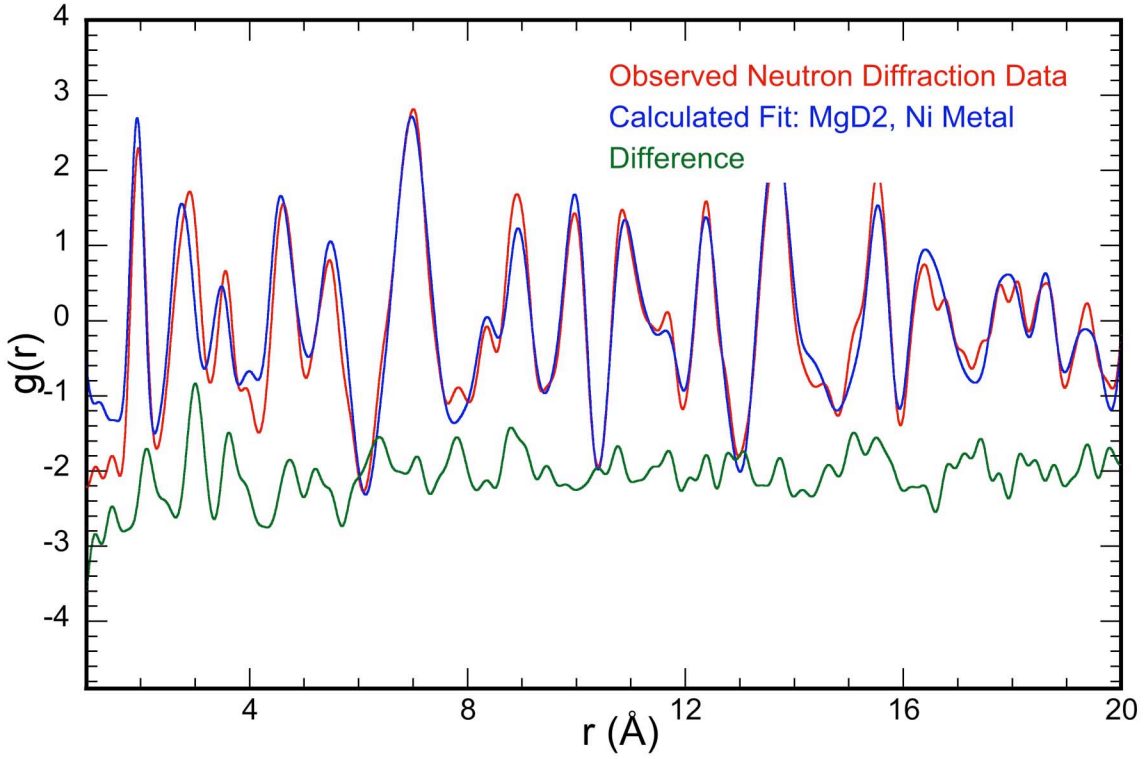

Figure 3-12: Pair distribution function for the deuteride sample modeled to metallic nickel. Red indicates the raw data, blue the calculated fit, and green shows the difference between the two.

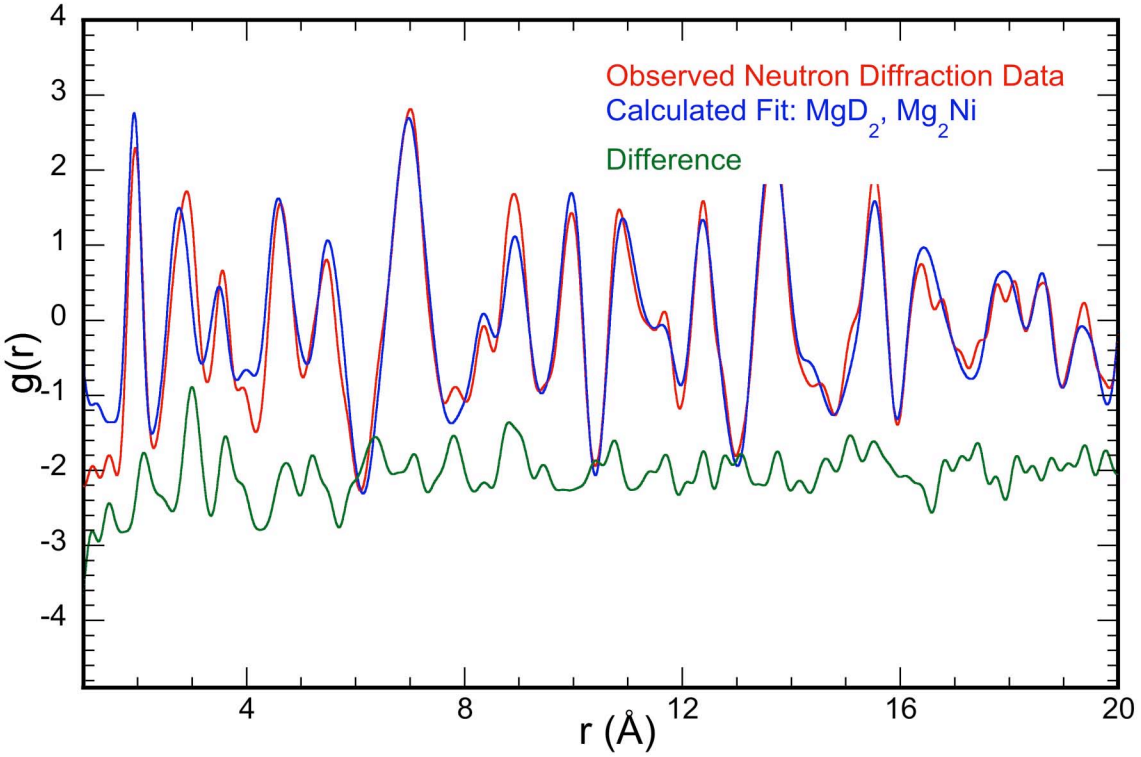

Figure 3-13: Pair distribution function for the MgD_2 sample fitted with an additional bimetallic phase, Mg_2Ni.

Fits of the hydrogenated Mg(Ni) (summarized in Table 3.3) were dominated by MgD_2 structure and fits including Mg_2Ni and Ni-metal failed to improve the χ^2 value for the fits. A shift in the peak position of the Mg-D peak leads to the conclusion that despite the definite MgD_2 structure, the deuterium is disordered.

Table 3-3: Summary of neutron scattering pdf fitting results for the MgD_2 sample.

Phases	χ^2	MgD_2 Scaling Factor	Mg Metal Scaling Factor	Mg_2Ni Scaling Factor	Ni Metal Scaling Factor
MgD_2	224.454	2.397			
MgD_2, Mg	220.412	2.414	0.021		
MgD_2, Ni-doped	221.681				
MgD_2, Ni	224.433	2.397			0.001
MgD_2, Mg_2Ni	218.447	2.435		-0.083	

Additional fitting to examine particle size and strain were performed in GSAS, but failed to return meaningful values. The disorder in the structure caused by both the

Ni and the cycling process prevented the construction of a sufficiently accurate fit to extract these parameters. Without an exact model of the disorder viewed in the deuterium and the Ni this fit is likely to remain only accurate enough to confirm the presence of these structures, but not sufficient to extract size and strain.

Ni XAFS results- MgD_2(Ni). The Ni XAFS also corroborate these results. The XANES of all three samples (see Figure 3.5) continue to be broad, featureless, and at energies only a small amount above the leading edge of the metal. The broad peak that was at 8358 eV in the metallic samples is now flatter in all three, so that the spectrum of the hydrided sample (125) more closely resembles those of the other two than it did when metallic. The interpretation continues to be that the absence of distinct spectral features reflects a highly disordered local environment.

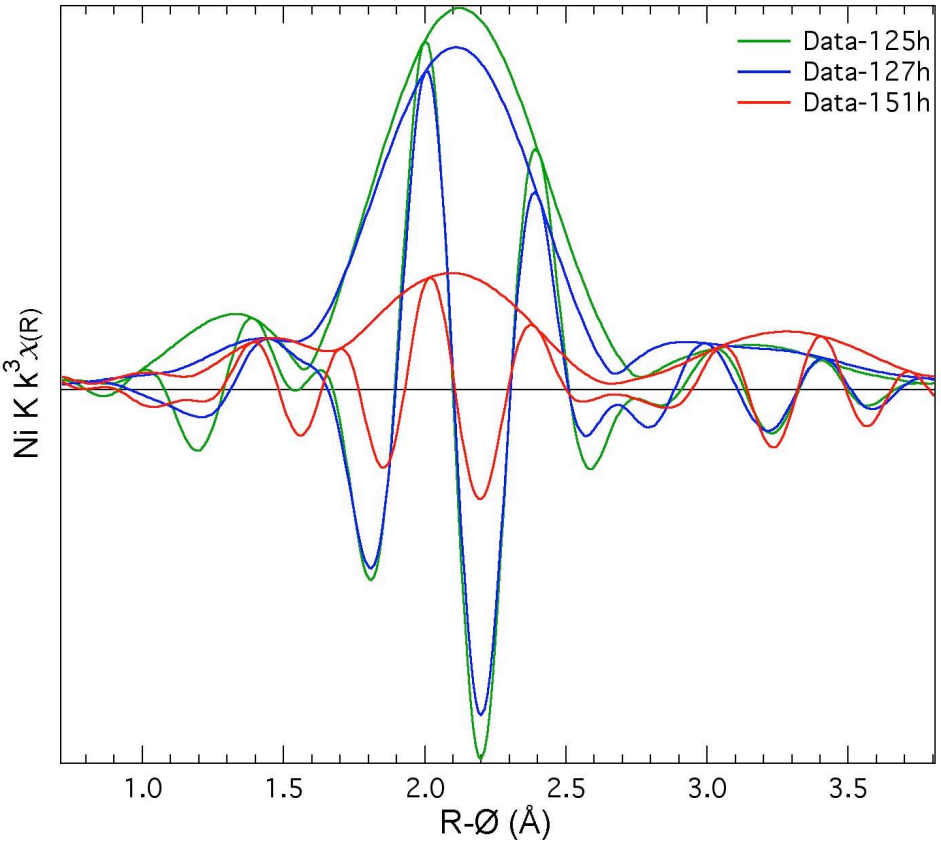

Figure 3-14: EXAFS, χ(R), data for the three hydrided samples.

The Fourier transforms of the EXAFS, χ(R), of these hydrided samples, just as in the metallic samples, are almost identical with each other in the pattern of the real component within the primary nearest neighbor contribution at R=2 Å. This can be seen in Figure 3-14, which compares all three hydrogenated samples. In contrast to the spectra of the metallic samples, in these the higher part of the asymmetric real component is below the modulus peak. This means that they match the pattern in Ni metal, suggesting that this shell that is the one that is directly bonded to the Ni central atom has shifted from being Mg rich to Ni. In the spectra of the 125 (Figure 3-15) and 127 (Figure 3-16) samples this peak increases in amplitude to 0.650 and 0.750 upon hydriding, which could result simply from the Ni nearest neighbors that have larger scattering amplitude than Mg. These are still much lower than in Ni metal.

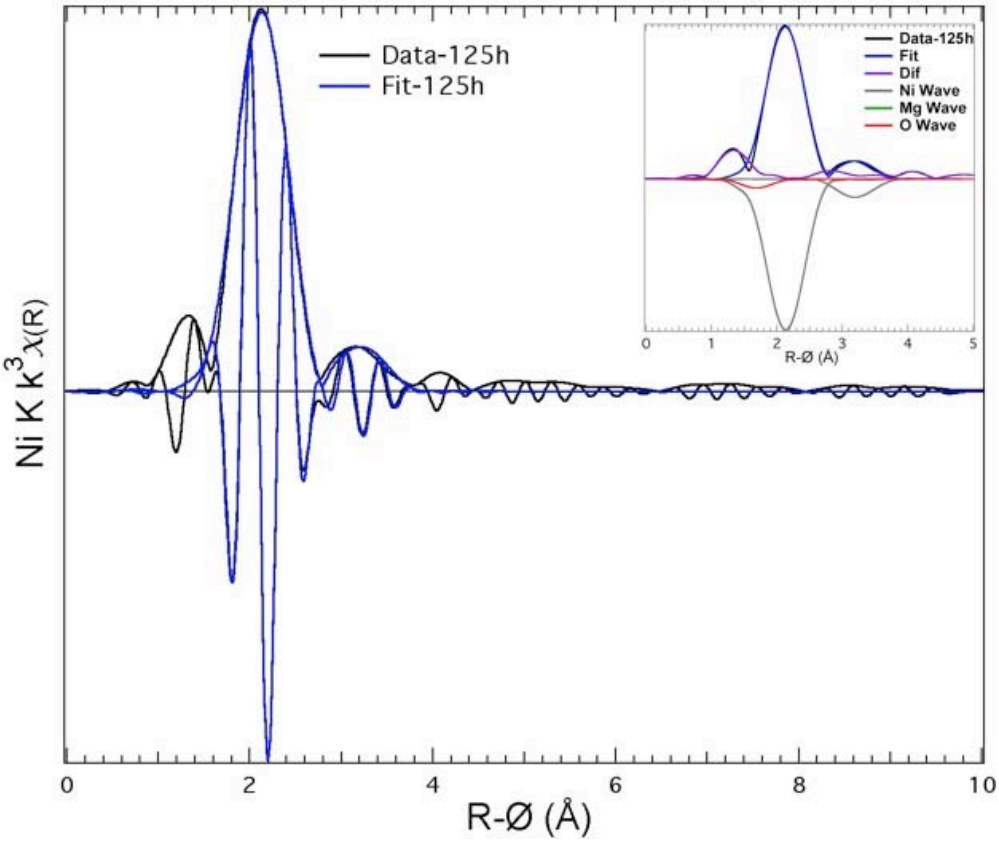

Figure 3-15: EXAFS, χ(R), data for the hydrided sample 125.

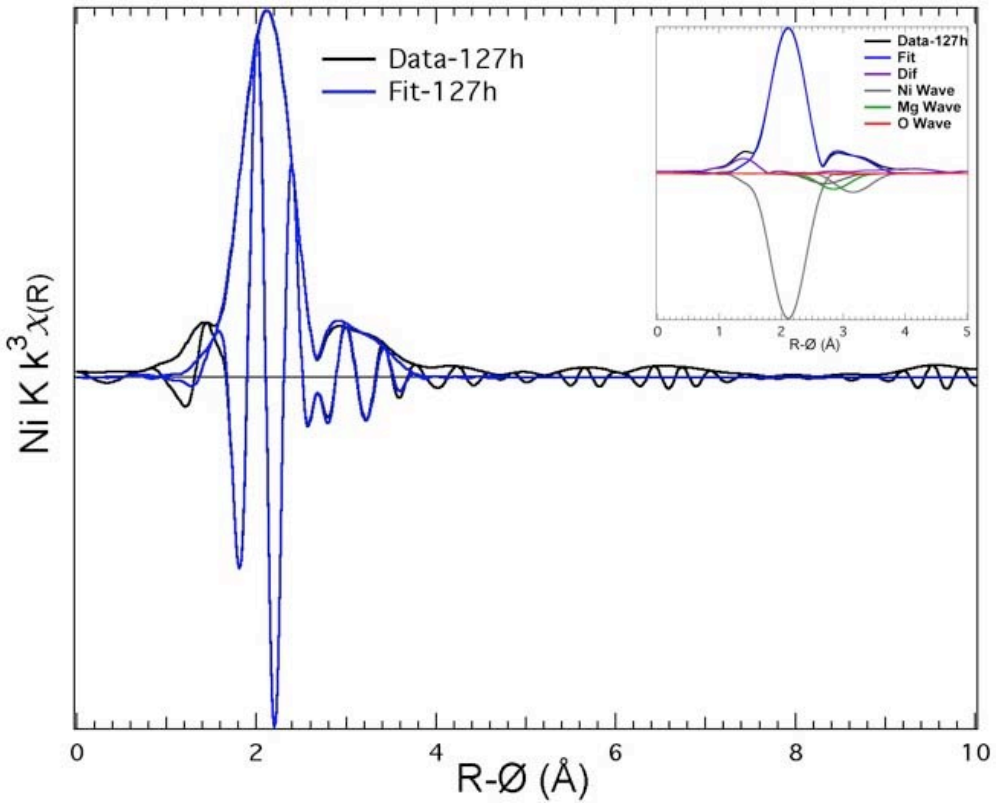

Figure 3-16: EXAFS results for hydrided sample 127.

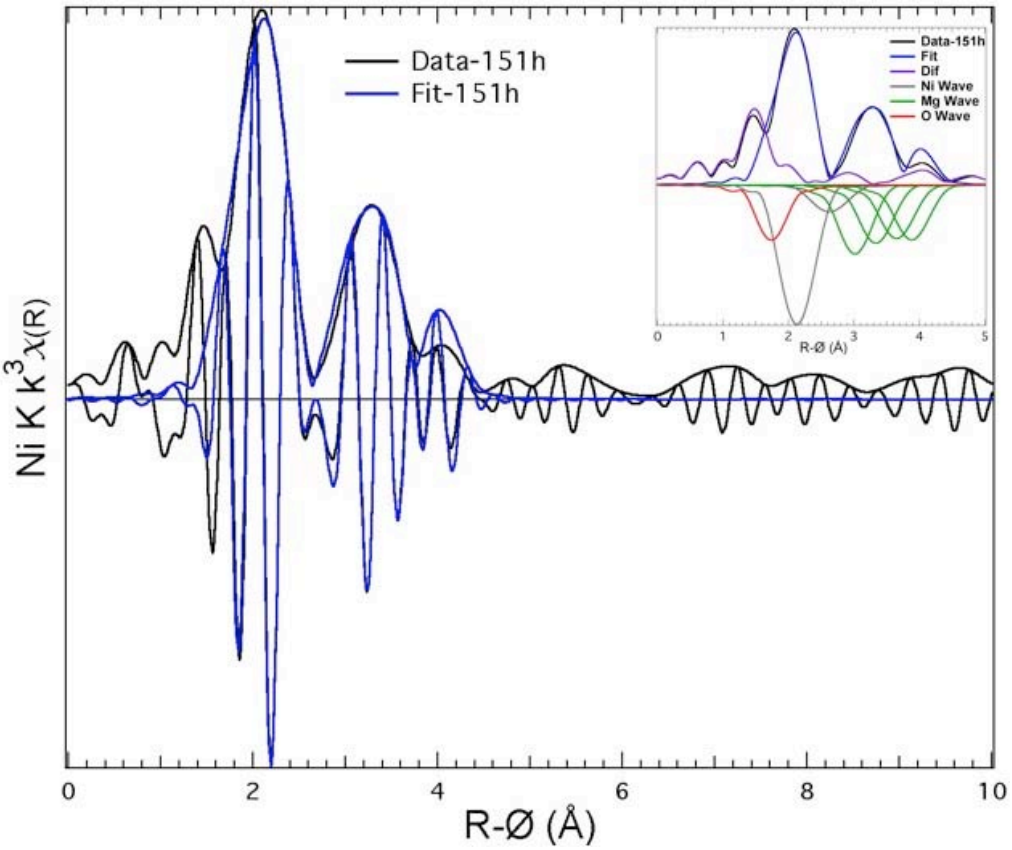

Figure 3-17: EXAFS results for hydrided sample 151.

In the spectrum of 151, however, this peak diminishes in amplitude from the metal to 0.2, so that, despite the similarity in the pattern, its amplitude is only a fraction of that of the other two. This is shown in Figure 3-17. Beyond this, all three spectra display higher R features – although only to R=4–4.5 Å – that differ from each other, as in the metal. The amplitudes of these features in the spectra of the hydrided samples are both higher and lower than in the metallic ones (see Figure 3-17 for a comparison of metallic vs. hydrided), but are always roughly comparable without the substantial differences in the nearest neighbor contribution. There is thus no evidence that the longer-range order is modified in a consistent way by the change in the nearest neighbors, suggesting that the clusters formed by the bonded Ni atoms are at most only a few atoms in size nor do they organize the atoms beyond them.

The curve fits for the hydrided samples (see Table 3-2) give definitive proof of this shift from the Ni atoms bonded to Mg neighbors in the metal samples to Ni neighbors in the hydrides. The largest peak in the spectra that is the contribution of the nearest neighbor is well fit by a single Ni shell for all three samples. The Ni-Ni distance of 2.47 Å is only slightly shorter than the 2.492 Å of Ni metal and significantly shorter than the expanded 2.645 Å Ni-Ni distance in Ni-H. This bond length therefore indicates metallic Ni in these samples. As with the metal samples, the numbers of atoms are quite low, 1.7 and 2.1 for the 125 and 127 samples and only 0.3 atoms in the 151 sample where the amplitude of this feature in the spectrum is lower than that of the metal sample, in contrast to the increased amplitude for the others. The Debye-Waller factors are reasonable, indicating substantial harmonic disorder in 125 and 127 and less for 151, which would account for some of the reduction in the number of atoms. These hydrided

materials that have only Ni-Ni metal-type bonds instead of Ni-Mg therefore have the same coordination unsaturation and (most likely) anharmonic disorder as the metallic ones despite this complete rearrangement of the Ni neighbors resulting from the hydriding.

The 125 and 151 hydride samples also have components below this nearest neighbor Ni contribution that can be fit with a first row C/N/O atom. The distances are somewhat contracted and the numbers somewhat smaller than in the 125 and 127 metal samples where this shell also improved the fit. However, as with the metal samples, given the inconsistency of their behavior it is difficult to determine if these shells are actually present or if they are simply fitting a C/N/O-like component of the low frequency noise. There also continues to be spectral weight at lower R, which again might be AXAFS or noise. Fitting the spectra at higher R values is more successful. These features are lower in amplitude and simpler in the hydride than in the metal spectra, an observation that is also reflected in the fit results. The 125 spectrum only requires one additional shell, 0.3 Ni at 3.52 Å, and the 127 spectrum only three additional shells, this same Ni shell at only 0.02 Å lower, plus another Ni and Mg shell at lower distances. The low amplitude 151 spectrum is best fit with one additional Ni and four Mg shells between 2.96 and 4.30 Å that appear unrelated to the ones in the other two samples. This combination fits the data well, but is problematic because it largely depends on destructive interference to accomplish this and the amplitudes of the individual shells are excessive relative to the data. What is confirmed is that there is some longer-range order beyond the nearest neighbor that is a combination of Mg and Ni.

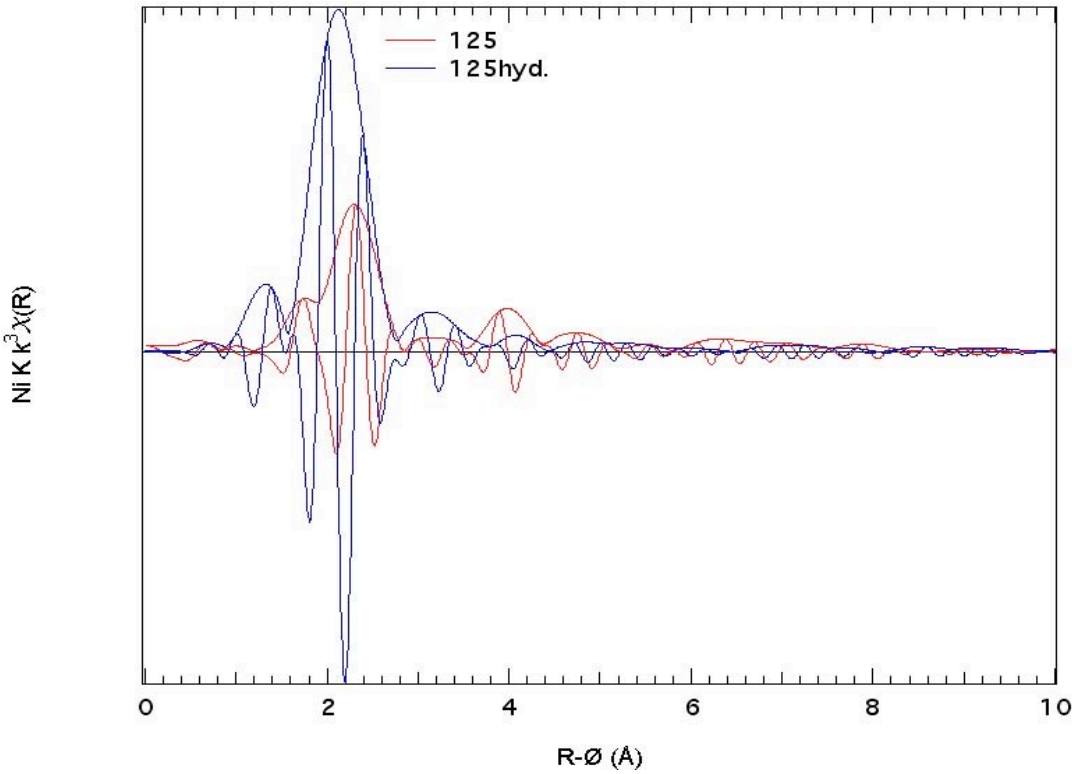

Figure 3-17: Comparison of metallic sample 125 with the corresponding hydrided sample.

The combined experiments indicate a chemically complicated mechanism for the hydride formation and reversion to the metal. The metallic materials consist of two components, ordered Mg metal and an aperiodic and disordered Ni-Mg compound in which the Ni is dispersed throughout the Mg so that the number of Ni-Ni bonds is small or zero. On reaction with hydrogen most or even all of the Mg is converted to the hydride. In undergoing this conversion the Ni is ejected from the Mg – perhaps because it is not soluble in the MgD_2 phase as either the metal or the hydride. These Ni atoms then form bonds with each other, but because they began widely separated from each other and may be trapped inside the Mg host they form very small clusters consisting of only a few atoms and not domains of Ni metal or hydride. In both the disordered Mg-Ni compound and the clusters the Ni has a low number of bonds and appears highly unsaturated.

3.4 Conclusions

Neutron scattering and XAS results have shown that significant structural changes occur during the hydrogenation/dehydrogenation cycling of the Ni-doped magnesium nanoparicles. The local atomic structure analysis shows the hydrogen storage material does not exhibit long-range ordering of Ni dopant, either as nickel islands on the surface of the magnesium particles or as a known Mg-Ni alloy. Both the neutron pdf and XAS demonstrate that the material is highly disordered. The neutron data match to Mg and MgD_2 in the respective samples, but the additional peaks do not index well to any other known structures of Mg/Ni, suggesting a lack of long-range order within in the material. The XANES is consistent with a highly disordered structure, which remains disordered upon hydriding. The broad featureless spectrum suggests low coordination numbers around the atoms as well as small numbers of total nearest neighbors. This is corroborated in the XAFS in which the first shell is highly disordered, while the second and third shells appear more ordered having comparable amplitudes, suggesting the same number of atoms. These results suggest isolated Ni atoms within the material, contrary to the theory that Ni islands might form on the surface, or that a Mg/Ni alloy might form. This information could help to explain the dramatically enhanced kinetics of the hydrogen cycling that we have observed, as the differences seen cannot be explained solely based on reduced particle size. The disorder of the material likely adds to the improved kinetics. This conclusion is consistent with previously published results on the increased rates of hydrogenation accompanying the addition of defects to the crystalline material.[54] Sato and coworkers reported on the improvement in hydrogen storage properties of Mg_2Ni by purposefully destabilizing the material by adding in aluminum

defects.[55] In the future it will be useful to repeat such experiments on samples that have been hydrogen cycled more than once to see if this disorder within the material changes over the cycling life of the material, a key aspect to applicability as a vehicular on-board fuel storage system.

What is intriguing is the possibilities this process may have for modifying the material to tailor its properties. The control over the uptake and loss of hydrogen is controlled by the solubilities of Ni in Mg metal and hydride relative to the energies of the of the Ni-Mg and Ni-Ni bonds in the aperiodic Ni-Mg compound and the small Ni clusters. The dispersal of the Ni or a different element in the Mg metal disrupts its structure, which should facilitate the reaction with hydrogen. Low solubility of the trace metal in the hydride that causes it to be ejected and the subsequent formation of pure, ordered MgH_2, however, will impede the release of the hydrogen and reversion to the original form. Finding an element as effective as Ni in intruding into Mg while subsequently doing the same in the hydride should make a better material, although this must be balanced against the lowered stability of the disordered hydride structure.

References:

(1) Schlapbach, L.; Zuttel, A. *Nature* **2001**, *414*, 353.
(2) Schlapbach, L. *Nature* **2009**, *460*, 809.
(3) Sakintuna, B.; Lamari-Darkrim, F.; Hirscher, M. *International Journal of Hydrogen Energy* **2007**, *32*, 1121.
(4) Latroche, M. *Journal of Physics and Chemistry of Solids* **2004**, *65*, 517.
(5) Eberle, U.; Arnold, G.; von Helmolt, R. *Journal of Power Sources* **2006**, *154*, 456.
(6) Zuttel, A. *Materials Today* **2003**, *6*, 24.
(7) Schuth, F.; Bogdanovic, B.; Felderhoff, M. *Chemical Communications* **2004**, 2249.
(8) Aguey-Zinsou, K.-F.; Ares-Fernandez, J.-R. *Energy & Environmental Science* **2010**, *3*, 526.
(9) Bogdanovic, B. *International Journal of Hydrogen Energy* **1984**, *9*, 937.
(10) Bogdanovic, B.; Hofmann, H.; Neuy, A.; Reiser, A.; Schlichte, K.; Spliethoff, B.; Wessel, S. *Journal of Alloys and Compounds* **1999**, *292*, 57.
(11) Vigeholm, B.; Kjoller, J.; Larsen, B. *Journal of the Less Common Metals* **1980**, *74*, 341.
(12) Zaluska, A.; Zaluski, L.; Strom-Olsen, J. O. *Applied Physics A: Materials Science & Processing* **2001**, *72*, 157.
(13) Pedersen, A. S.; Vigeholm, B.; Kjoller, J.; Larsen, B. *International Journal of Hydrogen Energy* **1987**, *12*, 765.
(14) Fernandez, J. F.; Sanchez, C. R. *Journal of Alloys and Compounds* **2002**, *340*, 189.
(15) Topler, J.; Buchner, H.; Saufferer, H.; Knorr, K.; Prandl, W. *Journal of the Less Common Metals* **1982**, *88*, 397.
(16) Stioui, M.; Grayevsky, A.; Resnik, A.; Shaltiel, A.; Kaplan, N. *Journal of the Less Common Metals* **1986**, *123*, 9.
(17) Friedlmeier, G.; Groll, M. *Journal of Alloys and Compounds* **1997**, *253 254*, 550.
(18) Klassen, T.; Oelerich, W.; Bormann, R. *Materials Science Forum* **2001**, *360-362*, 603.
(19) Huot, J.; Liang, G.; Schulz, R. *Applied Physics A: Materials Science & Processing* **2001**, *72*, 187.
(20) Paskevicius, M.; Sheppard, D. A.; Buckley, C. E. *Journal of the American Chemical Society* **2010**, *132*, 5077.
(21) Zaluska, A.; Zaluski, L.; Strom-Olsen, J. O. *Journal of Alloys and Compounds* **1999**, *288*, 217.
(22) Zaluski, L.; Zaluska, A.; Strom-Olsen, J. O. *Journal of Alloys and Compounds* **1997**, *253-254*, 70.
(23) Imamura, H.; Masanari, K.; Kusuhara, M.; Katsumoto, H.; Sumi, T.; Sakata, T. *Journal of Alloys and Compounds* **2005**, *386*, 211.

(24) Berube, V.; Radtke, G.; Dresselhaus, M.; Chen, G. *International Journal of Energy Research* **2007**, *31*, 637.
(25) Grochala, W.; Edwards, P. P. *Chemical Reviews* **2004**, *104*, 1283.
(26) Guoxian, L.; Erde, W.; Shoushi, F. *Journal of Alloys and Compounds* **1995**, *223*, 111.
(27) Schulz, R.; Huot, J.; Liang, G.; Boily, S.; Lalande, G.; Denis, M. C.; Dodelet, J. P. *Materials Science and Engineering A* **1999**, *267*, 240.
(28) Liang, G.; Huot, J.; Boily, S.; Neste, A. V.; Schulz, R. *Journal of Alloys and Compounds* **1999**, *292*, 247.
(29) Liang, G.; Huot, J.; Boily, S.; Neste, A. V.; Schulz, R. *Journal of Alloys and Compounds* **1999**, *291*, 295.
(30) Liang, G.; Huot, J.; Boily, S.; Schulz, R. *Journal of Alloys and Compounds* **2000**, *305*, 239.
(31) Schimmel, H. G.; Hout, J.; Chapon, L. C.; Tichelaar, F. D.; Mulder, F. M. *Journal of the American Chemical Society* **2005**, *127*, 14348.
(32) Charbonnier, J.; Rango, P. d.; Fruchart, D.; Miraglia, S.; Skryabina, N.; Huot, J.; Hauback, B.; Pitt, M.; Rivoirard, S. *Journal of Alloys and Compounds* **2005**, *404-406*, 541.
(33) Hanada, N.; Ichikawa, T.; Fujii, H. *Journal of Alloys and Compounds* **2005**, *404-406*, 716.
(34) Checchetto, R.; Bazzanella, N.; Miotello, A.; Mengucci, P. *Journal of Alloys and Compounds* **2007**, *446*, 58.
(35) Bououdina, M.; Guo, Z. X. *Journal of Alloys and Compounds* **2002**, *336*, 222.
(36) Aguey-Zinsou, K.-F.; Fernandez, J. R. A.; Klassen, T.; Bormann, R. *International Journal of Hydrogen Energy* **2007**, *32*, 2400.
(37) Aguey-Zinsou, K.-F.; Nicolaisen, T.; Fernandez, J. R. A.; Klassen, T.; Bormann, R. *Journal of Alloys and Compounds* **2007**, *434-435*, 738.
(38) Barkhordarian, G.; Klassen, T.; Bormann, R. *Journal of Alloys and Compounds* **2006**, *407*, 249.
(39) Bhat, V. V.; Rougier, A.; Aymard, L.; Nazri, G. A.; Tarascon, J.-M. *Journal of Alloys and Compounds* **2008**, *460*, 507.
(40) Gupta, R.; Agresti, F.; Russo, S. L.; Maddalena, A.; Palade, P.; Principi, G. *Journal of Alloys and Compounds* **2008**, *450*, 310.
(41) Hanada, N.; Hirotoshi, E.; Ichikawa, T.; Akiba, E.; Fujii, H. *Journal of Alloys and Compounds* **2008**, *450*, 395.
(42) Mandzhukova, T.; Khrussanova, M.; Grigorova, E.; Stefanov, P.; Khristov, M.; Peshev, P. *Journal of Alloys and Compounds* **2008**, *457*, 472.
(43) Varin, R. A.; Czujko, T.; Wasmund, E. B.; Wronski, Z. S. *Journal of Alloys and Compounds* **2007**, *446-447*, 63.
(44) Jung, K. S.; Lee, E. Y.; Lee, K. S. *Journal of Alloys and Compounds* **2006**, *421*, 179.
(45) Oelerich, W.; Klassen, T.; Bormann, R. *Journal of Alloys and Compounds* **2001**, *315*, 237.
(46) Oelerich, W.; Klassen, T.; Bormann, R. *Advanced Engineering Materials*

2001, *3*, 487.
(47) Dehouche, Z.; Klassen, T.; Oelerich, W.; Goyette, J.; Bose, T. K.; Schulz, R. *Journal of Alloys and Compounds* **2002**, *347*, 319.
(48) Barkhordarian, G.; Klassen, T.; Bormann, R. *Journal of Alloys and Compounds* **2004**, *364*, 242.
(49) Aguey-Zinsou, K.-F.; Ares-Fernandez, J.-R. *Chemistry of Materials* **2008**, *20*, 376.
(50) Ares, J. R.; Aguey-Zinsou, K.-F.; Klassen, T.; Bormann, R. *Journal of Alloys and Compounds* **2007**, *434-435*, 729.
(51) Arthur, T. S. Dissertation, Colorado State University, 2010.
(52) Farrow, C. L.; Juhás, P.; Liu, J. W.; Bryndin, D.; Božin, E. S.; Bloch, J.; Proffen, T.; Billinge, S. J. L. *Journal of Physics: Condensed Matter* **2007**, *19*, 335219.
(53) Conradson, S. D.; Begg, B. D.; Clark, D. L.; den Auwer, C.; Ding, M.; Dorhout, P. K.; Espinosa-Faller, F. J.; Gordon, P. L.; Haire, R. G.; Hess, N. J.; Hess, R. F.; Keogh, D. W.; Morales, L. A.; Neu, M. P.; Paviet Hartmann, P.; Runde, W.; Tait, C. D.; Veirs, D. K.; Villella, P. M. *Journal of the American Chemical Society* **2004**, *126*, 13443.
(54) Janot, R.; Cuevas, F.; Latroche, M.; Percheron-Guegan, A. *Intermetallics* **2006**, *14*, 163.
(55) Sato, T.; Blomqvist, H.; Noreus, D. *Journal of Alloys and Compounds* **2003**, *356-357*, 494.

Chapter 4: Local structure analysis of Cu_2ZnSnS_4 (CZTS) nanoparticles via x-ray absorption fine structure (XAFS) spectroscopy and neutron diffraction[iv]

4.1 Introduction

One of the definitive goals of solar energy research is to reach global terawatt-scale energy production. In order for photovoltaic (PV) technology to be competitive with current carbon-based fuels, it is necessary to fabricate low cost, robust, high conversion efficiency solar cells. The cost of silicon PV systems, the current industry standard, is still too high to have a significant impact on energy production at the commercial level.[1] This limitation is the predominant reason why solar power currently provides less than 0.1% of global energy demand.[2] Recently, the study of lower cost solar cells has shown potentially commercially viable options such as $CuIn_{1-x}Ga_xSe_2$ (CIGS) thin film solar cells, which have shown conversion efficiencies as high as 19.9% as well as high optical absorption coefficient in comparison to polycrystalline silicon solar cells.[3] This material, however, is not ideal as a silicon replacement due to two major disadvantages: the first is that it contains indium, which becomes problematic due to its scarcity and therefore increased cost; the second is that the chalcogen, selenium, is considered toxic.[4,5] These concerns become a hindrance to mass-producing such materials for eventual terawatt-scale energy production.[6]

[iv] Samples for experiments were prepared by Shannon C. Riha, Laura Wally and Sarah J. Fredrick. XAFS experiments were run at SSRL by Steven D. Conradson. Neutron scattering data were obtained by Sven Vogel and Mary B. Martucci at the Lujan Neutron Scattering Center at Los Alamos National Laboratory. Neutron data were analyzed by Dylan Conradson, Sven Vogel and Mary B. Martucci.

Cu_2ZnSnS_4 (CZTS) is a solar absorber composed of naturally abundant materials with a direct band gap of ~1.5 eV as well as a large optical absorption coefficient (~10^4 cm^{-1}), making it an extremely promising candidate for use as the absorber layer in thin film solar cells.[7-13] Much effort in research has been placed on the development of this material as a thin film photovoltaic. Many methods have been used to synthesize high-purity thin films of the quaternary material, including pulsed laser deposition, multi-source vacuum evaporation, sol-gel sulfurization, electrodeposition, spray pyrolysis, and photochemical deposition followed by sulfurization. However, these techniques are often costly or necessitate high annealing temperatures (>500 ℃), and can yield binary and ternary metal sulfide impurities along with the desired product.[14-34] This is problematic to the intended application in the solar cell industry, as it is well established in the literature that the optical properties of the CZTS films are extremely sensitive to small changes in composition.[35-38] For example, losses of tin have been observed in several of the aforementioned synthetic methods that require a high-temperature annealing step above 500 ℃. This effect is attributed to the evaporation of SnS during this annealing step, and as a result changes in device performance result.[39-42] Seeing the need to circumvent this high-temperature annealing step, Wang and Gong developed a lower temperature thin film synthesis and annealing of CZTS using the binary sulfides. In this case the annealing step was below the temperature at which other groups have observed the loss of tin, however, in this instance Cu_2S was found as an impurity.[43] It is clear that precise control over the reaction and resulting product is essential to the success of this material as a photovoltaic device.

Recently, our group has developed a solution-based hot-injection nanoparticle synthesis of this quaternary material. This one-pot solution-phase nanoparticle synthesis method eliminates the problematic issue of impurity phases and allows precise control over particle size and morphology.[44] This approach also affords the additional advantage of being able to manipulate the suspended particles as nanocrystal "inks", a printable solution of nanocrystals, which is then used to fabricate 3-D arrays or annealed thin films of the material, allowing a simple and cost-effecive process for device fabrication.[45-47] Our group has developed a reliable method for dip-casting these nano-inks onto flourine-doped tin oxide (FTO) substrates followed by an annealing step at 350 ℃ to create thin films of the photoactive material. However, it has been observed that this heat treatment changes the optical absorption of the CZTS films to have a much steeper onset as well as changing the band gap from 1.45 eV to 1.56 eV for the stoichiometric CZTS films.[48] As mentioned previously, the optoelectrical properties of the CZTS films are extremely sensitive to minor changes in structure and composition. The characterization of these nanoparticles and dip-cast films do not suggest any binary or ternary impurities evaporating or solid state conversion to another crystal structure during the annealing process, suggesting that this change in abosorption may be due to far more subtle structural variations.

In order to determine if these changes in the optical properties are the result of local structural changes in the lattic occuring during the annealing step, we have completed neutron diffraction and x-ray absorption fine structure (XAFS) spectroscopy experiements on as-prepared and annealed powder samples of the CZTS nanoparticles. These two techniques are highly complementary for the local structure analysis of the

CZTS material. XAFS is extremely sensitive to changes in the bond lengths between pairs of atoms. While any subtitution occuring between the Cu and Zn sites would be invisible to x-ray absorption spectroscopy techniques (as well as bulk x-ray diffraction methods), their neutron scattering cross sections (Cu= 8.03; Zn=4.13) differ significantly such that neutron scattering can distinguish between them and verify any substitution occuring between the zinc and copper sites within the material. Previous work has been done using neutron scattering to determine if anti-site substitution is occuring in CZTS powders. Schorr demonstrated that anti-site substitution between the copper and zinc is observed in theie prepared kesterite powders, meaning that intrinsic point defects were observed in which Cu substituted into Zn sites and Zn substituted into Cu sites in the structure.[49] It will be interesting to see if we observe the same anit-site substitution from our synthetic method that Schorr observed. Going a step further, our study should elucidate any local structural changes via the XAFS affording an explanation for the observed changes in the optical properties resulting from the heat treatment in the CZTS thin-film synthesis.

4.2 Experimental

Sample Preparation- Samples of ~10 nm Cu_2ZnSnS_4 nanocrystals were synthesized and characterized according to procedures outlined in reference (9).

XAS and Neutron Diffraction Sample Preparation- Two separate sets of samples were prepared: the first set for neutron scattering analysis; the second set for XAFS measurements. Both sets included two powder samples: an un-annealed, as-prepared sample from the hot-injection reaction, and a second sample prepared via the same

synthesis followed by the annealing process outlined in reference (23). X-ray absorption spectroscopy samples were run at the Stanford Synchrotron Radiation Lightsource (SSRL). Neutron scattering data was collected at the Lujan Neutron Scattering Center at Los Alamos National Laboratory on the high-pressure-preferred orientation (HIPPO) beamline.

XAS and Neutron Diffraction Data Analysis- X-ray measurements were performed and the data analyzed by standard procedures.[50] Neutron data were analyzed using the General Structure Analysis System (GSAS) structure fitting software.

4.3 Results and Discussion

Neutron scattering as well as XAS experiments were completed for non-annealed and annealed samples. The neutron data shows a good fit in both cases, annealed and non-annealed samples, for the Cu_2ZnSnS_4 crystal structure (space group I -4 2 m). As would be expected, the annealed sample shows sharper, more intense peaks (Figure 4.1) consistent with the enhanced ordering resulting from the annealing.

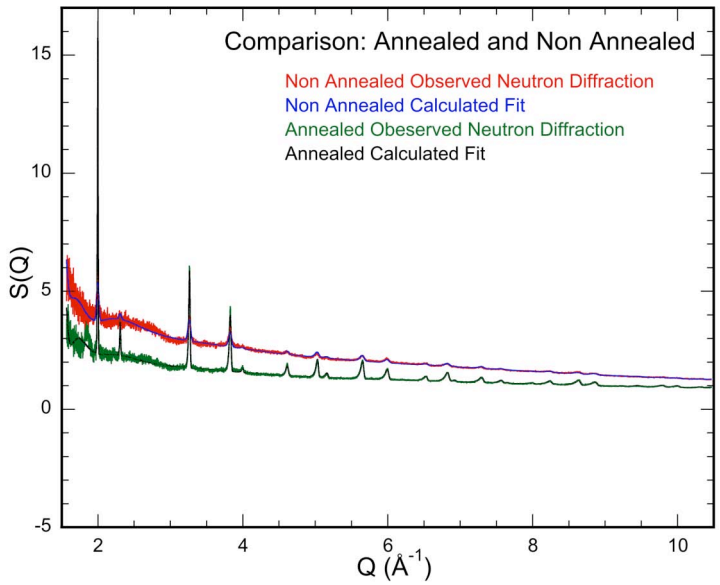

Figure 4.1: Neutron scattering data and fits for both the annealed and unannealed samples. Note the similarity in the patterns, with the annealed sample showing more intense and sharper peaks at the same positions as the unannealed.

Fractional occupancy for Cu and Zn was fit using two separate phases to determine the fraction. The fractions reflect the stoichiometric CZTS compound. From this analysis, it has been determined that there is very little Cu on the [0, ½, ¼] site (mixed site). Cu/Zn is 10/90 for the annealed sample and 5/95 for the unannealed one. Since annealing should enhance the ordering this result could suggest the presence of disordered material or a second phase that is becomes crystalline CZTS on annealing but distributes its Cu more widely than in the initial material. From the profile parameters that contribute to strain broadening, percentage strain was calculated to be 0.6% for the unannealed and 0.3% for the annealed samples. This decrease in strain upon annealing is consistent with expectations.

Based on the nodes of the real components, there is reasonable agreement between the Cu EXAFS calculated from the crystal structure and the measured ones through R=5.5 Å, beyond which the nodes do not align (Figure 4.2). The difference in amplitudes indicates that this agreement originates in similarities in the locally ordered components of the structure but that there is a substantial locally disordered fraction as well. This disorder and the reduction in the contributions of multiple scattering paths that are greatly overestimated in the calculated FeFF data could account for the differences in the shape of the modulus, although the difference between the two experimental spectra indicates that the local minimum near R=3.7 Å is caused by a change in a structural component. The annealed does show better correspondence with the calculation than the unannealed at that location. This will be verified by curve-fits, which are summarized in Table 4.1.

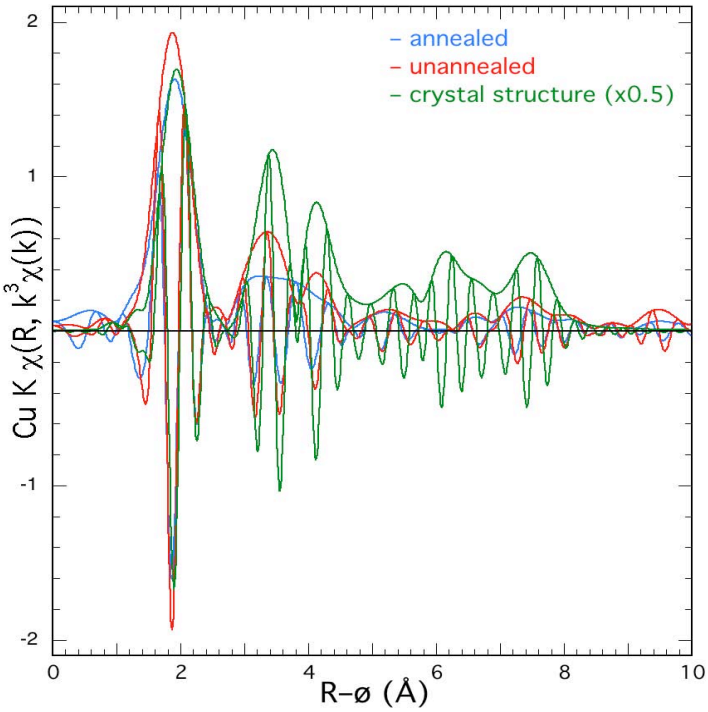

Figure 4.2: Experimental and calculated Cu EXAFS data for Cu_2ZnSnS_4. Blue spectrum shows experimental results for the annealed sample; red depicts experimental data for the as-prepared sample; green shows the data calculated from the crystal structure.

Table 4.1: Summary of cuve fitting results for Cu XAFS data.

Sample	Shell	Neighbor Atom	Distance	Coordination Number	Sigma	ΔE_0
Cu, as-prepared	1	S	2.31	3.9	0.077	1.53
	5	S	3.22	0.2	0.040	0.54
	3	Sn	3.77	3.5	0.077	-0.31
	2	Zn	3.81	5.0	0.077	-0.46
	4	S	4.45	23.3	0.016	1.54
Cu, annealed	1	S	2.29	3.8	0.067	-2.76
	5	S	3.24	0.4	0.040	-3.76
	2	Zn	3.80	11.0	0.122	-4.76
	3	Sn	3.88	6.5	0.110	-1.49
	4	S	4.47	11.4	0.098	-2.76
Cu, calculated	1	S	2.33	4.9	0.043	-0.41
	2	Zn	3.86	11.0	0.081	-2.41
	3	Sn	3.91	6.5	0.039	1.59
	4	S	4.50	33.1	0.091	-0.41

Forming the EXAFS from the sum of the single scattering paths could check the effects of multiple scattering paths beyond that region. The slightly higher nearest neighbor Cu-S peak is within the noise level. There is also a chance of different order as well, in the region beyond R=6 Å the two experimental spectra exhibit the same features that differ from the calculated spectra, indicating that they originate in actual structural features that may not be the ones in the crystal structure.

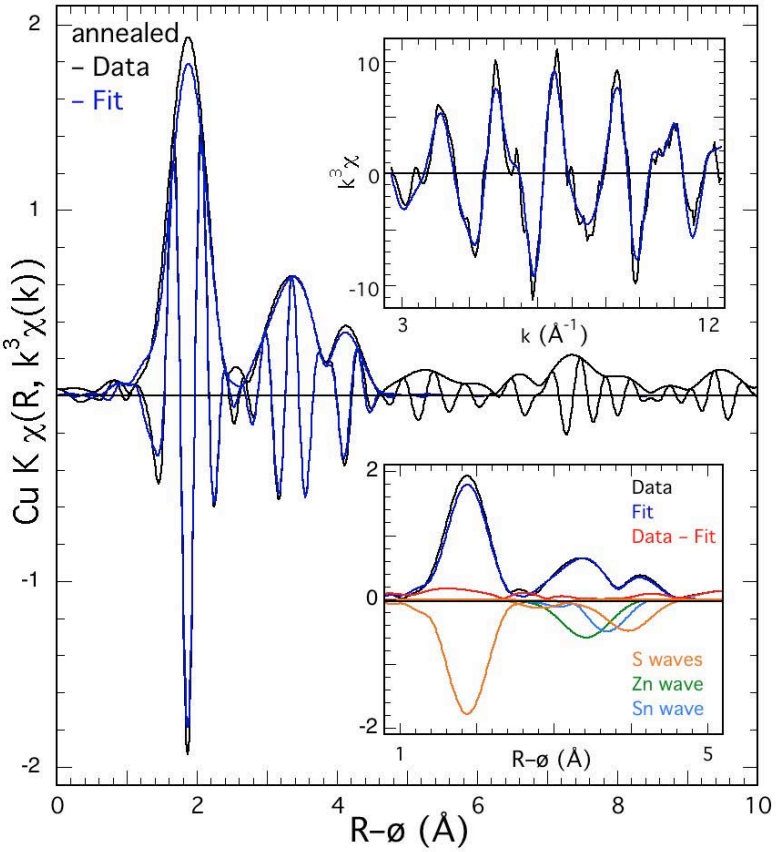

Figure 4.3: Cu XAFS for the annealed CZTS sample. Bottom inset shows the data and fit along with the individual waves.

Good fits are obtained with a relatively simple, four shell model for the structure through 4 Å. Cu and Zn as neighbor atoms are indistinguishable in EXAFS, so that references to Cu or Zn actually mean a possible combination of the two. The similarity in local structure of annealed (Figure 4.3) and unannealed (Figure 4.4) is corroborated by

the curve-fits, the results of which must be compared against the crystal structure, and specifically whether the shells these find are those of the structure and any are missing. These fits show that local minimum in the modulus at R=3.7 Å occurs because the Cu-Sn distance in the unannealed sample is 3.78 Å compared with 3.88 Å on annealing, changing the interference condition with the unchanged Cu-Cu/Zn shell at 3.80(5) Å. It is possible that this change reflects a modification of the ordering within a complicated distribution rather than an actual displacement. There is a slight (0.018 Å) contraction of the nn Cu-S distance from 2.33 to 2.31 Å, and a possible expansion of the long (4.46 Å) Cu-S one. The fits include a possible S shell at 3.23 Å, but its contribution is so small that its presence is uncertain.

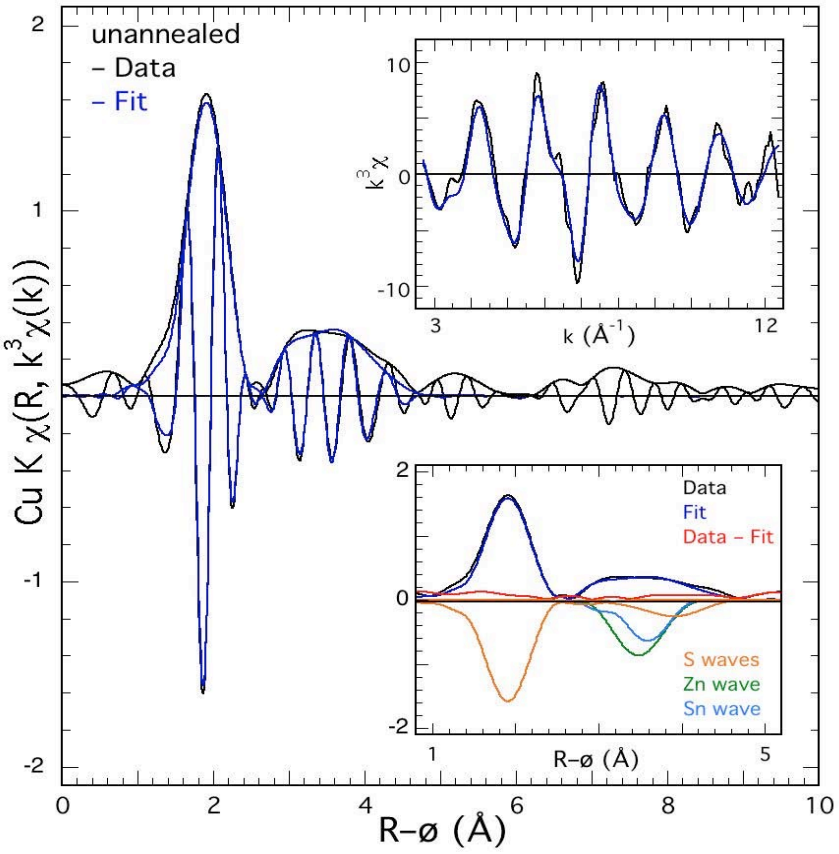

Figure 4.4: Cu XAFS data for the unannealed sample. Bottom inset show the data and fit along with the individual waves.

The contraction of the nearest neighbor (nn) Cu-S bond is validated in the phase difference plot (see Figure 4.5). This, ideally, should be a horizontal line, so the error can be calculated as the deviation from such a line over the fitting range. This is 0.023 ±0.007 Å. This could be sufficiently large to alter the degree of overlap of the copper and sulfur orbitals and affect the degree of covalency and, in turn, the electronic properties and absorbance, depending on the nature of the HOMO and LUMO states across the band gap.

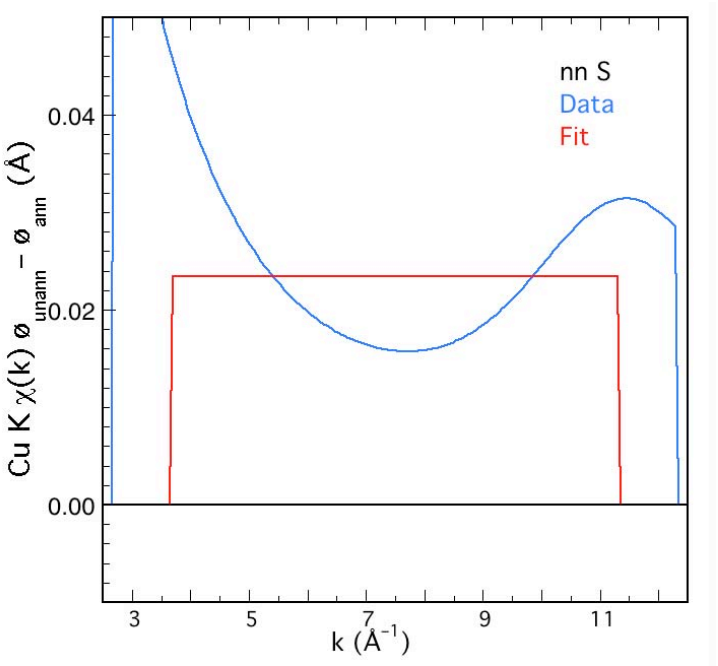

Figure 4.5: Phase difference calculated for Cu-S in the CZTS sample.

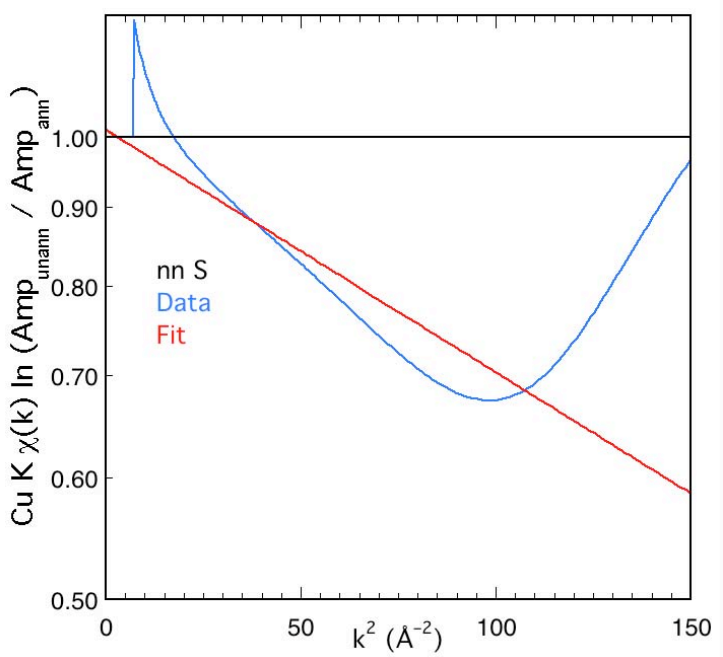

Figure 4.6: Logarithm of the amlitude ratio. Note that the intercept of the linear fit = 1.0, indicating that number of atoms is identical in the two samples. The negative slope indicates a lower Debye-Waller factor in the annealed material.

Similarly, changes in the number of near neighbors that is convoluted with the anharmonic disorder and the Debye-Waller factors are best analyzed as the logarithm of the amplitude ratio that should be a straight line (see Figure 4.6). This shows that the apparent number of atoms is identical in the two samples, indicating negligible changes in the anharmonic disorder, and that the Debye-Waller factor is larger in the unannealed sample by 0.013 Å. This analysis also shows that the cause of the larger FT modulus amplitude in the unannealed spectrum is a change in the shape of the amplitude envelope so that it begins to get larger at k=10 $Å^{-1}$. Because the amplitude is low this is within the noise level. The larger Debye-Waller factor is consistent with less order prior to annealing. Since the amplitude factors – the number of atoms and the Debye-Waller factors – were unconstrained both the conservation of the number and the change in Debye-Waller factor are real differences between the samples.

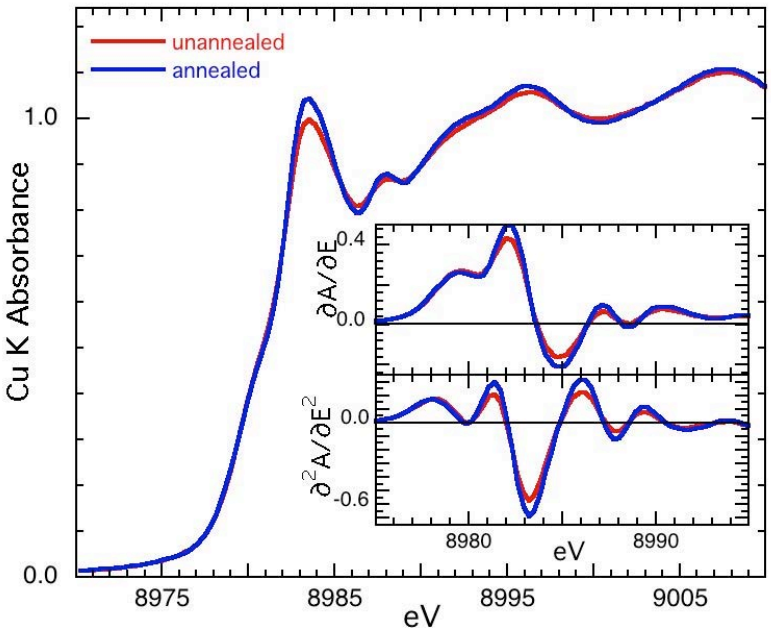

Figure 4.7: Cu XANES for the unannealed and annealed samples. Red line represents the data for the unannealed sample and blue shows the data for the annealed CZTS.

The identity of the numbers and energies of the spectral features in the Cu XANES, seen in Figure 4.7, is consistent with the high degree of similarity in the local structure found by the EXAFS. What is of interest then is the change in the relative intensities of some of the peaks. Since, especially in the pre-edge, these reflect electronic states, it is possible that, as suggested, they are modified by the change in the orbital overlap caused by the contraction of the Cu-S bond on annealing.

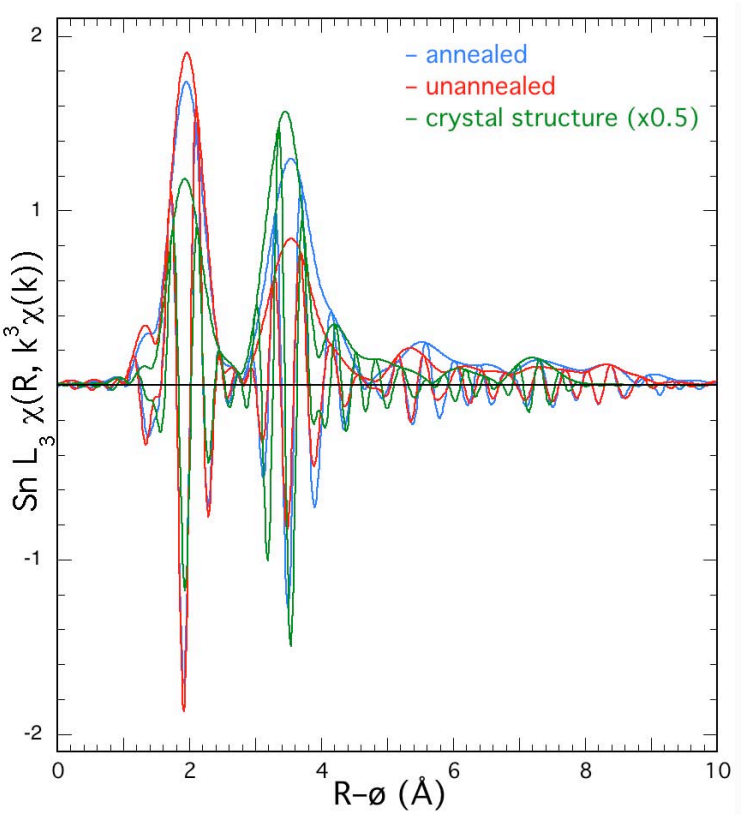

Figure 4.8: Experimental and calculated Sn EXAFS data for Cu_2ZnSnS_4. Blue spectrum shows experimental results for the annealed sample; red depicts experimental data for the as-prepared sample; green shows the data calculated from the crystal structure.

The Sn XAFS differs from that of the copper and the zinc in that the long-range structure has low amplitude indicative of less order. Comparing the experimental and calculated spectra, as presented in Figure 4.8, the relative amplitudes of the peaks representing the contributions of the nearest (S) and next nearest (Zn/Cu) invert relative to the calculated EXAFS, indicating substantially more disorder in the crystal at longer ranges around the tin than the copper and the zinc. The real component nodes of the measured spectra and calculation align well through the nearest neighbor sulfur peak, but, although quite similar for the unannealed and annealed spectra through the entire range with the exceptions of some of the moduli minima, are shifted from the crystal structure in the mid-range even in the second nearest neighbor region before matching again at

R=7–8 Å. The moduli amplitudes are comparable for the sulfur, but the higher amplitude for the second peak implies greater order for the annealed material.

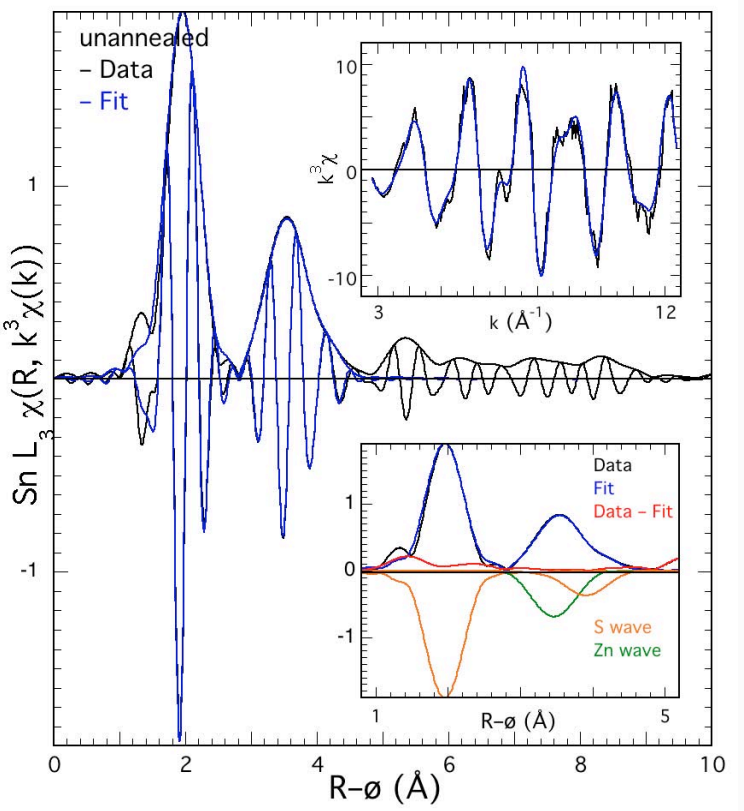

Figure 4.9: Sn XAFS data for the annealed sample showing the data (black) as well as the fit (blue). Bottom inset show the data and fit along with the individual waves.

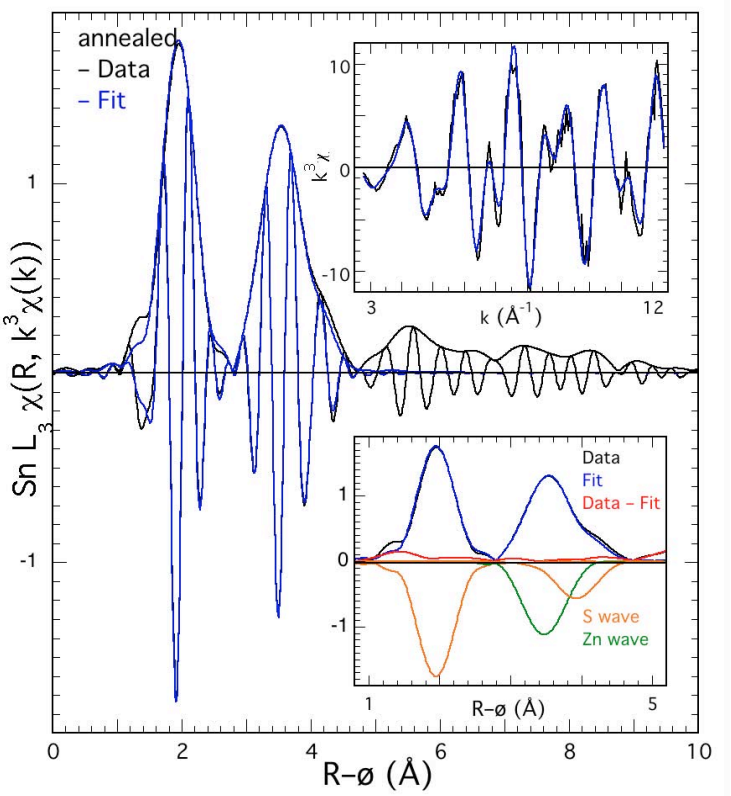

Figure 4.10: Sn XAFS data for the annealed sample showing the data (black) as well as the fit (blue). Bottom inset show the data and fit along with the individual waves.

Table 4.2: Summary of curve fitting results for the Sn XAFS.

Sample	Shell	Neighbor Atom	Distance	Coordination Number	Sigma	ΔE_0
Sn, as-prepared	1	S	2.41	4.9	0.059	5.61
	2	Zn	3.82	7.1	0.085	6.63
	3	S	4.42	15.8	0.103	3.80
Sn, annealed	1	S	2.41	4.3	0.056	5.01
	2	Zn	3.83	10.4	0.080	6.46
	3	S	4.43	20.4	0.095	3.80
Sn, calculated (Feff)	1	S	2.41	4.3	0.025	0.20
	2	Zn	3.83	10.7	0.017	-1.64
	3	S	4.48	22.7	0.074	2.02

Excellent fits for both the unannealed (Figure 4.9) and the annealed (Figure 4.10) samples are obtained with a very simple structure consisting of a nearest neighbor S at the same 2.41 Å distance. The 3.83 Å Sn-Zn/Cu distances (zinc and copper cannot be distinguished by the curve-fits) are within 0.01 Å, as are the long 4.43 Å Sn-S ones that

complete the fit. This is indicative of minimal modification of the tin environment as a result of the annealing process, and appears to affect only the local order. A summary of these curve-fitting results can be found in Table 4.2.

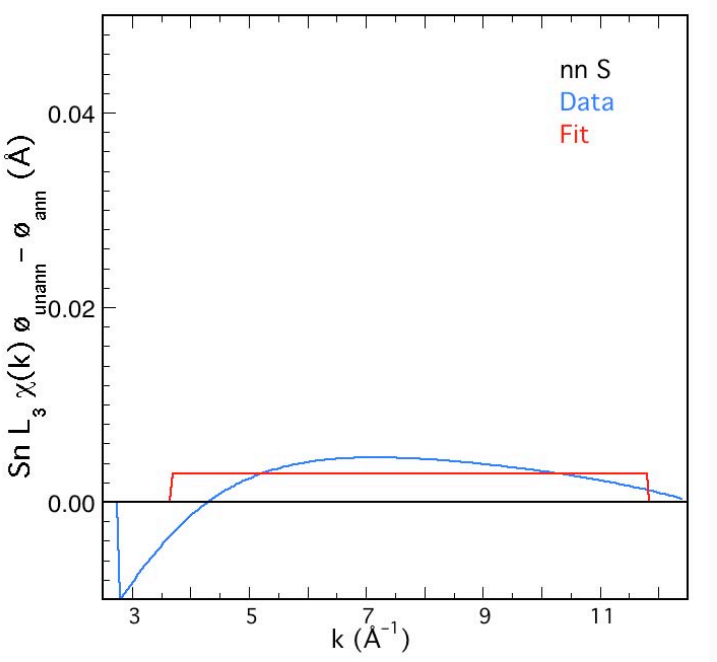

Figure 4.11: Phase difference calculated for Sn-S in the CZTS samples.

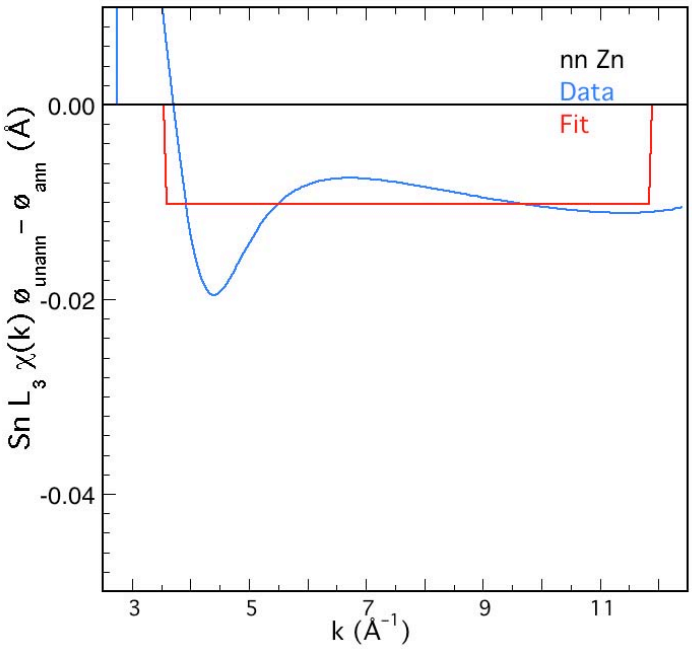

Figure 4.12: Phase difference calculated for Sn-Zn/Cu in the CZTS sample. Blue line shows the data and the red the fit.

Because of the simplicity of the fit with no overlapping shells that could correlate with each other it was possible to perform the phase difference and logarithmic amplitude ratio analysis to both the nn S (Figure 4.11) and the second nn Zn (Figure 4.12). These corroborate the behavior of the $\chi(R)$ spectra and the curve-fits. The difference in Sn-S distance on annealing is only –0.003±0.002 Å, and for the Zn it is a slightly larger 0.010±0.004Å change that, for the second shell, is minimally significant or even negligible.

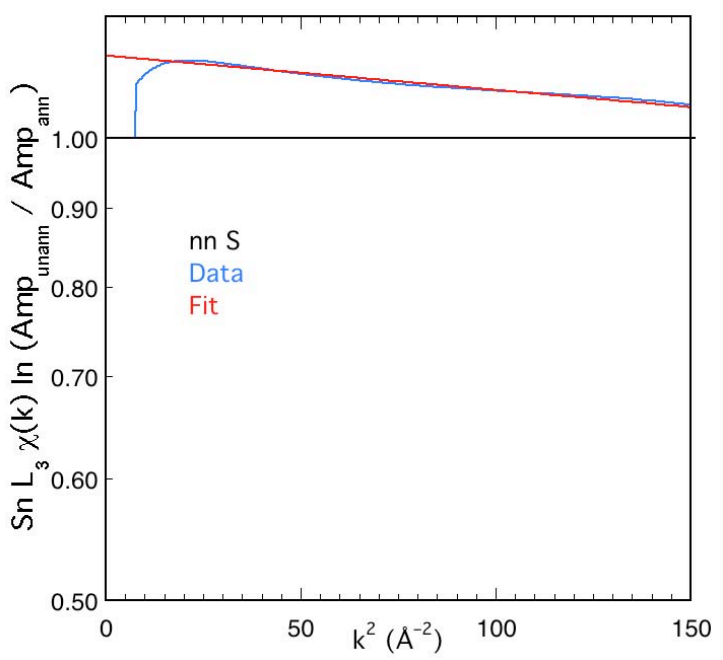

Figure 4.13: Logarithm of the Sn-S amlitude ratio. The intercept of the fit indicates a ~10% decrease in the number of S nearest neighbors or the adoption of an anharmonic distribution on annealing, the slope a very small decrease in the Debye-Waller factor.

The logarithmic amplitude ratios show minimal differences for the Sn-S, as seen in Figure 4.13. The amplitude is less than 10% smaller on annealing without any deviations of the ratio from the expected line, consistent with the change in the numbers of atoms from 4.9 to 4.3 in the fit or in the ratio from 4.0 to 4.5 in the annealed sample, and the Debye-Waller factor is only 0.002 Å smaller, which is negligible.

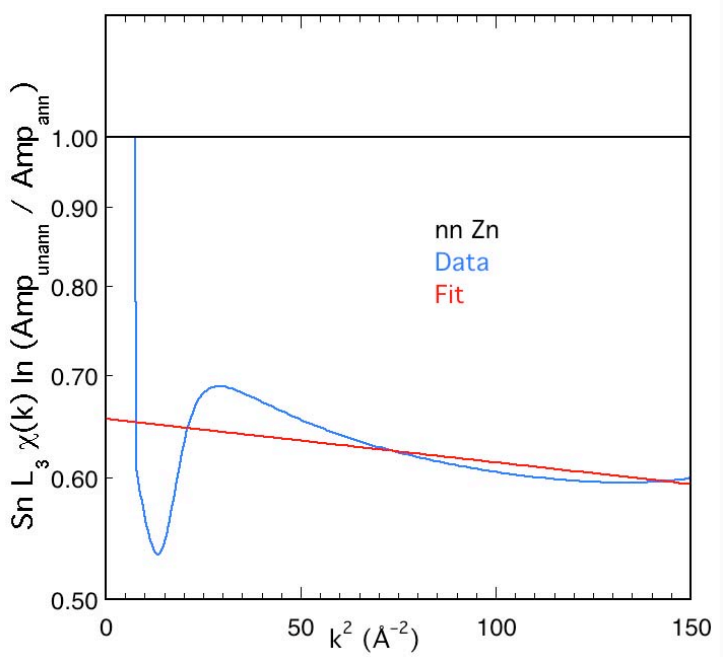

Figure 4.14: Logarithm of the Sn-Zn amlitude ratio.

The Sn-Zn shell, however, exhibits a much larger 25% reduction in the anharmonic disorder that changes the number of atoms from 7.1 to 10.4. This is consistent with the logarithmic-amplitude ratio result, as shown in Figure 4.14. The correspondence between the fit and data from around k=6 Å^{-1} demonstrates that the deviation from linearity at low k does not affect the result. Anharmonic disorder would include the possibility of actual changes in the number of atoms in that shell and/or shifts in the non-Gaussian components of the distribution. In other words, the number of Zn/Cu atoms could increase on annealing, and/or the zinc atoms that compose the shell could rearrange into a more anharmonic distribution. The change in the Debye-Waller factor is a negligible 0.002 decrease on annealing.

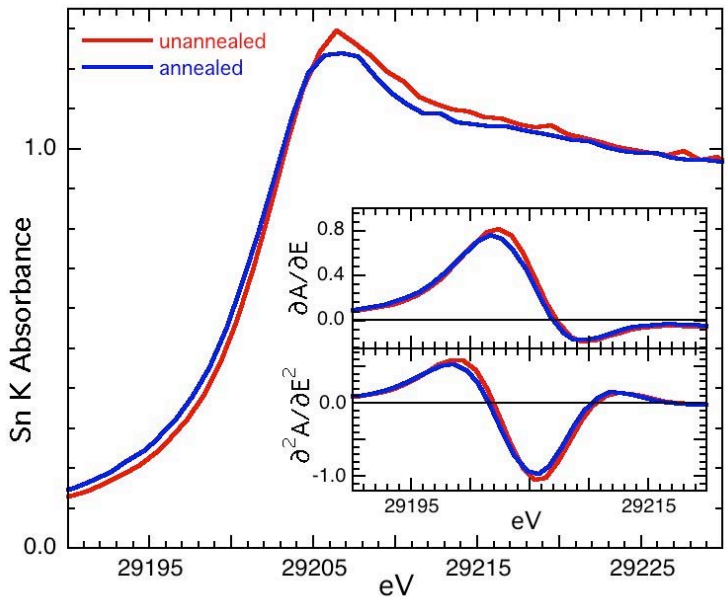

Figure 4.15: Sn XANES for the unannealed and annealed samples. Red line represents the data for the unannealed sample and blue shows the data for the annealed CZTS.

Relative to the Cu, the Sn XANES, presented in Figure 4.15, is broadened by core-hole lifetime effects and therefore exhibits no features except the absorption peak. The small difference in the amplitude and shape affecting the entire peak region evenly is within the noise level and calibration error in this energy region. This is verified by the derivatives that display the same spectral features at almost identical energies. The XANES is therefore consistent with the EXAFS that show only minimal or negligible changes in the Sn local environment and the same for the electronic structure.

The Zn EXAFS, shown in Figure 4.16, differ from the Sn and especially the Cu in that, with the exception of the areas around R=2.5, 3.8, 4.6, and 6 Å, the real component nodes of the experimental and calculated spectra agree fairly well out to R=8 Å, which is an impressivel long distance. The relative amplitudes of the features in the measured spectra at R=5.2 and 6.5 Å are lower than in the calculated one, but the remainder are quite similar so that the overall pattern generally resembles that of the calculated one.

The experimental spectra exhibit a difference from each other at one of these regions, R=2.5 Å. This is a region where, in the calculated spectrum the amplitude of the modulus is close to zero between the first and second neighbor contributions, and in this way differ from the Cu and Sn. An identical pattern occurs at R=3.8 Å. The cause of this difference will be investigated by curve-fits.

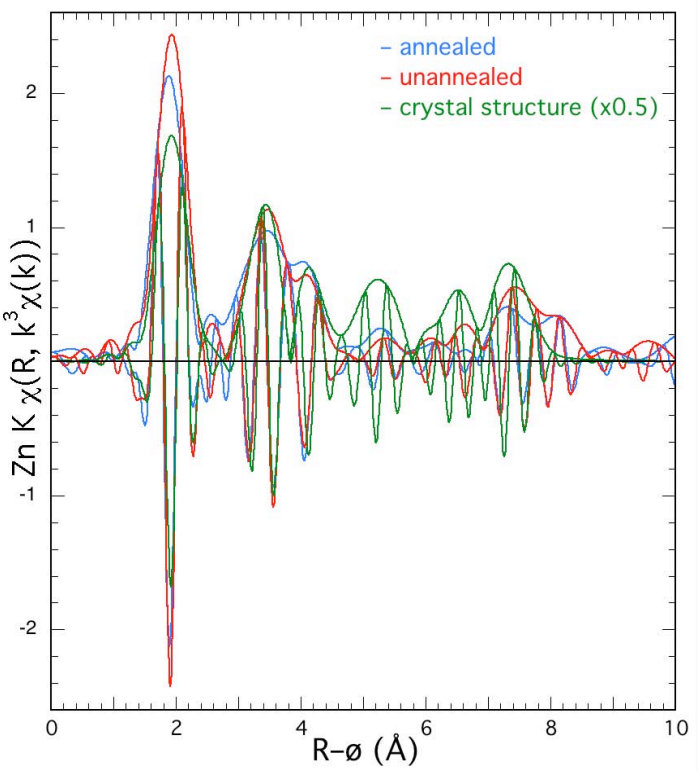

Figure 4.16: Experimental and calculated Zn EXAFS data for Cu_2ZnSnS_4. Blue spectrum shows experimental results for the annealed sample; red depicts experimental data for the as-prepared sample; green shows the data calculated from the crystal structure.

Curve-fits through 4.5 Å in the unannealed sample (Figure 4.17) find a local environment very similar to the Cu, with a nearest neighbor S at 2.32 Å, Zn/Cu at 3.83 Å, Sn at the same distance 3.82 Å (the larger phase shift of the Zn/Cu moves its modulus peak to lower R despite the same distances), and a S at 4.47 Å. Curve fitting results for zinc EXAFS are summarized in Table 4.3. Shifts on annealing (Figure 4.18) are minimal, 0.02 Å expansions of the nn S and Cu/Zn and a 0.04 Å increase in the Zn-Sn

distance. In contrast to the Cu environment where only the Cu-Sn distance increased by 0.1 Å, both of these distances show an increase. Although these expansions in the distances are smaller than the Cu-Sn their population-weighted average is comparable. The Zn-S amplitude from the fit shows lower numbers of atoms and a Debye-Waller factor because of the correlation between these parameters. Good fits for the Zn/Cu and Sn were obtained by constraining the numbers of atoms and lowering the Debye-Waller factor of both shells on annealing, which raises the amplitudes, whereas the distant suffer shell displayed substantial increases in both parameters in the spectrum of the annealed sample. Another finding is that fitting the region at R=2.5 Å requires two additional, non-crystallographic sulfur shells at 2.89 and 3.21 Å in the unannealed sample and one non-crystallographic sulfur shell at 2.89 Å in the annealed sample.

Table 4.3: Summary of curve fitting results for Zn XAFS data.

Sample	Shell	Neighbor Atom	Distance	Coordination Number	Sigma	Delta Eo
Zn, as-prepared	1	S	2.31	4.2	0.067	0.17
	5	S	2.89	1.2	0.062	1.17
	6	S	3.21	1.0	0.062	1.17
	3	Sn	3.8	6.5	0.100	2.17
	2	Zn	3.82	11.0	0.092	2.17
	4	S	4.46	16.7	0.098	2.17
Zn, annealed	1	S	2.33	3.6	0.041	2.08
	5	S	2.89	1.8	0.124	0.08
	6	S	3.41	0.0	0.124	4.08
	2	Zn	3.83	11.0	0.083	2.13
	3	Sn	3.84	6.5	0.083	4.08
	4	S	4.47	25.9	0.120	4.08
Zn, calculated (Feff)	1	S	2.33	4.4	0.028	-1.13
	2	Zn	3.81	8.5	0.061	-3.13
	3	Sn	3.87	5.3	0.081	-2.55
	4	S	4.48	14.5	0.050	-2.59

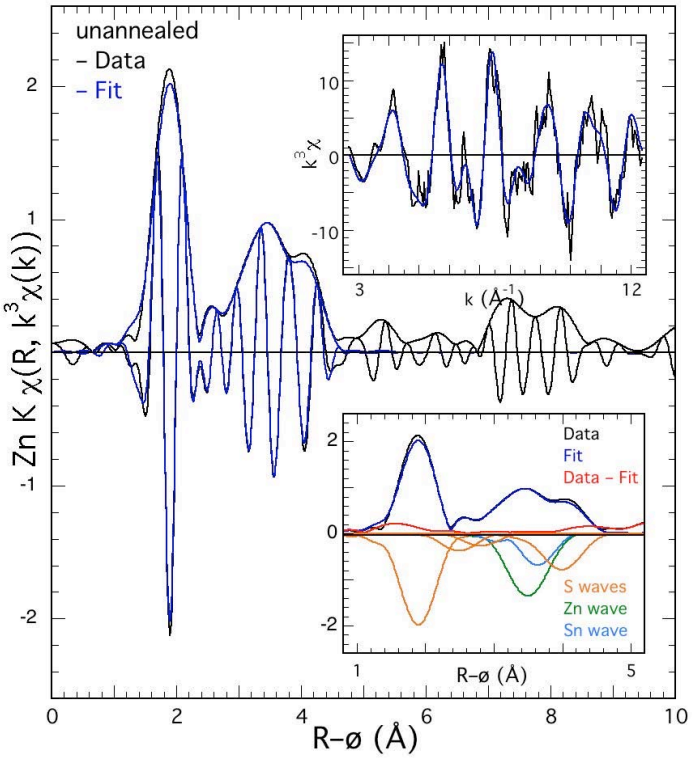

Figure 4.17: Zn EXAFS data for the unannealed sample showing the data (black) as well as the fit (blue). Bottom inset show the data and fit along with the individual waves.

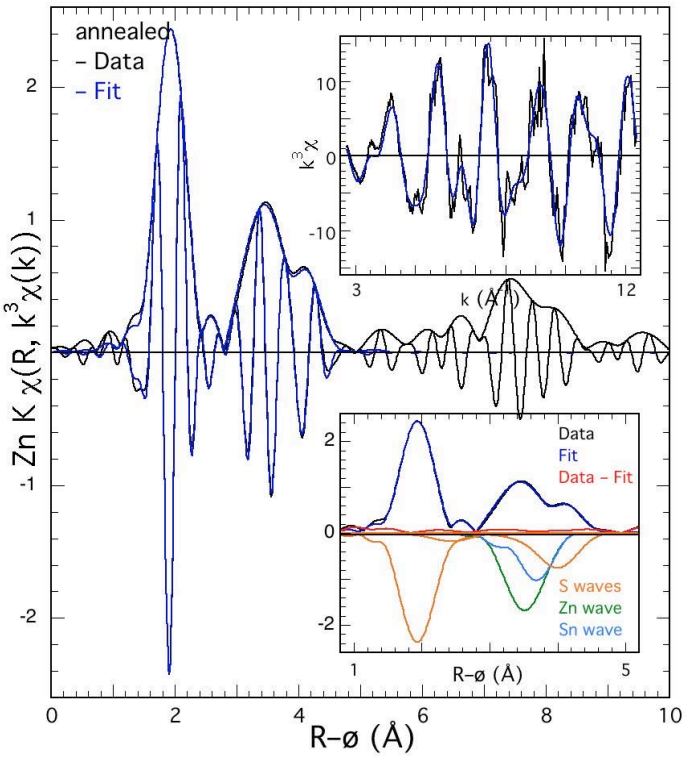

Figure 4.18: Zn EXAFS data for the annealed sample showing the data (black) as well as the fit (blue). Bottom inset show the data and fit along with the individual waves.

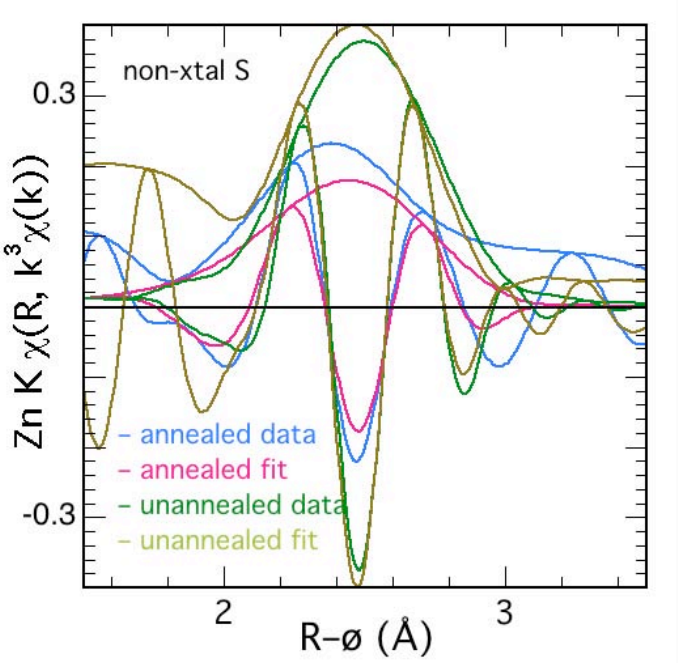

Figure 4.19: The non-crystallographic sulfur shell after separation from the remainder of the structure. Note the decrease in amplitude from the unannealed to the annealed sample.

The presence of the non-crystallographic sulfur shell was tested by separating its contribution in both the data and the fit from the remainder of the spectrum by subtracting out all of the other components (Figure 4.19). This shows that the overall characteristics of the spectral feature being fit including its nodes that are sensitive to its distance are identical in both the unannealed and the annealed data, it is well fit by a Zn-S wave, and that its amplitude is lower in the annealed sample, implying that it is lost in the general increase in ordering resulting from annealing. However, especially in the unannealed sample, this analysis increases the confidence in the presence of this non-crystallographic shell.

Phase-difference analysis of the Zn-S wave, presented in Figure 4.20, corroborates the curve-fit result by finding an expansion of Zn-S bond of 0.029±0.003Å on annealing. It is notable that this is almost exactly the inverse of the Cu-S bond contraction, so that these two effects cancel out in the structure.

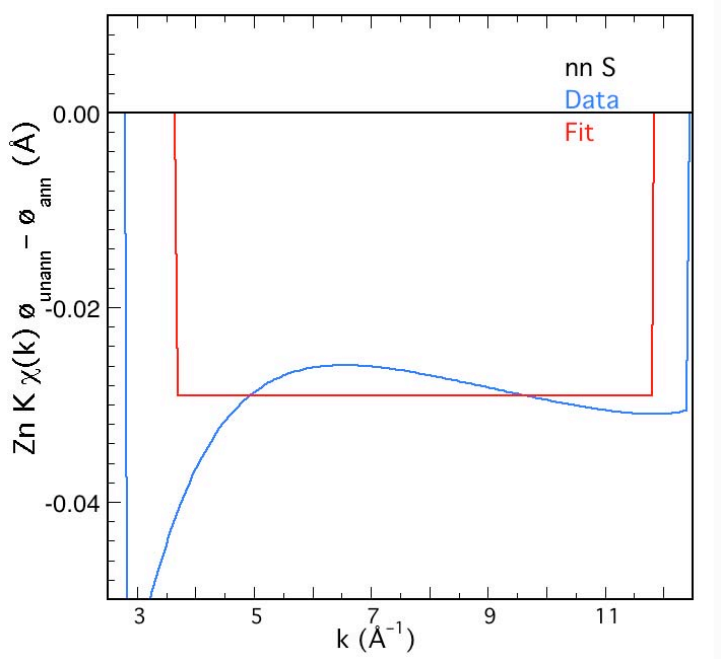

Figure 4.20: Phase difference plot for the Zn-S wave.

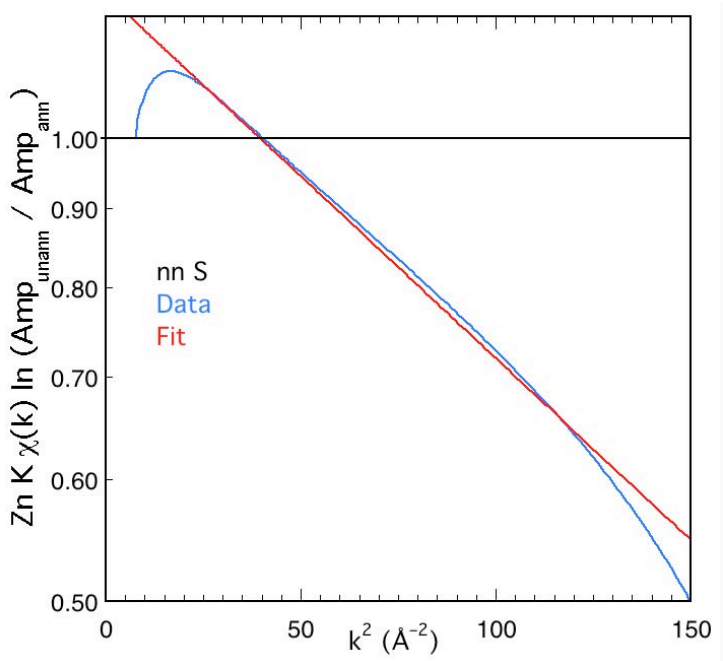

Figure 4.21: Logarithmic amplitude ratio plot for Zn-S.

The ln-amplitude ratio analysis for the near neighbor sulfur shell, shown in Figure 4.21, which separates the number of atoms from the Debye-Waller factor to break their correlation, gives a very good line. It shows a 22% increase in amplitude in the annealed

sample that indicates that the anharmonic disorder that is either a reduction in the average number of near neighbor sulfur atoms around the zinc and/or a change in the Zn-S distribution that makes is less Gaussian is larger on annealing. The harmonic Debye-Waller factor decreases by 0.025 Å upon annealing, which is a relatively large value.

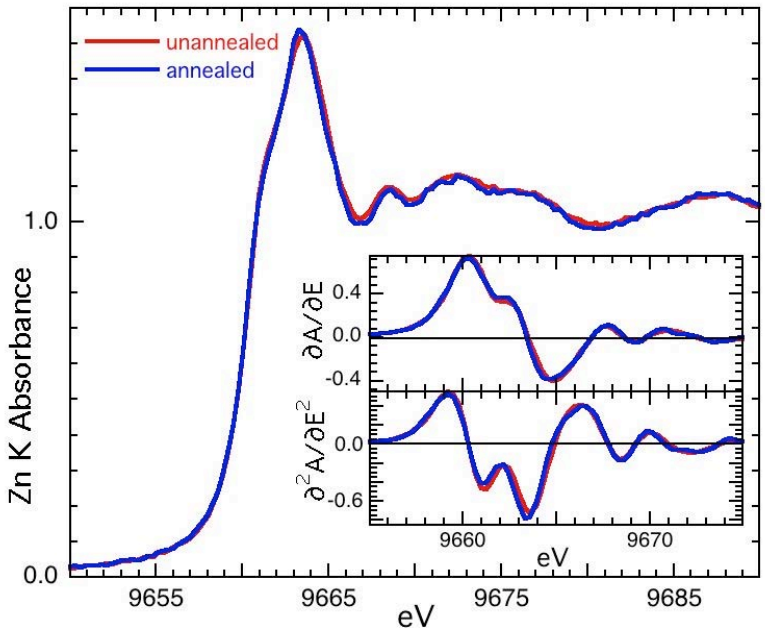

Figure 4.22: Zn XANES for the unannealed and annealed samples. Red line represents the data for the unannealed sample and blue shows the annealed data.

The differences in the Zn XANES (presented in Figure 4.22) between the annealed and unannealed samples are minimal and close to experimental error. Any changes in the local environment or electronic occupancies on the zinc are correspondingly small.

Comparing the separated original, unratioed amplitudes of the Cu-S and Zn-S waves in both samples, as shown in Figure 4.23, it is interesting to note that there is not much difference between the unannealed and annealed samples for the zinc – indicating no change in the number of atoms, but a clear drop in amplitude for the Cu-S from the

unannealed to the annealed. This would suggest that the aforementioned sulfur loss upon annealing is happening preferentially from around the copper sites.

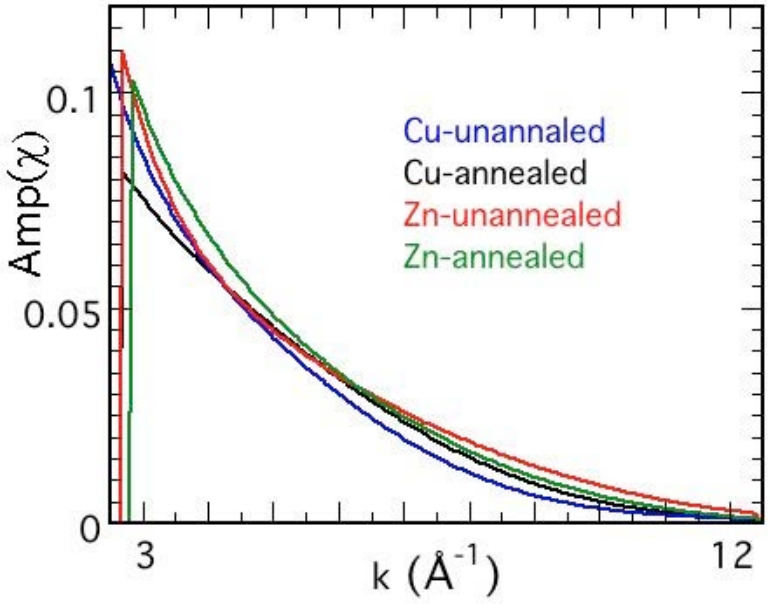

Figure 4.23: Amplitudes with respect to the sulfur. Note that the change in amplitude from the unannealed to the annealed sample happens exclusively for the copper, while the zinc remains fairly constant.

4.4 Conclusions

In summary, the unannealed and annealed samples show significant differences in the crystal structure for this material. These differences include a new sulfur neighbor shell for the zinc that may be present for the copper and that diminishes on annealing. There are, however, additional disordered components. The tin environment is relatively insensitive to annealing. The copper and zinc do exhibit changes that, although modest, are sufficient to change the degree of overlap of the bonds with sulfur. These changes are almost exactly the opposite for the nearest neighbor sulfur shell, but overall similar for the second nearst-neighbor shell except that it involves only the tin shell around the copper but both tin and Cu/Zn shells around the zinc, so overall these displacements are

complicated. There are also changes in the ordering. Oddly, the anharmonic order for the Cu- and Zn-S appears greater for the unannealed samples whereas the harmonic order is less. These data also show an additional sulfur shell that diminishes upon annealing, suggesting there is some sulfur loss occurring during the heat treatment. In addition to this, the sulfur loss appears to be happening preferentially from around the copper sites which could only happen if there was clustering of the copper on the nanometer scale, i.e., domains that are a minimum of several unit cells in size with higher than average amounts of copper. Only in this way could loss of sulfur through volatilization affect only the copper environments and not the zinc. The neutron scattering results show a good fit for the CZTS crystal structure and will aid in the future in understanding any Zn/Cu substitution that may be occurring in the material.

These observed local structural changes aid in the explanation of the observed increase in the optical absorption properties from the unannealed to the annealed sample previously reported. The changes in the bond lengths seen in the XAFS reflect an increase in the orbital overlap, which results in more mixing and thus more separation in the band gap, yielding this increase in the absorption. What is intriguing about these results is that understanding the structural changes accompanying the various synthetic steps will allow for precise control over the composition which will allow tuning of the band gap to optimize the material for device fabrication in the future.

References:

(1) Ginley, D.; Green, M. A.; Collins, R. MRS Bulletin 2008, 33, 355.
(2) Mitzi, D. B.; Gunawan, O.; Todorov, T. K.; Wang, K.; Guha, S. Solar Energy Materials and Solar Cells 2011, 95, 1421.
(3) Repins, I.; Contreras, M. A.; Egaas, B.; DeHart, C.; Scharf, J.; Perkins, C. L.; To, B.; Rommel, N. Progress in Photovoltaics 2008, 16, 235.
(4) Scragg, J. J.; Dale, P. J.; Peter, L. M.; Zoppi, G.; Forbes, I. Physica Status Solidi b 2008, 245, 1772.
(5) Wadia, C.; Alivisatos, A. P.; Kammen, D. M. Environmental Science & Technology 2009, 43, 2072.
(6) Feltrin, A.; Freundlich, A. Renewable Energy 2008, 33, 180.
(7) Jimbo, K.; Kimura, R.; Kamimura, T.; Yamada, S.; Maw, W. S.; Araki, H.; Oishi, K.; Katagiri, H. Thin Solid Films 2007, 515, 5997.
(8) Katagiri, H. Thin Solid Films 2005, 480-481, 426.
(9) Katagiri, H.; Saitoh, K.; Washio, T.; Shinohara, H.; Kurumadani, T.; Miyajima, S. Solar Energy Materials and Solar Cells 2001, 65, 141.
(10) Ito, K.; Nakazawa, T. Japanese Journal of Applied Physics 1988, 27, 2094.
(11) Kobayashi, T.; Jimbo, K.; Tsuchida, K.; Shinoda, S.; Oyanagi, T.; Katagiri, H. Japanese Journal of Applied Physics 2005, 44, 783.
(12) Katagiri, H.; Ishigaki, N.; Ishida, T.; Saito, K. Japanese Journal of Applied Physics 2001, 40, 500.
(13) Seol, J.-S.; Lee, S.-Y.; Lee, J.-C.; Nam, H.-D.; Kim, K.-H. Solar Energy Materials and Solar Cells 2003, 75, 155.
(14) Chan, C. P.; Lam, H.; Surya, C. Solar Energy Materials and Solar Cells 2010, 94, 207.
(15) Ennaoui, A.; Lux-Steiner, M.; Weber, A.; Abou-Ras, D.; Kotschau, I.; Schock, H.-W.; Schurr, R.; Holzing, A.; Hock, R.; Vob, T.; Schulze, J.; Kirbs, A. Thin Solid Films 2009, 517, 2511.
(16) Kamoun, N.; Bouzouita, H.; Rezig, B. Thin Solid Films 2007, 515, 5949.
(17) Katagiri, H.; Sasaguchi, N.; Hando, S.; Hoshino, S.; Ohashi, J.; Yokata, T. Solar Energy Materials and Solar Cells 1997, 49, 407.
(18) Kumar, Y. B. K.; Babu, G. S.; Bhaskar, P. U.; Raja, V. S. Solar Energy Materials and Solar Cells 2009, 93, 1230.
(19) Kurihara, M.; Berg, D.; Fischer, J.; Seibentritt, S.; Dale, P. J. Physica Status Solidi C 2009, 6, 1241.
(20) Nakayama, N.; Kentaro, I. Applied Surface Science 1996, 92, 171.
(21) Pawar, S. M.; Pawar, B. S.; Moholkar, A. V.; Choi, D. S.; Yun, J. H.; Moon, J. H.; Kolekar, S. S.; Kim, J. H. Electrochemica Acta 2010, 55, 4057.
(22) Pawar, B. S.; Pawar, S. M.; Shin, S. W.; Choi, D. S.; Park, C. J.; Kolekar, S. S.; Kim, J. H. Applied Surface Science 2010, 257, 1786.
(23) Schurr, R.; Hölzing, A.; Jost, S.; Hock, R.; Vob, T.; Schulze, J.; Kirbs, A.; Ennaoui, A.; Lux-Steiner, M.; Weber, A.; Kötschau, L.; Schock, H.-W. Thin Solid Films 2009, 517, 2465.

(24) Tanaka, K.; Moritake, N.; Uchiki, H. Solar Energy Materials and Solar Cells 2007, 91, 1199.
(25) Moriya, K.; Tanaka, K.; Uchiki, H. Japanese Journal of Applied Physics 2007, 46, 5780.
(26) Moriya, K.; Tanaka, K.; Uchiki, H. Japanese Journal of Applied Physics 2008, 47, 602.
(27) Miyamoto, Y.; Tanaka, K.; Oonuki, M.; Moritake, N.; Uchiki, H. Japanese Journal of Applied Physics 2008, 47, 596.
(28) Oishi, K.; Saito, G.; Ebina, K.; Nagahashi, M.; Jimbo, K.; Maw, W. S.; Katagiri, H.; Yamazaki, M.; Araki, H.; Takeuchi, A. Thin Solid Films 2008, 517, 1449.
(29) Rajeshmon, V. G.; Kartha, C. S.; Vijayakumar, K. P.; Sanjeeviraja, C.; Abe, T.; Kashiwaba, Y. Solar Energy 2011, 85, 249.
(30) Jeon, M.; Shimizu, T.; Shingubara, S. Materials Letters 2011, 65, 2364.
(31) Tanaka, K.; Moritake, N.; Oonuki, M.; Uchiki, H. Japanese Journal of Applied Physics 2008, 47, 598.
(32) Zhang, X.; Shi, X.; Ye, W.; Ma, C.; Wang, C. Applied Physics A 2009,94, 381.
(33) Tanaka, K.; Oonuki, M.; Moritake, N.; Uchiki, H. Solar Energy Materials and Solar Cells 2009, 93, 583.
(34) Scragg, J. J.; Dale, P. J.; Peter, L. M. Electrochemistry Communications 2008, 10, 639.
(35) Katagiri, H.; Jimbo, K.; Maw, W. S.; Oishi, K.; Yamazaki, M.; Araki, H.; Takeuchi, A. Thin Solid Films 2009, 517, 2455.
(36) Katagiri, H.; Jimbo, K.; Yamada, S.; Kamimura, T.; Maw, W. S.; Fukano, T.; Ito, T.; Motohiro, T. Applied Physics Express 2008, 1, 041201.
(37) Tanaka, T.; Yoshida, A.; Saiki, D.; Saito, K.; Guo, Q.; Mitsuhiro, N.; Yamaguchi, T. Thin Solid Films 2010, 518, S29.
(38) Tanaka, K.; Fukui, Y.; Moritake, N.; Uchiki, H. Solar Energy Materials and Solar Cells 2011, 95, 838.
(39) Weber, A.; Krauth, H.; Perlt, S.; Schubert, B.; Kotschau, I.; Schorr, S.; Schock, H. W. Thin Solid Films 2009, 517, 2524.
(40) Weber, A.; Mainz, R.; Schock, H.-W. Journal of Applied Physics 2010, 107, 013516 (6 pages).
(41) Scragg, J. J.; Ericson, T.; Kubart, T.; Edoff, M.; Platzer-Bjorkman, C. Chemistry of Materials 2011, 23, 4625.
(42) Redinger, A.; Berg, D. M.; Dale, P. J.; Siebentritt, S. Journal of the American Chemical Society 2011, 133, 3320.
(43) Wang, Y.; Gong, H. Journal of the Electrochemical Society 2011, 158, H800.
(44) Riha, S. C.; Parkinson, B. A.; Prieto, A. L. Journal of the American Chemical Society 2009, 131, 12054.
(45) Basol, B. M.; Kapur, V. K.; Norsworthy, G.; Halani, A.; Leidholm, C. R.; Roe, R. Electrochemical and Solid-State Letters 1998, 1, 252.
(46) Panthani, M. G.; Akhavan, V.; Goodfellow, B.; Schmidtke, J. P.; Dunn, L.; Dodabalapur, A.; Barbara, P. F.; Korgel, B. A. Journal of the American

Chemical Society 2008, 130, 16770.
(47) Steinhagen; Panthani, M. G.; Akhavan, V.; Goodfellow, B.; Koo, B.; Korgel, B. A. Journal of the American Chemical Society 2009, 131, 12554.
(48) Riha, S. C.; Fredrick, S. J.; Sambur, J. B.; Liu, Y.; Prieto, A. L.; Parkinson,
B. A. ACS Applied Materials & Interfaces 2011, 3, 58.
(49) Schorr, S. Solar Energy Materials and Solar Cells 2011, 95, 1482.
(50) Conradson, S. D.; Begg, B. D.; Clark, D. L.; den Auwer, C.; Ding, M.; Dorhout, P. K.; Espinosa-Faller, F. J.; Gordon, P. L.; Haire, R. G.; Hess, N. J.; Hess, R. F.; Keogh, D. W.; Morales, L. A.; Neu, M. P.; Paviet Hartmann, P.; Runde, W.; Tait, C. D.; Veirs, D. K.; Villella, P. M. Journal of the American Chemical Society 2004, 126, 13443.